TUFTS UNIVERSITY

Investigating the Effect of Deformation and Stirring on Pure Gold Surface Tension Measurements Using a Faraday Forcing Technique

by

William Cusato

A Thesis Submitted
in Partial Fulfillment of the
Requirements for the Degree

Bachelor of Science in Mechanical Engineering

Approved, Thesis Committee:

Douglas Matson, Chair
Professor of Mechanical Engineering

Erica Kemmerling
Assistant Teaching Professor of
Mechanical Engineering

Medford, Massachusetts

May, 2026

ABSTRACT

Investigating the Effect of Deformation and Stirring on Pure Gold Surface Tension Measurements Using a Faraday Forcing Technique

by

William Cusato

Surface tension is a critical thermophysical property that is vital to the modeling of manufacturing processes. Gold was studied due to its inert nature and simple composition, which eases the study of novel experimental techniques. This provides a foundation on which more complex, industrially relevant materials can be investigated. Surface tension was studied in an electromagnetic levitator (EML) in microgravity and excited with Faraday forcing to induce oscillations, a method typically reserved for electrostatic levitators (ESL). The frequency of oscillations is related to surface tension by the Rayleigh equation. These results are corrected for frequency shifts resulting from sample deformation. To investigate the effect of stirring, caused by the EML heater, a range of heater control voltages were tested. It was found that increasing heater control voltage both increases surface tension's temperature dependence and increases

the value of surface tension at the melting temperature of gold. By extrapolating the results of the heater control runs to zero voltage, an additive correction can be created for both gold's surface tension at the melting temperature and temperature dependence. These results, when compared to pulse excitation, a standard EML experimental method, show that Faraday forcing is a viable method of determining surface tension and yields more precise measurements, supporting its use in future investigations.

Acknowledgments

I would first like to thank my research advisor, Professor Doug Matson, for giving me such a unique and strong academic opportunity. What started as a simple request for a letter of recommendation turned into the most formative academic experience of my life up to this point. His unwavering commitment to the development of his students is something that I am indebted to, and his research mindset has aided me leaps and bounds, particularly in the development of a mindset that keeps asking questions. I'm seemingly being seduced by 'the dark side,' which I don't view as a bad thing.

In addition to Professor Matson, I would like to thank everybody in his research group for their support in integrating me as a member of their team and providing guidance when I needed it. This in particular extends to Dr. Jannatun Nawer, who taught me many analysis techniques while in the midst of an intense job search; Dr. Peace Muusha, who offered guidance during the writing of this work; and Ben Ledru, whose work runs concurrent to mine and was my main source of peer support during this process.

In a similar manner, I would like to thank the second reader of this thesis, Assistant Professor Erica Kemmerling. In the coursework taught by her, I

learned the basics of technical writing, experimental methods, and technical skills like MATLAB that were instrumental in the writing and completion of this work. The development of these skills undoubtedly influenced my decision to pursue research.

Finally, I would like to thank my parents, who have done everything in their power to set me and my siblings on an academic path. Without their support and guidance, I would not find myself able to conduct research, especially at an institution like Tufts University. Despite what I said at the time, my mom's summer 'math workshops' created an appreciation for school, and I see this work as the culmination of that appreciation.

Contents

Abstract ii

Acknowledgments iv

List of Tables x

List of Illustrations xiii

1 Introduction 1

1.1 Overview 1

1.2 Motivation 1

2 Background 3

2.1 Containerless Processing 3

2.1.1 Alloy Selection 3

2.1.2 Methods 4

2.2 Surface Tension 8

2.2.1 Theory 8

2.2.2 Rayleigh Equation 10

2.2.3 Experimental Measurement 12

2.3 ISS-EML Heater 14

2.3.1 Capabilities and Purpose 15

2.3.2 Effect on Deformation 15

2.3.3 Deformation Induced Frequency Shift 17

2.4 Temperature Measurement 18

2.5 Fluid Velocity in EML Testing 21

3 Methods 26

3.1 Sample Preparation 26

3.2 Faraday Forcing 28

3.3 Data Segmentation 31

3.4 Deformation Definition 34

3.4.1 Definition of Top View Deformation 34

3.4.2 Definition of Side View Deformation 35

3.5 Surface Tension Derivation and Deformation Correction 37

3.5.1 Rayleigh Method 37

3.5.2 Deformation Corrected Analysis 38

3.6 Quantifying Fluid Velocity 39

4 Results 41

4.1 Pyrometry 41

4.2 Frequency Analysis 42

5 Discussion 54

5.1 Validation of Excitation Parameters 54

5.1.1 Validation of Faraday Amplitude 54

5.1.2 Validation of Stimulation Time 55

5.1.3 Validation of Faraday Frequency 57

5.2 Effect of Deformation on Surface Tension 58

5.2.1 Correction Factors 59

5.2.2 Corrected Surface Tension 62

5.3 Effect of Stirring on Surface Tension 64

5.3.1 Quantification of Stirring 64

5.3.2 Statistical Analysis of Results 66

5.3.3 Extrapolation to Zero Stirring 67

5.4 Comparison to Pulse Excitation 71

6 Uncertainty Analysis 72

6.1 Uncertainty in Experimental Methods 72

6.2 Uncertainty in Temperature 73

6.3 Uncertainty in Mass 75

6.4 Uncertainty of Fitted Parameters 76

6.5 Uncertainty in Frequency 77

6.6 Uncertainty in Linear Regression 79

6.7 Uncertainty in Surface Tension 80

6.8 Uncertainty in Deformation 81

6.8.1 Top View 81

6.8.2 Side View 82

6.9 Uncertainty in Corrected Surface Tension 83

6.10 Tabular Summary of Results 85

7 Conclusion **86**

8 Future Work **89**

Bibliography **91**

Appendices **97**

A Sample Historical Data Sheet 97

B Sample Calculation 98

B.1 Surface Tension Calculation 98

B.2 Pyrometry Correction 99

B.3 Velocity Calculation 101

C Pyrometer Corrected Time-Temperature Profiles 103

D Uncorrected Surface Tension Profiles 106

E Corrected Rayleigh Equation Curve Fits 108

F Corrected Surface Tension Profiles 111

G Derivation of Gold and Electrical Conductivity 113

H Deposition Coil Mass Loss Table 115

I Code 119

I.1 Sectioned Analysis 119

I.2 Surface Tension Correction 120

I.3 Velocity and Reynolds Number 121

Tables

2.1 EML Modules and their purpose [1]. 7

2.2 Low-order oscillation modes of a liquid droplet characterized by the spherical harmonic index ℓ [2]. 10

2.3 Comparison of positioning and heating electromagnetic fields on the ISS-EML [1]. 16

2.4 Material Properties Used in the Velocity Surrogate Model . . . 25

3.1 Experimental Test Matrix 31

3.2 Initial Guesses and Lower and Upper Bounds for Iterative Levenberg-Marquardt Algorithm 34

3.3 Initial Guesses and Lower and Upper Bounds for Frequency Shift Curve Fit 38

3.4 Flow Regimes Within a Metallic Droplet Defined by Reynolds Number 40

4.1 Cycle number, associated HCV value, and observed liquidus temperature. 42

4.2 Results of Linear Fit of Uncorrected Surface Tension Data $y = m(T - T_m) + b$ 43

4.3 Frequency and Deformation Data — 0.3 V 44

4.4 Frequency and Deformation Data — 0.5 V 48

4.5 Frequency and Deformation Data — 0.6 V 48

4.6 Frequency and Deformation Data — 0.8 V 50

4.7 Frequency and Deformation Data — 1.0 V 51

5.1 Experimental Test Matrix 54

5.2 Experimental input parameters for the four f-sweep runs. . . . 57

5.3 Rayleigh equation correction factors for all heater control voltage runs. 60

5.4 Average of First Three Frequencies After Excitation for Each Heater Control Voltage 61

5.5 Results of linear fits to corrected surface tension data, $\sigma = m(T - T_m) + b$. 63

5.6 Results of chi-squared test for the effect of stirring on surface tension fit parameters. 67

5.7 Extrapolated surface tension parameters at zero stirring. . . . 68

5.8 Comparison of Surface Tension Line of Best Fits with Respect to Temperature [3, 4] 68

5.9 Heater and Frequency Corrected Linear Regression Results . . 70

5.10 Comparison of Zero Stirring Lines of Best Fit Between Pulse Excitation and Faraday Forcing [3, 4] 71

6.1 Summary of Relative Uncertainty Results 85

Illustrations

2.1 Dramatic Sample Deformation Observed in Land-Based Electromagnetic Levitators 5

2.2 Photo of the Physical ISS-EML Arrangement with Labeled CAD Diagram of the ISS-EML Modules [1] 6

2.3 Photo of MSFC ESL as of January, 2026 9

2.4 Representation of Spherical Harmonics Ranging from $\ell = 2$ to $\ell = 4$ [5] 11

2.5 Plot of Egry's surface tension results for gold in microgravity and ground-based experiments [3, 6] 12

2.6 Dipole EML Heating Field (Red) and Quadruple Positioning Field (Blue) and Associated Forces on the Sample [1] 16

2.7 Velocity Fields of $Fe_{50}Co_{50}$ for different heater control currents 23

3.1 Preparation of the Ingot Blank Showing Induction Melting, Ingot Rolling, Ingot Trimming and the Creation of the Press Fit Blank 27

3.2 Machining of Sphere Showing the Press Fit Blank, Blank Adhesion Tool, Lathe Machining and the Final Sample 27

3.3 Unthresholded Top View Frame Without (Left) and With (Right) Ellipsoidal Curve Fit 29

3.4 Unthresholded Side View Frame Without (Left) and With (Right) Ellipsoidal Curve Fit 30

3.5 Plot of Forced (Dark Blue) and Free Oscillations (Light Blue) within Sample and Heater Control Value (Black) vs. Time (s) for Cycle 32 Top View 32

3.6 $y = Ae^{-t/\tau}\sin(2\pi\nu + \phi) + D$ Applied to Sample Dataset with A, ν and ϕ Labeled For a Side View Signal 33

3.7 Sample with Oxide Present on Surface (Left) and Associated Oxide Spike (Right) 38

4.1 Corrected Time-Temperature Profile of Cycle 31 (Left), with Melt Plateau (Right). Filtered Signal Given by Dashed Black Line (Right) 41

4.2 Surface Tension (N/m, Left Axis) and Frequency (Hz, Right Axis) vs. Temperature Profile for all $U^H_{\text{ctr}} = 0.3$ Runs 43

5.1 Droplet oscillation amplitude (pixels^2) vs. Faraday forcing amplitude (V). 55

5.2 Oscillation profile (pixels^2) vs. time (s), with active Faraday forcing shown in black and free damping in blue. 56

5.3 Oblate Eccentricity at the End of Excitation amplitude vs. Faraday Excitation Duration (s). 56

5.4 Amplitude (pixels^2) vs. forced frequency (Hz) for Cycles 56, 57, 60, and 61, respectively. 58

5.5 Max Eccentricity vs. Heater Control Voltage 59

5.6 Steady State Deformation (%) vs. Heater Control Voltage for Both Top View (Blue) and Side View (Orange) Runs 60

5.7 Nonlinear regression of the frequency correction formula $\nu_c = \nu_{\theta=0}(1 + p_\theta\theta)(1 + p_1\delta + p_2\delta^2)$ for $U^H_{\text{ctr}} = 0.8$ V. 61

5.8 Frequency (Hz) vs. deformation for heater control voltages of 0.3, 0.6, 0.8, and 1.0 V, respectively. 63

5.9 Comparison of corrected surface tension curve fits across all heater control voltage runs. 64

5.10 Maximum convective velocity (left) and Reynolds number (right) vs. temperature (K). 65

5.11 Cumulative convective velocity (left) and Reynolds number (right) vs. time during sinusoidal heater excitation. 66

5.12 Slope (left) and intercept (right) of the corrected surface tension fit vs. heater control voltage, with linear extrapolation to zero stirring. 68

5.13 Plot of Previous Surface Tension Results with Extrapolated Zero-Stirring Condition (This Study) Overlaid 69

5.14 Plot of Surface Tension vs. Temperature with Frequency and Heater Corrections Applied 70

6.1 Time-Temperature Profile of Cycle 31 with Boxes Representing Apparent (Green) and Apparent Liquidus (Red) Indices Used for Uncertainty Calculation 74

B.1 Observed Frequency (Hz) vs. Temperature (K) for Cycle 31 Top View 98

B.2 Corrected Frequency Formula Applied to 0.3 HCV Dataset with $\nu_{\theta=0} = 18.91$, $p_1 = -0$, $p_2 = -2.713$, $p_\theta = -0.139$, and $R^2 = 0.695$ 99

B.3 Full Temperature Profile (Left) and Subsection of Melt Plateau (Right) for Cycle 31 100

C.1 Corrected Pyrometry Time (s) Temperature (K) Profiles for All Cycles 105

D.1 Individual Uncorrected Surface Tension vs. Temperature Profiles for HCV Values of 0.3, 0.5, 0.6, 0.8 and 1.0 V Respectively 107

E.1 Plots of Corrected Frequency Formula ($\nu_c = \nu_{\theta=0}(1 + p_\theta\theta)(1 + p_1\delta + p_2\delta^2)$) for HCV Values of 0.3, 0.5, 0.6, 0.8 and 1.0 V Respectively 110

F.1 Individual Corrected Surface Tension vs. Temperature Profiles for HCV Values of 0.3, 0.5, 0.6, 0.8 and 1.0 V Respectively . . 112

G.1 Raw Results of SCE Resistivity and Density 114

G.2 Raw Results of SCE Resistivity and Density with Linear Fit . 114

Nomenclature

δ	Deformation
ℓ	Mode of Oscillation
γ	Surface Tension
ν	Frequency (Hz)
$\nu_{\theta=0}$	Frequency at Liquidus Temperature
θ	Dimensionless Temperature $\left(\frac{T}{T_{\text{liq}}}\right)$
A	Amplitude of Signal
D	X-axis Offset of Signal
e	Eccentricity
m	Mass (g)
p_1	Linear Deformation Correction Factor
p_2	Quadratic Deformation Correction Factor
R_0	Radius of Spherical Droplet
R_L	Polar Radius
R_w	Equitorial Radius
T	Absolute Temperature
T_L	Liquidus Temperature
T_{PL}	Pyrometry Reading of Liquidus Temperature
T_P	Pyrometry Reading of Temperature
U^H_{ctr}	Heater Control Voltage
U^P_{ctr}	Positioner Voltage

Chapter 1

Introduction

1.1 Overview

Manufacturing techniques for metals often involve melting the material to achieve desired geometries. Two of the most important governing properties for how a molten metal behaves are its surface tension and viscosity. This study utilizes the electromagnetic levitator (EML) aboard the International Space Station (ISS) to characterize gold's surface tension. EML samples, or droplets, are levitated and excited to incite oscillations within the droplet. The frequency of these oscillations can be used to find the material's surface tension. However, the frequency is also affected by the deformation of the droplet by the EML heater. By changing the output of the EML heater, the relationship between derived surface tension properties and deformation can be determined. Stimulating samples using the EML also incites fluid flow within the droplet. By using a surrogate model to quantify the Reynolds number within the droplet under certain testing conditions, the effect of stirring can be determined.

1.2 Motivation

Advanced manufacturing techniques, namely additive manufacturing, are developing to industrial relevance. The desire for additive manufacturing is twofold, as it saves material compared to traditional manufacturing processes

that remove material and can be leveraged to create complex geometry with more ease than traditional methods [7]. Particular interest in metal additive manufacturing has been placed in the aerospace industry, where agencies like NASA have devoted resources to developing rocket nozzles from additive manufacturing techniques [7]. Due to the complexity of such operations, predictive modeling of additive manufacturing techniques is paramount to optimize processes and understand multiphysics effects unique to additive manufacturing, such as melt-pool dynamics and Marangoni effects [8]. These predictive models are particularly reliant on the thermophysical properties of melted metals, such as surface tension and viscosity [8]. As a result, increased fidelity in the measurement of these properties increases fidelity in the predictive models.

Gold, while not an additive manufacturing material, can be used to understand trends in experimental testing, consequently aiding in the testing of more complex materials and alloys. Because gold is an inert pure element, it is free of the complex interactions found in multi-component alloys. Therefore, by studying a pure element's thermophysical properties and reaction to processing techniques, a benchmark that can be used for validation of other, more complex, results is formed [9]. In ground-based experiments, gold is difficult to levitate and is influenced heavily by the gravitational force, which induces asymmetry in the droplet [9]. This proves problematic as most analyses of containerless solidification assume spherical droplet geometry. These problems are effectively reduced in the microgravity environment of the ISS-EML.

Chapter 2

Background

2.1 Containerless Processing

Containerless processing is an umbrella term used to group methods and equipment that allow materials to be studied without contact with container walls and other boundaries. Material selection and knowledge of containerless equipment are vital to understanding the experimental procedures and analysis used in this study.

2.1.1 Alloy Selection

Gold was chosen as the material to study the effects of stirring and deformation on surface tension derivation. One primary reason for this is gold's simple composition. When studying multiphase alloys, interactions between the respective phases can complicate analysis through changes in composition in the metallic droplet. Because gold is a pure element, it does not share this pitfall. This allows gold to be used as a baseline test for determining the relationship between testing conditions and thermophysical property derivation, easing subsequent analysis on more complex alloys [10]. Additionally, gold is a material that has been studied for years due to its prevalence in jewelry, electronics, and other sectors. Because of this, there exists a multitude of pre-existing data to 'ground' analysis [6, 11, 4, 9].

Surface tension measurement can be dramatically skewed by surface contami-

nation. Selecting gold as the studied material acts as a strategic choice against contamination, particularly oxide contamination. Metals like gold and platinum are inert and immune to oxide contamination during terrestrial sample preparation [3, 9]. Because of this, inert metals like gold can be used to calibrate levitators, as their measurements are stable across different experimental set-ups [3].

Gold's high electrical conductivity can also be leveraged to study the velocity and stirring within the droplet. The amount of stirring present within a sample is dependent on the density, viscosity, and electrical conductivity of the sample material. Leveraging gold's properties allows for a wide range of flow regimes to be studied [9, 12, 13].

2.1.2 Methods

EML and ISS-EML

Installed in 2014, the ISS-EML is a containerless material testing facility located in the Columbus Module of the International Space Station [14]. Samples are loaded into the EML within a wound coil that provides separate electromagnetic fields to both position and heat the sample [14]. With the capability to melt samples up to 2200°C, the ISS-EML enables testing of a wide range of metallic elements and alloys. Through different experimental configurations, it can measure surface tension, viscosity, density, and electrical conductivity of materials [14, 15]. These measurements are significantly enhanced by the equipment's microgravity environment. Land-based EMLs must compensate for the 1-g gravitational force exerted on samples with stronger electromagnetic fields. This requirement can lead to droplet asymmetries that complicate

sample analysis, as spherical sample geometry is often assumed [9]. Droplet asymmetry is seen in Figure 2.1. Droplet asymmetry is particularly an issue when conducting EML testing, as opposed to other containerless solidification methods, due to its larger sample size, which ranges 6–10 mm and 2–4 g [1]. This risk is effectively eliminated in microgravity, where the sample levitates without requiring strong electromagnetic fields. Instead, a small positioning field is utilized to prevent samples from drifting within the chamber [1].

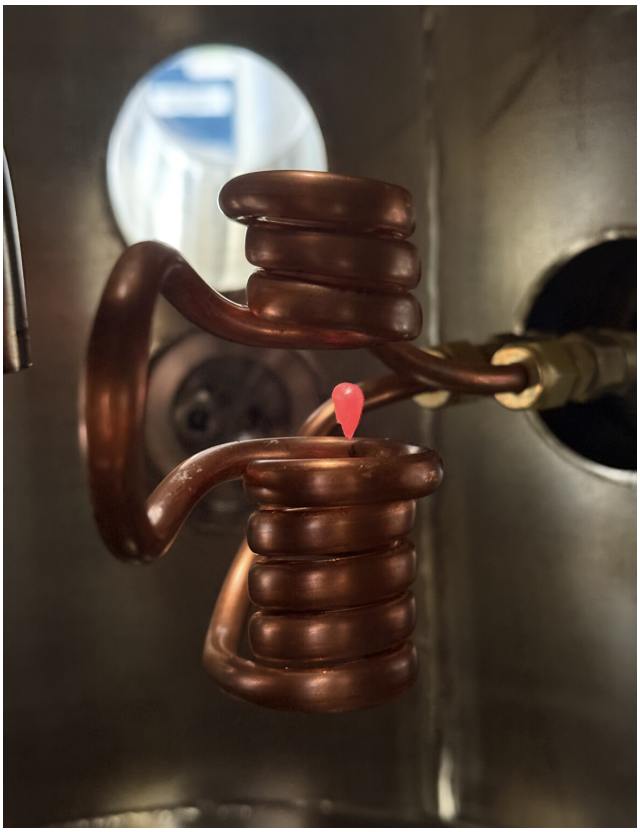

Figure 2.1 : Dramatic Sample Deformation Observed in Land-Based Electromagnetic Levitators

Samples are processed remotely from the Microgravity User Support Center (MUSC) in Cologne, Germany, and are operated by the German agency DLR [14]. At the MUSC, test parameters such as temperature ramp rate, and heater stimulation time can be varied to optimize experimental conditions.

For surface tension derivation, all required data are recorded by a pyrometer, which measures sample temperature, and two high-speed cameras positioned on the axial and radial views of the test apparatus [14, 15]. The ISS-EML contains a chamber that can hold eighteen samples at a time, called a batch. The gold sample being studied is part of Batch 4. To date, more than 2000 experiments have been performed on the ISS-EML [14]. A schematic of the ISS-EML is shown in Figure 2.2 with description of module functions in Table 2.1.

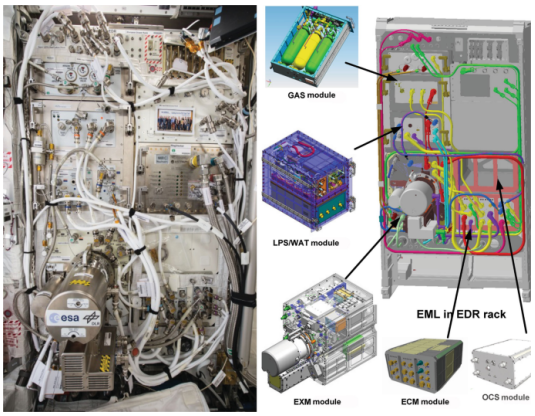

Figure 2.2 : Photo of the Physical ISS-EML Arrangement with Labeled CAD Diagram of the ISS-EML Modules [1]

The physical basis for EMLs is the Lorentz force. Alternating current within the EML coils induces varying magnetic fields that create eddy currents within the molten droplet. This field then interacts with the eddy currents to levitate the sample through the Lorentz force [16]. In addition to providing a mechanism to levitate the sample, the eddy currents create significant stirring within the sample itself. This stirring can cause difficulty in determining thermophysical properties, especially viscosity [12].

Table 2.1 : EML Modules and their purpose [1].

EML Module	**Main Function**
Gas Supply Module (GAS)	Storage and distribution of the noble gases
Levitation Power Supply (LPS) Water Pump Module (WAT)	Provision of RF voltage to the RF coil generating the electromagnetic fields. Secondary cooling loop to subsystems
Experiment Module (EXM)	Core experiment: comprising e.g. vacuum chamber, RF coil, diagnostics, mechanisms, samples
Experiment Controller Module (ECM)	Data management & control, power distribution

Electrostatic Levitation (ESL) and MSFC ESL

Installed in 1997 and continually improved since its installation, NASA Marshall Space Flight Center's electrostatic levitator has been a premier containerless solidification resource [17]. The MSFC ESL was designed for the testing of materials in a broad range of environments (10^{-8} torr to 5 atm) for thermophysical properties such as surface tension, viscosity, creep strength, and thermal expansion, as well as phenomena like nucleation and phase equilibria [17].

Located on the ground, the MSFC ESL does not benefit from the same microgravity advantages as the ISS-EML. Because of this, the MSFC ESL must maintain strong positioning forces via a static electric field [17]. This is done through a strong z-axis electric field, which levitates the charged sample, and relatively smaller x- and y-axis fields, which position it laterally. The use of electrostatic fields that levitate the sample through Coulomb's force, as op-

posed to electromagnetic fields, results in a quiescent sample that has little internal stirring. Notably, MSFC ESL samples are smaller than those of ISS-EML samples, typically with diameters of 1.5–3 mm and weights of 30–50 mg [17]. Because of this, terrestrial ESL experiments do not face the same droplet asymmetry issues as terrestrial EML testing.

Despite the smaller sample size, there are a multitude of factors that make levitating gold difficult in ground-based electrostatic levitators. The high density of gold causes samples to reach the operational limit [17]. This contributes to the large electrostatic fields needed to levitate the sample. This is exacerbated by gold's large work function, which makes it inherently difficult to create a surface charge sufficient to levitate the sample [9]. These large electrostatic fields cause the sample to move erratically as the sample loses impurities and their respective charges to evaporation [18]. Because of this, gold is primarily studied in microgravity environments with electromagnetic levitators.

2.2 Surface Tension

Derivation of surface tension in containerless processing involves basic knowledge of spherical harmonics and how it applies to the Rayleigh equation. This differs from other ways of experimentally determining surface tension, like the meniscus and pendant drop methods, which often cannot be used with metallic material.

2.2.1 Theory

Surface tension represents the excess energy at an interface and is a fundamental thermophysical property that governs many aspects of fluid dynamics

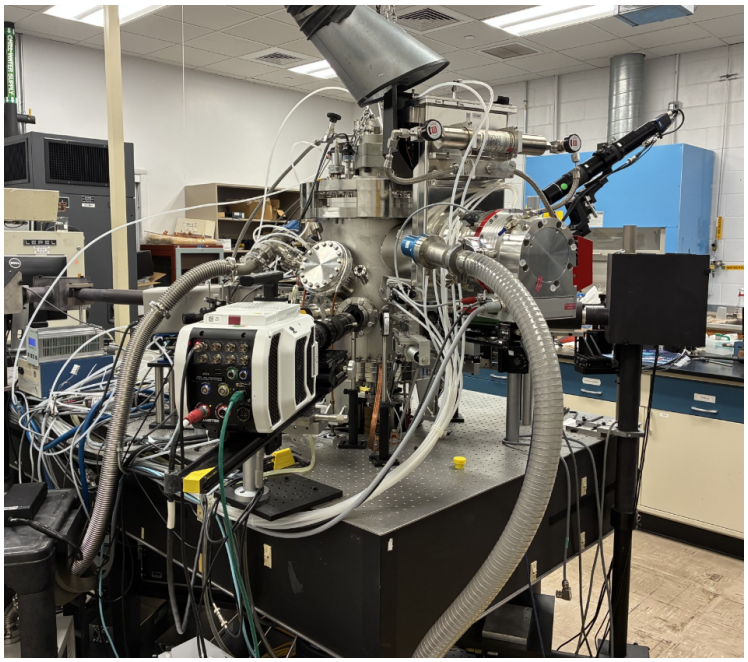

Figure 2.3 : Photo of MSFC ESL as of January, 2026

in natural and industrial contexts [19]. At its core, surface tension is closely tied to Gibbs free energy and represents the work required to increase a fluid's surface area at a given temperature and pressure [19]. This relationship is expressed by the following equation, where G is Gibbs free energy, A is the surface area of the fluid, and γ is the surface tension at temperature T, pressure P, and composition n [20].

$$\gamma = \left(\frac{\partial G}{\partial A}\right)_{T,P,n} \qquad \text{Surface Tension from Gibbs Free Energy} \qquad (2.1)$$

Additionally, the surface tension of a fluid decreases linearly with increasing temperature, a phenomenon known as the Eötvös Rule [21].

$$\gamma V^{2/3} = k_e(T_C - T) \qquad \text{Eötvös Rule} \qquad (2.2)$$

In this equation, V is the molar volume of the fluid, $k_e = 2.110^{-7}\ J/K$ is the Eötvös constant, and T_C is the critical temperature of the material where the fluid exhibits no surface tension [21, 22]. Previous experimental results for gold have shown deviations from this principle. Below temperatures of 1480 K, the surface excess entropy—the amount of entropy associated with an interface beyond the entropy of the bulk volume—changes by an order of magnitude, suggesting structural changes in the gold surface at higher temperatures [23].

2.2.2 Rayleigh Equation

The Rayleigh equation relates a material's natural frequency of vibration, ν, to its surface tension [24].

$$\gamma = \frac{3\pi\nu}{\ell(\ell-2)(\ell-1)} \qquad \text{Rayleigh Equation} \qquad (2.3)$$

In this equation, ℓ represents the mode of deformation of the material. When levitating a material, the sample assumes a spherical geometry to minimize surface energy. When stimulated—in the case of the ISS-EML, through electromagnetic fields—the sample enters a new mode of deformation, characterized by a change in shape [24].

Table 2.2 : Low-order oscillation modes of a liquid droplet characterized by the spherical harmonic index ℓ [2].

Mode (ℓ)	**Name**	**Physical Description**
0	Breathing Mode	Uniform Sphere
1	Translational Mode	Dipole oscillation across the sphere
2	**Fundamental Mode**	**Shape oscillation between prolate and oblate ellipsoids**
3, 4, ...	Higher-Order Modes	Higher resolution, more complex, and more frequent oscillations

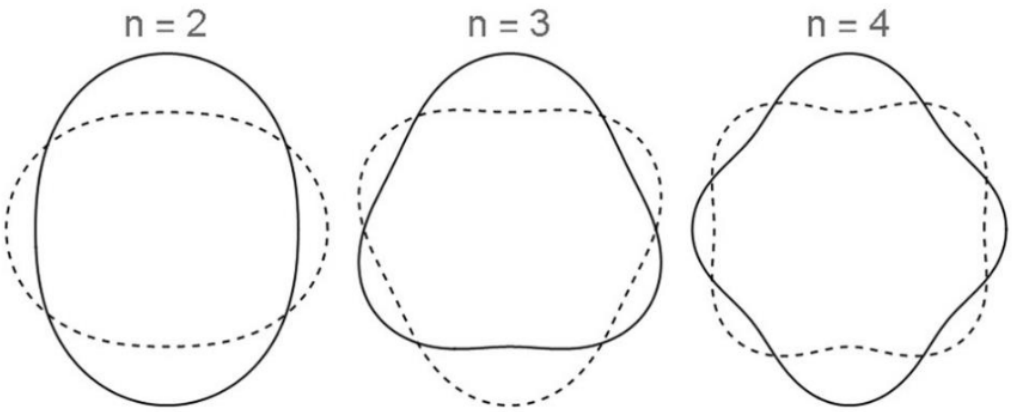

Figure 2.4 : Representation of Spherical Harmonics Ranging from $\ell = 2$ to $\ell = 4$ [5]

The predominant mode of deformation used for studying droplets on the ISS-EML is $\ell = 2$. Lord Rayleigh deduced that the frequency of the $\ell = 2$ mode is determined by the balance between the sample's inertia (mass) and its restoring force (surface tension) [2, 25].

$$\omega^2 = \ell(\ell - 1)(\ell + 2)\frac{\gamma}{R^3\rho}$$

Substituting $\ell = 2$ and $\omega = 2\pi\nu$ yields:

$$(2\pi\nu)^2 = \frac{8\gamma}{R^3\rho}$$

Finally, assuming spherical geometry and substituting mass for density yields the Rayleigh equation for mode $\ell = 2$:

$$\gamma = \frac{3}{8}\pi m\nu^2 \qquad \text{Rayleigh Equation } (\ell = 2) \qquad (2.4)$$

2.2.3 Experimental Measurement

Ivan Egry studied surface tension of gold aboard the Columbia Space Shuttle using the TEMPUS electromagnetic levitation facility. Egry notes the increased fidelity of using spherical harmonics in a microgravity environment due to the reduced deformation seen [6, 3]. Egry's results yield a relationship between surface tension and temperature expressed as:

$$\gamma = 1.149 - 0.00014(T - T_m)\ N/m$$

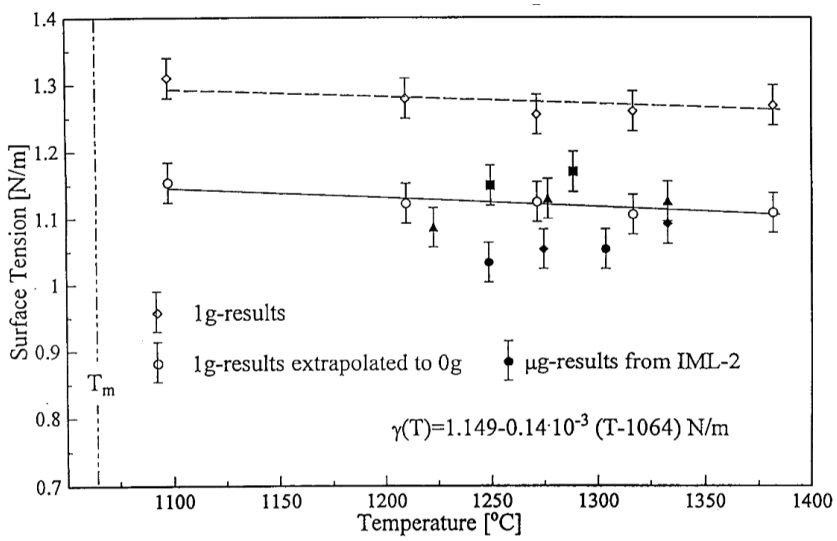

Figure 2.5 : Plot of Egry's surface tension results for gold in microgravity and ground-based experiments [3, 6]

Egry's results compare well to corrected measurements taken a year before at 1-g, as can be seen in Figure 2.5. Additionally, using the surface temperature at the melting point as a method of comparison, Egry's results correspond remarkably well to results published by B.J. Keene, who details a surface tension relationship of [4, 3]:

$$\gamma = 1.145 - 0.00020(T - T_m)\ N/m$$

Pendant Drop

The Pendant Drop Method uses optics to determine surface tension and interfacial tension by analyzing the profile of a liquid droplet suspended from a needle [26]. The shape of the droplet is governed by the Young-Laplace Equation, which describes the pressure difference across a curved interface [27, 28].

$$\Delta P = \gamma \left(\frac{1}{R_1} + \frac{1}{R_2} \right) \qquad \text{Young-Laplace Equation} \qquad (2.5)$$

It has been shown that the shape of a pendant drop is dependent on only the Bond number, a dimensionless parameter that relates gravitational forces to surface tension forces [29]

$$Bo = \frac{\rho g R^2}{\gamma} \qquad \text{Bond Number} \qquad (2.6)$$

There are regimes in which the pendant drop technique fails. In situations where the Bond number far exceeds one, the surface tension force is too low to sustain a stable droplet. Conversely, when the Bond number approaches zero, surface tension dominates and the drop does not deform, making analysis impossible. These such cases necessitate the use of other measurement techniques [29].

Meniscus

The meniscus technique focuses on the forces brought on by surface tension as its method of measurement. When a solid probe—commonly a Wilhelmy Plate or a Du Noüy ring— touches a liquid surface, the liquid wets the probe and forms a meniscus [30, 31].

The Wilhelmy Plate method is the most common method of force-based meniscus methods. It uses a thin plate, typically made of platinum or glass, as the probe. The measured surface tension is dependent on the wetted perimeter, $L = 2l + 2t$, and the contact angle, θ, between the probe and the liquid. The net force acting on the probe is comprised of two forces: the weight of the meniscus and the buoyancy force. The weight of the meniscus must be isolated by controlling the buoyancy force. The plate is often roughened to ensure perfect wetting, characterized by a contact angle of $\theta = 0$ [31].

$$\gamma = \frac{F}{L \cdot cos(\theta)} \qquad \text{Wilhelmy Plate Method} \qquad (2.7)$$

The Du Noüy ring method submerges a platinum-iridium ring in a liquid and records the maximum force experienced while pulling the ring from the liquid, typically experienced right before the meniscus ruptures. Analysis of the Du Noüy method is complicated by a correction factor, f, that accounts for the fact that the meniscus has both an inner and outer radius [32].

$$\gamma = \frac{F_{\max}}{4\pi R} \cdot f \qquad \text{Du Noüy Method} \qquad (2.8)$$

2.3 ISS-EML Heater

The heating coil on the ISS-EML stimulates the sample and also deforms it. This deformation effects the derivation of surface tension and can be quantified, allowing for the correction of surface tension. This correction is vital to the fidelity of surface tension results.

2.3.1 Capabilities and Purpose

The ISS-EML heater serves two distinct purposes in experimentation: heating and stimulating the sample [1]. It can provide a heating rate up to 100 K/s and is tunable by adjusting the voltage in the coil. By varying the voltage within the coil, samples can also be effectively stimulated to create oscillations.

There are two main methods of creating oscillations within a sample. One method involves introducing a sharp 0.1-second voltage impulse, while the other, Faraday excitation, sweeps the voltage sinusoidally for a longer duration with lower amplitude than the impulse method [1]. Traditionally, EML studies focus on impulse excitation while ESL studies utilize Faraday excitation [1, 17]. This study serves as the first large-scale application of Faraday excitation in ISS-EML testing. As such, a primary focus of this study is evaluating the suitability of Faraday Excitation in the ISS-EML environment. Both methods of stimulating samples are tunable, with characteristics such as amplitude, frequency, and sweep duration adjustable between experimental runs.

2.3.2 Effect on Deformation

Because microgravity effectively eliminates sample deformation due to gravity, the main source of sample deformation is the ISS-EML heater, with an additional contribution from the positioner coil [1]. The heater and positioner coils are decoupled in the ISS-EML to simplify the governing physics of the system [14]. The fields also differ in their implementation: the heater operates as a dipole field running from the bottom to the top of the sample, while the positioner uses a quadrupole field that runs tangent to the sample and pro-

duces larger, symmetrical forces [1].

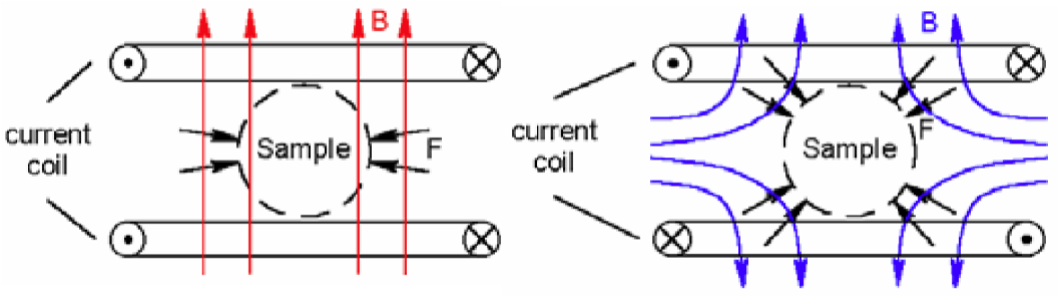

Figure 2.6 : Dipole EML Heating Field (Red) and Quadruple Positioning Field (Blue) and Associated Forces on the Sample [1]

In contrast, the forces acting on the sample created by the heater field are asymmetrical, being concentrated along the equator of the sample. This produces a net squeezing effect on the sample that efficiently creates oscillations [1]. Because of this squeezing effect, in certain ISS-EML experiments, the heater is turned off and testing is conducted as the sample cools to mitigate net deformation. However, other experiments are conducted at constant temperature to provide precise tracking of how thermophysical properties change with temperature [33]. In such cases, establishing a concrete relationship between the constant heater voltage and property derivation is paramount, which motivates this study.

Table 2.3 : Comparison of positioning and heating electromagnetic fields on the ISS-EML [1].

Feature	**Positioning Field**	**Heating Field**
Field Type	Quadrupole type	Dipole type
Frequency	Approximately 140 kHz	Approximately 380 kHz
Primary Effect	High positioning force with low heating efficiency	High heating efficiency with low forces on the sample

2.3.3 Deformation Induced Frequency Shift

The Rayleigh equation may not be appropriate at large deformation amplitudes. At these larger deformations—typically 1% and above—a notable decrease in natural frequency is observed that is independent of temperature [34]. To account for this effect, a curve fit is employed for all frequency data. This curve fit contains a linear dimensionless temperature term $\theta = T/T_m$ with associated weight p_θ, and a parabolic deformation term where δ represents the deformation and p_1 and p_2 represent weights for the linear and parabolic deformation terms, respectively [34].

$$\nu_c = \nu_{\theta=0}(1 + p_\theta\theta)(1 + p_1\delta + p_2\delta^2) \quad \text{Corrected Frequency Formula} \quad (2.9)$$

The corrected frequency, ν_c, approaches the Rayleigh frequency of the material, ν, at an arbitrary temperature as the deformation approaches zero [34]. Because surface tension has a well-documented dependence on temperature, as evidenced by the Eötvös rule, it is useful to remove this factor and study the effect of deformation in isolation. This is accomplished using the frequency shift ratio:

$$\frac{\nu_c - \nu}{\nu} = p_1\delta + p_2\delta^2 \quad \text{Frequency Shift Ratio} \quad (2.10)$$

Because frequency decreases with deformation, the frequency shift ratio yields negative values, particularly for larger deformations. Positive values may result from noise at small deformations, as the deformation effect is less pronounced [34].

Solving for ν_c in the above equation and substituting into the Rayleigh equa-

tion yields a corrected formula that accounts for frequency shift in measured frequency values:

$$\gamma = \frac{3}{8}\pi m\nu^2(1 + p_1\delta + p_2\delta^2) \qquad \text{Corrected Rayleigh Equation} \qquad (2.11)$$

2.4 Temperature Measurement

During testing, the sample temperature is recorded using a pyrometer. Pyrometers are remote-sensing devices that determine the temperature of a surface by measuring the thermal radiation emitted by that surface [35]. The key advantage of this method is the ability to measure temperature without disturbing the sample [36]. This both preserves the contactless nature of containerless solidification and keeps instruments outside the testing chamber. Determination of temperature allows for a relationship between surface and temperature to be defined.

Pyrometry is based on the fundamental principle that all objects above absolute zero emit electromagnetic radiation. This relationship is governed by Planck's law, which relates the spectral radiance of a black body, $B(\lambda, T)$, to a particular wavelength, λ, and absolute temperature, T. In the following equation, h is Planck's constant, k is the Boltzmann constant, and c is the speed of light [35].

$$B(\lambda, T) = \frac{2hc^2}{\lambda^5}\frac{1}{e^{\frac{hc}{\lambda k T_b}} - 1} \qquad \text{Planck's Law} \qquad (2.12)$$

Planck's law shows that, for a given wavelength, as the temperature of a black body increases, the spectral radiance also increases. In single-color pyrometry, only the radiance at one specific wavelength is recorded, effectively making

radiance a function of temperature alone [35]. Planck's law can be simplified further when the exponent $\frac{hc}{\lambda kT} \gg 1$. In this regime—applicable when $\lambda T < 2082\,\mu m \cdot K$ for less than 0.01% error—the exponential dominates the denominator, allowing simplification. This approximation is particularly useful in the study of gold, where the emitted radiation lies in the infrared to visible light spectrum [37].

$$B(T) = \frac{2hc^2}{\lambda_{\text{eff}}^5} e^{-\frac{hc}{\lambda_{\text{eff}} kT_b}} \qquad \text{Wien's Approximation} \tag{2.13}$$

Despite these simplifications, the samples aboard the ISS-EML are not perfect black bodies, and post-processing of the data must be conducted to determine the correct sample temperatures [35]. Emissivity values are programmed into the pyrometer but rarely match those of the actual material. The spectrum recorded at a reference temperature, B_0 at T_{b0}, can be used to calibrate the pyrometer to the correct value. The reference temperature chosen is often the liquidus temperature of the material, T_L. The true value of this temperature is well documented for materials like gold and is easily identified after recalescence from the undercooled state [38]. Taking the ratio of an instantaneous spectral radiance recording, B, to the reference spectral radiance, B_0, yields:

$$\frac{B}{B_0} = \frac{\frac{2hc^2}{\lambda_{\text{eff}}^5} e^{-\frac{hc}{\lambda_{\text{eff}} kT_b}}}{\frac{2hc^2}{\lambda_{\text{eff}}^5} e^{-\frac{hc}{\lambda_{\text{eff}} kT_{b0}}}}$$

This can be simplified by cancelling like terms and combining exponentials:

$$\frac{B}{B_0} = e^{-\frac{hc}{\lambda_{\text{eff}} kT} + \frac{hc}{\lambda_{\text{eff}} kT_0}}$$

Taking the natural logarithm yields:

$$\ln\left(\frac{B}{B_0}\right) = -\frac{hc}{\lambda_{\text{eff}}k}\left(\frac{1}{T_b} - \frac{1}{T_{b0}}\right)$$

It should be noted that both T_b and T_{b0} are black body temperatures and must be corrected for the sample's emissivity. This can be achieved through the definition of a grey body, $B_\lambda^{bb}(T_b) \cdot \epsilon_\lambda = B_\lambda^{gb}(T)$ [35]. Solving for the black body temperature, T_b, yields:

$$\frac{1}{T_b} = \frac{1}{T} - \frac{\lambda}{hc}\ln(\epsilon_\lambda) \qquad \text{Definition of a Grey Body} \qquad (2.14)$$

Applying Equation 2.14 to the above derivation converts black body temperatures to grey body temperatures and results in:

$$\ln\left(\frac{B}{B_0}\right) = -\frac{hc}{\lambda_{\text{eff}}k}\left(\frac{1}{T} - \frac{1}{T_0}\right) + \ln\left(\frac{\epsilon_\lambda}{\epsilon_{\lambda 0}}\right)$$

The emissivity term reduces to zero under the assumption that both the instantaneous emissivity, ϵ_λ, and the reference emissivity, $\epsilon_{\lambda 0}$, are identical.

By equating the ratio of spectral radiances $\frac{B}{B_0}$, which represents the ratio of an instantaneous radiance reading to a reference state, to the ratio of an instantaneous pyrometer reading to the pyrometer's reading at the liquidus temperature, $\frac{B_P}{B_{PL}}$, the final temperature correction equation can be derived:

$$\ln\left(\frac{B}{B_0}\right) = \ln\left(\frac{B_P}{B_{PL}}\right)$$

$$\frac{hc}{\lambda_{\text{eff}}k}\left(\frac{1}{T} - \frac{1}{T_L}\right) = -\frac{hc}{\lambda_{\text{eff}}k}\left(\frac{1}{T_P} - \frac{1}{T_{PL}}\right)$$

$$\left(\frac{1}{T}-\frac{1}{T_L}\right)=\left(\frac{1}{T_P}-\frac{1}{T_{PL}}\right) \qquad \text{Pyrometry Correction Equation} \qquad (2.15)$$

Because of the dependence on the pyrometer's reading at the liquidus temperature, it was essential that all individual experimental runs included recordings of the recalescence temperature after undercooling.

2.5 Fluid Velocity in EML Testing

Understanding the fluid velocity in EML testing is crucial, as it dictates the derivation of material properties and solidification of molten elements and alloys [13]. This inner fluid flow is instilled by the ISS-EML heater, and is more pronounced in Faraday Forcing experiments as a result of the heater being present throughout the entire test [13]. Quantification of surface tension is found through a surrogate model where there are contributions from both the heater and positioner coils [12]. This model, defined below, is used to quantify the fluid velocity, and thus, Reynolds number, throughout the thesis to determine the effects of fluid velocity and stirring.

This flow is primarily driven by the Lorentz force induced by the electromagnetic field of the ISS-EML's heater coils [13]. The flow regime is dictated by the Reynolds number, where ρ is the density of the material, u is the flow velocity, d is the diameter of the droplet, and μ is the dynamic viscosity of the material. For EML droplets, turbulent flow is first found at Reynolds numbers ranging from 500 to 600 [12].

$$Re=\frac{\rho u d}{\mu} \qquad \text{Reynolds Number} \qquad (2.16)$$

Gold in particular is susceptible to turbulent flow in EML testing [12]. Baker *et al.* found that when the EML heater is active, the Reynolds number for gold exceeds 600 across nearly all temperatures and heater control voltages, U_{ctr}^{H}, and only at very low positioner voltages and significant undercooling was molten gold observed to be laminar [12]. However, it should be noted that the velocity fields created by the positioner and heater counteract each other. This effect, investigated by J. Lee *et al.*, is shown in Figure 2.7 and is a consequence of the positioner and heater magnetic fields acting on the droplet in different manners, as was seen in Figure 2.6 [39]. This becomes especially important at low heater control voltages, where the heater does not entirely dominate. Velocity streamline plot a) in Figure 2.7 shows a heater control current, I_H, of 0, corresponding to a heater control voltage of 0, creating a significant clockwise vortex. This is counteracted by a counter-clockwise vortex created by the introduction of the EML heater in velocity streamline plots b), c) and d) [39].

Because of this, the internal velocity of the droplet is found by subtracting the contribution to the velocity from the positioner from that of the heater. The internal velocity must be calculated using surrogate models that use magnetohydrodynamic simulations. These simulations utilize least squares regression to fit raw data and create coefficients—p_{ijks} for the positioner and q_{ijks} for the heater—that best characterize sample behavior [40, 13]. These coefficients are specific to flow regime (laminar or turbulent), and as such, should be used to quantify velocity based on the expected flow regime. These tabulated coefficients can be found in the *Supplementary Information* section of *MHD surrogate model for convection in electromagnetically levitated molten metal droplets processed using the ISS-EML facility* by Baker *et al.* [12]. The indices

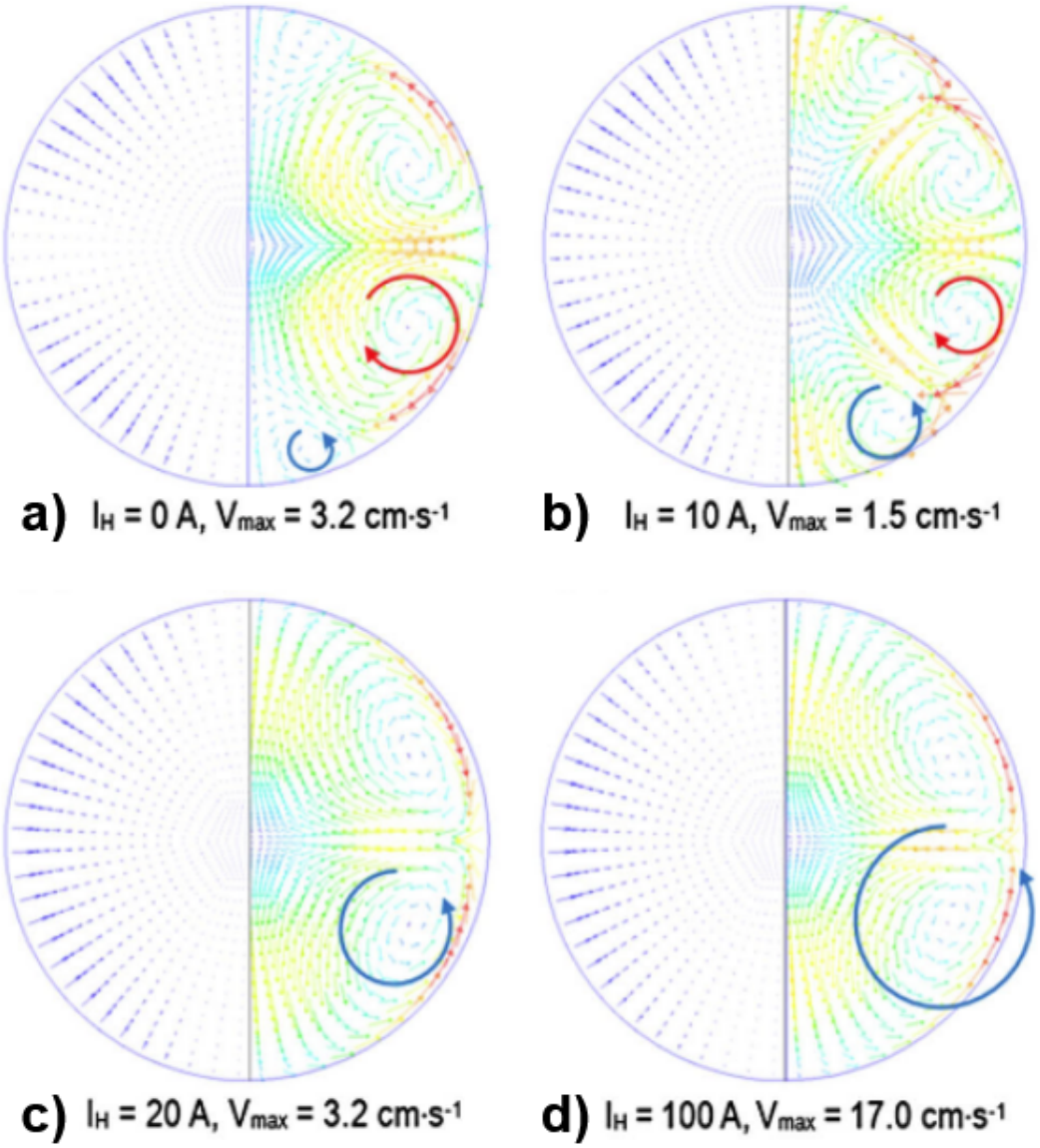

Figure 2.7 : Velocity Fields of $Fe_{50}Co_{50}$ for different heater control currents

represent the different contributions of thermophysical properties, with i, j, k and s representing the contributions from the heater control voltage, density, viscosity and electrical conductivity respectively for the heater model, and positioner voltage, electrical conductivity, density and viscosity respectively for the positioner model. This culminates in the following model, which characterizes the maximum fluid velocity within the sample when the heater coil and

positioner coil is on [40, 13, 12].

$$u_{\max}, \dot{\gamma}_{\max} = \sum_{i,j,k,s} q_{\text{ijks}} \cdot \left(U_{\text{ctr}}^{H}\right)^{i} \cdot \rho^{j} (\ln \mu)^{k} \cdot (\ln \sigma_{\text{el}})^{s} \qquad \text{Heater Velocity} \tag{2.17}$$

$$u_{\max}, \dot{\gamma}_{\max} = \sum_{i,j,k,s} p_{\text{ijks}} \cdot \left(U_{\text{ctr}}^{P}\right)^{i} \cdot \left(\frac{1}{\sqrt{\sigma_{\text{el}}}}\right)^{j} \cdot \left(\rho^{k}\right) \cdot \left(\frac{1}{\ln(\mu)}\right)^{s} \quad \text{Positioner Velocity} \tag{2.18}$$

In this model, ρ represents density, μ represents the dynamic viscosity and σ_{el} represents the electrical conductivity of the material.

In addition to heater control voltage, the surrogate models are dependent on the electrical conductivity, density and viscosity of the metallic droplet. The electrical conductivity and density were found from the gold sample tested. For viscosity, values from literature are used. The material properties and their relationship with temperature are shown in Table 2.4. Derivation of the electrical conductivity and density are shown in Appendix G and was completed by Professor Douglas Matson and Dr. Peace Muusha. In the following definition of viscosity, μ_0 can be obtained using literature values of the viscosity at the melting temperature. For gold, it can be derived by the following, where $\mu_m = 5.37\ mPa \cdot s$ is the viscosity at the melting temperature, R is the gas constant in SI units and T_m is the melting temperature [41].

$$\mu_0 = \frac{\mu_m}{\exp(\frac{2.65 T_m^{0.27}}{R})} = 0.57976\ mPa \cdot s$$

Internal droplet velocity is more impactful in viscosity measurements as a re-

Table 2.4 : Material Properties Used in the Velocity Surrogate Model

$\mu\ (Pa \cdot s)$ [12]	$\rho\ (kg \cdot m^{-3})$	$\sigma_{\text{el}}\ (S \cdot m^{-1})$
$\mu_0 \exp\left(\frac{2.65T_m^{1.27}}{RT}\right)$	$17233 - 1.168(T - T_m)$	$(2.500 \cdot 10^{-7} + 4.937 \cdot 10^{-11}(T - Tm))^{-1}$

sult of the characteristic mixing associated with a larger Reynolds number. This mixing decreases the damping time of the droplet oscillations, τ, which is used in determining fluid viscosity [12]. As a result, investigators focus of low Reynolds number, $Re < 500$, for viscosity experiments [12]. Stirring is thought to have minimal effects on the derivation of surface tension. This relationship is ill-defined however, with no formal study focusing on the relationship. It has been shown that decreasing positioning and heater control voltages $U^P_{\text{ctr}}, U^H_{\text{ctr}}$, leads to increased fidelity in experimental measurements [13]. Additionally, in EML environments, the induced flow within the droplet may vary significantly locally [13]. These effects, however significant, lead to changes in property derivation that is currently unstudied.

There exists a significant difference in how stirring affects testing, depending on which excitation method is being used. In traditional EML testing, where the sample is hit with a short impulse of heater voltage, heater-induced stirring is only present for a short time, while positioner-induced stirring, which is less powerful, continues throughout the remainder of testing. Because of this, the Reynolds number is not consistent throughout testing, and the direction of fluid flow can change if testing is prolonged enough. Conversely, in Faraday excitation, which is typical of ESLs, the heater remains at a constant voltage even after excitation is finished.

Chapter 3

Methods

3.1 Sample Preparation

The following is an excerpt from the sample preparation procedure written by Professor Doug Matson for the gold sample that was used in this study.

"All sample preparation was conducted in air, as gold is a noble metal and inert to oxidation, at master goldsmith James Binnion Metal Arts in Bellingham WA USA. The samples were prepared from raw wire stock. The as-received material was sectioned, rinsed in 99% isopropyl alcohol to desiccate surfaces to remove any ambient water, air-dried and placed in a ceramic crucible which served as the ingot mold.

Figure 3.1 shows preparation of the blank for machining. A master-alloy ingot was prepared by induction melting and then removing the central pipe, or porous central region from solidification shrinkage, and minimize the shrinkage cavity at the top of the ingot by using an induction Bridgeman furnace technique. Upon cooling, the ingot was rolled in a wire mill down to a 6.4 mm octagonal section. Leading and trailing ends of the ingot were trimmed with a jewelers saw, and the resulting blank was cut into sections to provide enough material for each sphere. Cut sections were then press-fit in a die cavity to form a 6.74 mm diameter blank with a hemispherical end. Note that this blank intentionally has a larger diameter than the desired final sphere dimension of

6.50 mm to ensure that any blank-preparation contaminants are removed from the final sample surface during lathe machining operations.

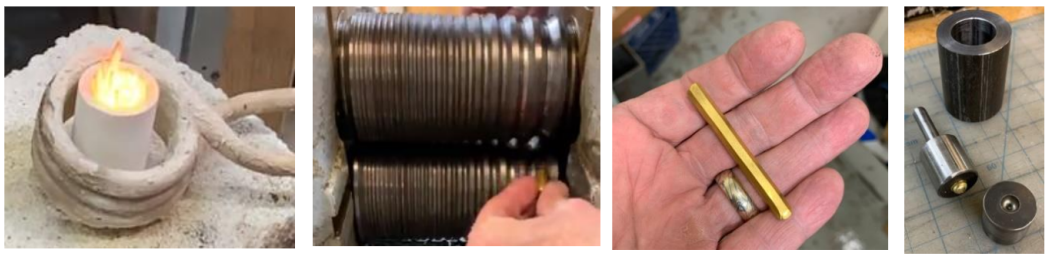

Figure 3.1 : Preparation of the Ingot Blank Showing Induction Melting, Ingot Rolling, Ingot Trimming and the Creation of the Press Fit Blank

Figure 3.2 shows the machining operations. The blank was glued into a steel fixture with Loctite EA615 epoxy to allow the blank to be turned on the lathe. Once the epoxy was cured, the fixture with the gold blank was mounted in a lathe, and a hemisphere was turned on the exposed flat end of the blank. The gold blank was removed from the fixture by heating it with a torch until the epoxy released it. The partially machined blank was measured and then returned to the fixture with the machined end glued into the fixture. Once the epoxy was cured, the fixture was returned to the lathe to remove the final amount of material resulting in a spherical sample.

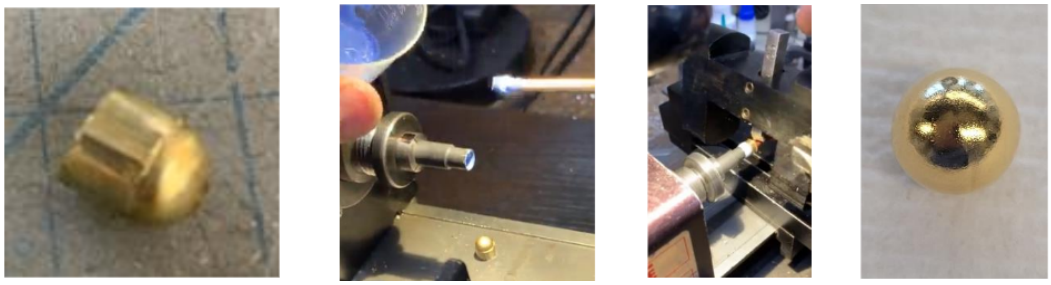

Figure 3.2 : Machining of Sphere Showing the Press Fit Blank, Blank Adhesion Tool, Lathe Machining and the Final Sample

After turning, the sphere was re-released from the fixture with a torch and

then placed in a vibratory tumbler with an abrasive-loaded plastic media for 12 hours to remove the machining toolmarks. After abrasive tumbling, the spheres were run in a magnetic pin tumbler with stainless steel pins to burnish the surface. After burnishing, the spheres were soaked in a 10% HCl solution for 30 minutes to remove any residual metals from machining and burnishing and then rinsed with water from a reverse osmosis (RO) cleaning system. The spheres were then placed in an ultrasonic cleaner with a 2% Citranox solution for 10 minutes and then rinsed with RO water. A final rinse with 99% isopropyl alcohol was applied to desiccate the samples, then followed by air drying, labeling, and packaging for shipping" [42].

3.2 Faraday Forcing

Samples were excited using Faraday Forcing, a technique that involves applying a sinusoidal voltage pattern to the heater coil. Larger deformations are observed when the voltage input has a frequency close to the material's natural frequency. Early Faraday Forcing tests on the sample were devoted to determining appropriate voltage input characteristics, such as frequency and duration. It was determined that applying the impulse for 2.1 seconds at a frequency of 18.6 Hz with an amplitude of 0.2 V provided optimal results for analysis.

The ISS-EML has two high-speed cameras positioned on both the axial and radial views of the test chamber [14, 1]. In $\ell = 2$ deformation, these views observe different manifestations of deformation, and as such, deformation must be defined differently for each view. The camera on the top view observes a circular cross-section of the sample that undergoes cycles of expanding and

contracting radius, while the side view observes an ellipsoidal cross-section of the sample that undergoes cycles of oblate and prolate geometry. Together, the volume of an oscillating ellipsoidal droplet can be defined in terms of the equatorial radius, R_w, and the polar radius, R_L, and related to the stationary droplet radius, R_0:

$$V = \frac{4}{3}\pi R_L R_w^2 = \frac{4}{3}\pi R_0^3 \qquad \text{Volume of Oscillating Droplet} \qquad (3.1)$$

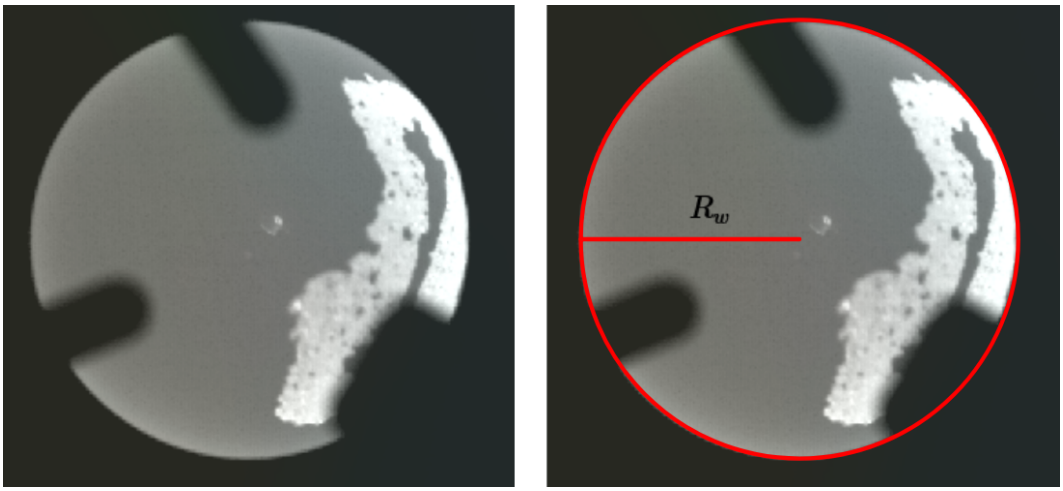

Figure 3.3 : Unthresholded Top View Frame Without (Left) and With (Right) Ellipsoidal Curve Fit

Videos recorded by the high-speed cameras are post-processed to obtain precise information about sample cross-sectional area. A threshold filter is applied to the high-speed camera video to separate the sample from the surrounding chamber [1]. High contrast exists between the sample and chamber in the raw test video, making simple thresholding effective at delineating the sample from the background. The sample in each frame of the thresholded video is then fitted to the equation of an ellipse. This is necessary because the testing appa-

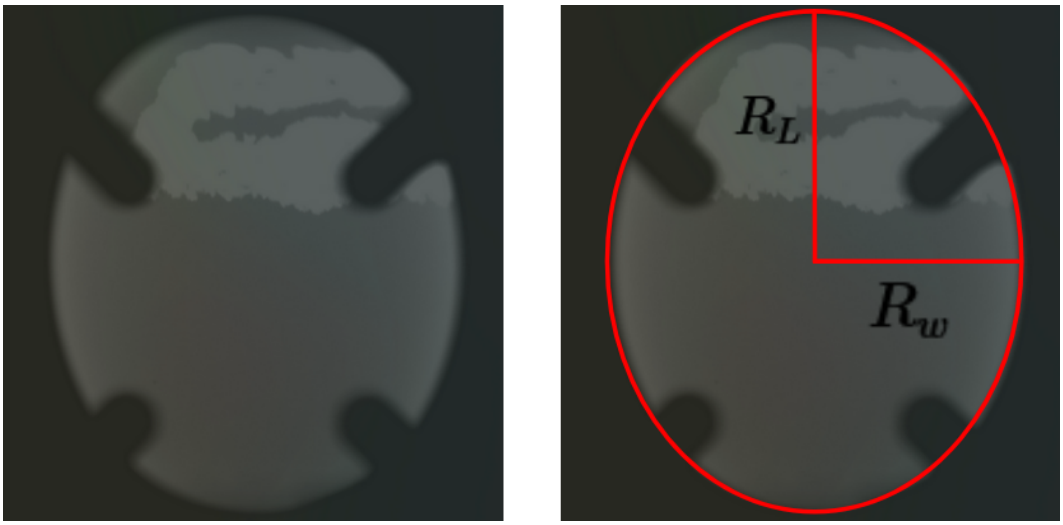

Figure 3.4 : Unthresholded Side View Frame Without (Left) and With (Right) Ellipsoidal Curve Fit

ratus of the ISS-EML protrudes into the video frame. Consequently, counting the number of thresholded pixels does not fully capture the true area of the sample. The ellipsoidal fit also enables the determination and storage of radii values. For top view videos, this yields the instantaneous equatorial radius, and for side view videos, this yields both the instantaneous equatorial radius and polar radius for each frame of the video.

Samples are stimulated with respect to a median heater control voltage (U^H_{ctr}). Crucially, this heater control voltage determines the level of constant deformation that the sample experiences. If a sample is stimulated at an heater control voltage of 1.0 V, the sample experiences significantly more force from the heater than a sample excited at a lower voltage. This provides the method for determining the effect of deformation on surface tension derivation.

Table 3.1 shows the experimental test matrix of the different heater control

voltage values tested. Testing characteristics were determined at an U^H_{ctr} of

Table 3.1 : Experimental Test Matrix

U^H_{ctr} (V)	**Number of Runs**	**Run Number(s)**
0.3	4	31, 32, 33, 34
0.5	1	36
0.6	2	37, 38
0.8	1	39
1.0	1	40

0.3 V, resulting in more tests conducted at that voltage level. Run number 35—tested at an U^H_{ctr} 0.3 V—was excluded from analysis due to sample solidification during oscillation, and run number 37—tested at an U^H_{ctr} 0.6 V—was discarded due to a noisy signal. Additionally, cycles 31 and 36 only have associated top view data. Only one test was conducted at each U^H_{ctr} above 0.3 V to prioritize other experimental initiatives.

During Faraday Forcing, the sample oscillates at the forced frequency of 18.6 Hz. When the voltage oscillations cease and the heater control voltage remains constant, the sample freely oscillates at its natural frequency, which decreases with both temperature and deformation. These free oscillation frequencies are used to determine thermophysical properties and are seen in Figure 3.5.

3.3 Data Segmentation

Typically, a fast Fourier transform (FFT) is used to determine the frequency of data, especially for large datasets. However, the frequency of the dataset changes with deformation and temperature, requiring evaluation of smaller data subsets. These smaller subsets are defined as 60 points for the top view

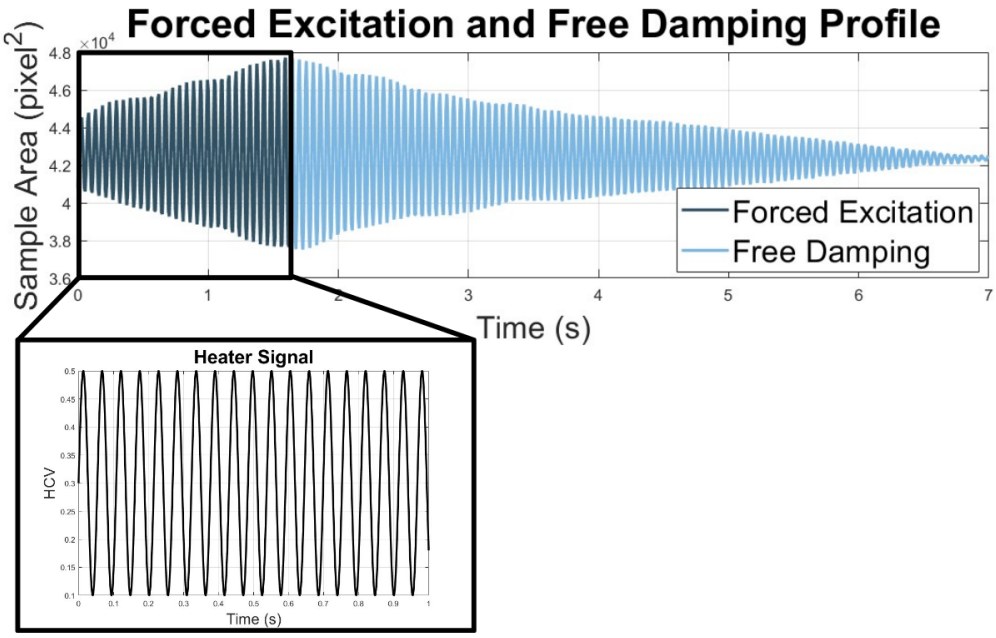

Figure 3.5 : Plot of Forced (Dark Blue) and Free Oscillations (Light Blue) within Sample and Heater Control Value (Black) vs. Time (s) for Cycle 32 Top View

and 160 points for the side view. This limits the effectiveness of FFT's resolution, which is defined as f_s/N, where f_s is the sampling rate and N is the number of data points [34]. To address this limitation, Levenberg-Marquardt least squares curve fitting is employed to determine oscillation characteristics. The equation being fit is an exponentially decaying sinusoidal wave:

$$y = Ae^{-t/\tau}\sin(2\pi\nu + \phi) + D \qquad \text{Curve Fit Equation} \qquad (3.2)$$

where A is the amplitude of the oscillation wave, τ is the decay time, ν is the frequency, ϕ is the phase offset, and D is the mean offset from zero signal. In top view videos, when the curve fit, y, represents the projected area of the sample, D represents the mean cross-sectional area of the sample as it oscillates. In side view videos, when the curve fit, y, represents the change in

radius, D is roughly zero. Figure 3.6 shows a side view signal, y, at many time points, t with fitted parameters showcased. Because it is a side view signal, the mean offset, D, is near zero. Damping parameter, τ, while not labeled, represents the reduction of amplitude, marked by the dashed black lines.

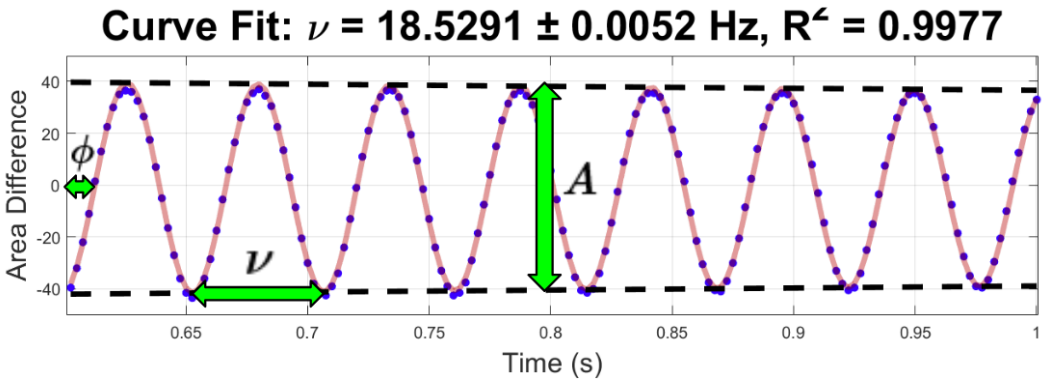

Figure 3.6 : $y = Ae^{-t/\tau}\sin(2\pi\nu + \phi) + D$ Applied to Sample Dataset with A, ν and ϕ Labeled For a Side View Signal

Each data segment is 0.4 seconds long and represents a temperature change of roughly 5 K. Each segment overlaps 80% with the previous segment. Overlapping analysis is used in EML data analysis to fully capture the state of stirring within the sample. As the sample cools, the flow regime within the sample may change, signified by the decreased in Reynolds number. Overlapping analysis allows for this transition to be more accurately monitored [34, 43].

Initial guesses and bounds are critical for ensuring that the curve-fitting algorithm reaches valid results. The initial guess is used in the first iteration of the algorithm, and bounds are used to determine the range of acceptable fitted parameters. In the following definition of guesses and bounds, x represents the values of the segmented signal, t represents the time duration of the segment, and subscript i refers to the current iteration.

Table 3.2 : Initial Guesses and Lower and Upper Bounds for Iterative Levenberg-Marquardt Algorithm

	A	τ	ν	ϕ	D
Initial Guess	$\max(x) - \text{mean}(x)$	t	18.62	0	$\text{mean}(x)$
Lower Bound	0.1	$0.3 \cdot t$	$0.8\,\nu_{i-1}$	$-\pi$	$\min(x)$
Upper Bound	1.5 max(segment)	$3 \cdot t$	$1.2\,\nu_{i-1}$	π	$\max(x)$

3.4 Deformation Definition

3.4.1 Definition of Top View Deformation

The top view captures changes in equatorial radius, R_w, which result in a net change in cross-sectional area. For an oscillating droplet with deformation δ, the equatorial radius can be defined as:

$$R_w = (1 \pm \delta)R_0 \qquad \text{Equatorial Radius Definition} \qquad (3.3)$$

Because the top view captures cross-sectional area change, the fitted area data best supports analysis of top-view deformation. From this, we can equate fitted parameter D to the cross-sectional area of the sample when $R = R_0$, and fitted parameter $|A| + D$ to the deformed cross-sectional area of the sample. Note that the absolute value of parameter A is taken to ensure deformation is never negative. Under these assumptions, the equatorial radius definition becomes:

$$\sqrt{\frac{|A| + D}{\pi}} = (1 \pm \delta)\sqrt{\frac{D}{\pi}}$$

Solving for δ yields:

$$\delta = \sqrt{\frac{|A| + D}{D}} - 1 \qquad \text{Top View Deformation} \qquad (3.4)$$

3.4.2 Definition of Side View Deformation

The side view camera captures changes in polar radius, R_L, which can be defined as follows for an oscillating droplet:

$$R_L = (1 \pm \delta)^{-2} R_0 \qquad \text{Polar Radius Definition} \qquad (3.5)$$

From the side view, there are minimal changes to the cross-sectional area, as the polar and equatorial radii expand and contract in sequence. Therefore, oscillations in the droplet are characterized by the difference between the polar radius and equatorial radius, $A = R_L - R_w$. Substituting the definitions for polar and equatorial radii yields:

$$A = \frac{R_0}{(1+\delta)^2} - R_0(1+\delta)$$

A truncated Taylor expansion, $\frac{R_0}{(1+\delta)^2} \approx R_0(1 - 2\delta + 3\delta^2)$, can be employed to simplify the derivation with minimal error:

$$\frac{A}{R_0} = (1 - 2\delta + 3\delta^2 - 1 - \delta) = (3\delta^2 - 3\delta)$$

Using the quadratic formula to solve for δ and taking the smaller root gives:

$$\delta = \frac{1 - \sqrt{1 - 4(\frac{A}{3R_0})}}{2} \qquad \text{Side View Deformation} \qquad (3.6)$$

Taylor approximation simplifies the derivation of δ significantly, warranting its use. The error associated with the Taylor approximation is the sum of the truncated terms. For sample deformation of 0.07—a value at the upper bound

of deformation—the error associated with the Taylor approximation is

$$\text{error} = \frac{1}{(1+\delta)^2} - (1 - 2\delta + 3\delta^2) \qquad \text{Error Definition}$$

$$\text{error} = \frac{1}{(1+0.07)^2} - (1 - 2(0.07) + 3(0.07)^2) \qquad \text{Substitution}$$

$$\text{error} = -0.00126$$

The side view deformation can also be related to the eccentricity of the droplet.

$$e = \sqrt{1 - \left(\frac{R_L}{R_w}\right)^2} \qquad \text{Prolate Eccentricity}$$

$$= \sqrt{1 - \left(\frac{\frac{R_0}{(1+\delta)^2}}{(1+\delta)R_0}\right)^2} = \sqrt{1 - (1+\delta)^{-6}}$$

$$e = \sqrt{1 - \left(\frac{R_w}{R_L}\right)^2} \qquad \text{Oblate Eccentricity}$$

$$= \sqrt{1 - \left(\frac{(1-\delta)R_0}{\frac{R_0}{(1-\delta)^2}}\right)^2} = \sqrt{1 - (1-\delta)^6}$$

These results, while different, yield consistent results. Below is an example calculation at a deformation of 0.04.

$$e = \sqrt{1 - (1+\delta)^{-6}} = \sqrt{1 + (1+0.04)^{-6}} \qquad = 0.466$$

$$e = \sqrt{1 - (1-\delta)^6} = \sqrt{1 - (1-0.04)^6} \qquad = 0.458$$

3.5 Surface Tension Derivation and Deformation Correction

3.5.1 Rayleigh Method

Levenberg-Marquardt curve fitting is used to determine frequency values for each 0.4-second segment of data. These frequency values are associated with the median temperature of the segment and paired together for analysis of surface tension's temperature dependence. Despite gold resisting the formation of oxides, contamination can still affect the surface of the sample. This often comes from the tumbling and sanding process, with common contaminants being silica, alumina, or titania resulting from the abrasives used in these processes. Contaminants cannot be determined until the sample returns from the ISS, however. If the pyrometer is focused on an oxide, the difference in emissivity of the oxide causes the pyrometer to record a temperature higher than that of the droplet. These disturbances, known as oxide spikes, must be avoided in data analysis. This is implemented in code through a threshold variable, T_{crit}:

$$T_{\text{crit}} = \begin{cases} 0.3\,K & \text{Side View} \\ 0.8\,K & \text{Top View} \end{cases}$$

If the difference between any two successive frames exceeds T_{crit}, an oxide spike is present, and data from that segment is discarded. Fits are also discarded if the curve fit has an R^2 value below 0.95. The frequency garnered from the curve fit of each data segment can be applied directly to the Rayleigh equation assuming the droplet is operating in the $\ell = 2$, $m = 0$ mode. This gives a value for surface tension that does not correct for the effect of deformation on oscillation frequency.

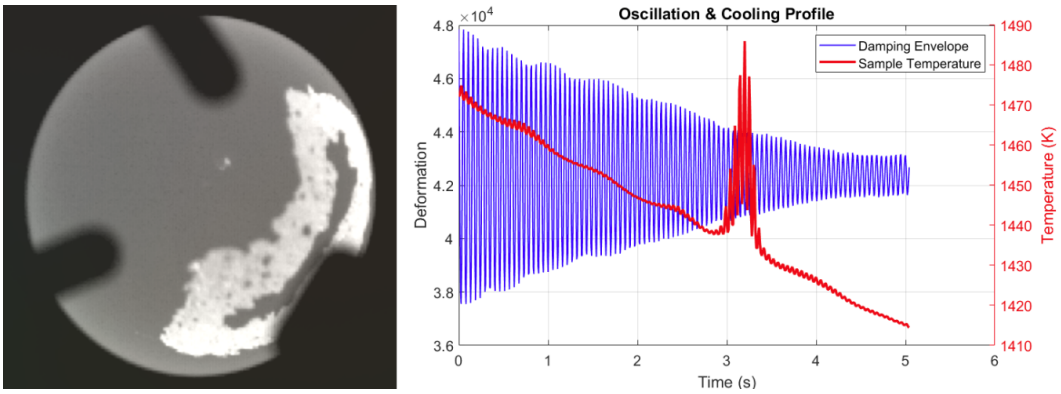

Figure 3.7 : Sample with Oxide Present on Surface (Left) and Associated Oxide Spike (Right)

3.5.2 Deformation Corrected Analysis

Frequency and temperature values from each segment are stored with their corresponding deformation and fitted to the corrected frequency formula with initial guesses and bounds as shown below:

Table 3.3 : Initial Guesses and Lower and Upper Bounds for Frequency Shift Curve Fit

	$\nu_{\theta=0}$	p_θ	p_1	p_2
Initial Guess	$\max(\nu)$	-0.125	-0.08	-2.0
Lower Bound	$0.9\max(\nu)$	-0.25	-0.1	-2.5
Upper Bound	$1.1\max(\nu)$	-0.1	0	-1.5

The initial guesses are derived from a study on LEK-94 and provide effective preliminary values for the iterative algorithm [34]. The value for the p_1 term in particular is constrained to serve as a correction factor for the frequency shift. If the value of the p_1 is left unconstrained, a direct relationship between oscillation frequency and temperature is observed, which violates Eötvös Rule.

With correction factors determined, the Corrected Rayleigh Equation can be

applied to give frequency-corrected values of surface tension.

3.6 Quantifying Fluid Velocity

The eddies created by the heater and positioner respectively counteract each other's motion [13]. Baker and Nawer found that the components of velocity from both the positioner and heater voltage are turbulent when testing gold, even for the smallest voltages. Therefore, the turbulent coefficients for both the positioner and heater surrogate model are used [12]. This allows for a final surrogate model to quantify the maximum fluid velocity within the sample by subtracting the positioner velocity from the heater velocity at given heater and positioner values. As to not convolute the study, the positioner voltage remains constant across all runs at 4.0 V.

$$u_{\max}, \dot{\gamma}_{\max} = \sum_{i,j,k,s} q_{\text{ijks}} \cdot \left(U^H_{\text{ctr}}\right)^i \cdot \rho^j (\ln \mu)^k \cdot (\ln \sigma_{\text{el}})^s \tag{3.7}$$
$$- \sum_{i,j,k,s} p_{\text{ijks}} \cdot \left(U^P_{\text{ctr}}\right)^i \cdot \left(\tfrac{1}{\sqrt{\sigma_{\text{el}}}}\right)^j \cdot \left(\rho^k\right) \cdot \left(\tfrac{1}{\ln(\mu)}\right)^s \quad \text{Droplet Velocity}$$

Velocities were calculated iteratively over a range of temperature values spanning from 1330 to 1440 K with a step size of one degree kelvin. This range spans both the melting temperature of gold and the entire range of data collection. For each iteration, the temperature was used to define gold's material properties, which were then applied to equation 3.7 along with the respective heater and positioner control voltages.

These voltages are then used to calculate Reynolds numbers using equation 2.16. The spherical diameter of the sample used in Reynolds number calculation is found by obtaining the volume of the droplet from the mass and iterated

density value, then solving for the diameter. From this, a Reynolds number for each temperature is calculated to quantify the level of stirring within the sample. The laminar-turbulent transition boundaries used here are specific to electromagnetically levitated droplets in microgravity, and differ significantly from classical pipe flow criteria. The transition was experimentally identified by Hyers *et al.* through direct observation of the formation and perturbation of the stagnation line at the equator of the droplet during microgravity experiments, with laminar flow below $Re = 500$, a transitional regime between $500 < Re < 600$, and fully turbulent flow above $Re = 600$ [40, 44].

Table 3.4 : Flow Regimes Within a Metallic Droplet Defined by Reynolds Number

Flow Regime	Re
Laminar	< 500
Transitional	$500 - 600$
Turbulent	> 600

Chapter 4

Results

4.1 Pyrometry

A time-temperature profile was recorded for each sample. A summary of pyrometry results and a representative time-temperature profile are shown below, with full time-temperature profiles located in Appendix C.

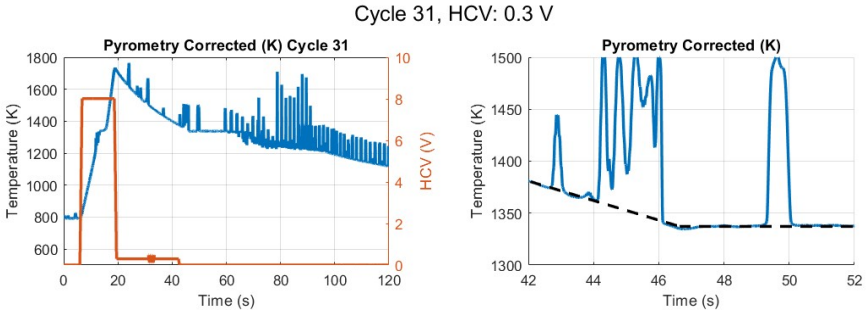

Figure 4.1 : Corrected Time-Temperature Profile of Cycle 31 (Left), with Melt Plateau (Right). Filtered Signal Given by Dashed Black Line (Right)

Data collection starts while the sample is still in a solid state, denoted by the initial plateau at roughly 800 K on the time-temperature profile. This is followed by the melting and solidification of the sample. After a prearranged heating time, or once a prearranged temperature has been reached, the heater is reduced to its testing value, and cooling ensues. As seen in Figure 4.1, cooling corresponds to the reduction of U^H_{ctr}. Additionally, Figure 4.1 showcases the Faraday excitation and intermediate U^H_{ctr} value of 0.3 V. Just after 40 seconds, the heater is turned off entirely, and the sample enters the melt plateau. After this point, no data that is recorded is used in analysis, with

the last necessary data being the recording of the solidification temperature for pyrometry correction. Figure 4.1 also contains a concise view of the time-temperature profile at the end of cooling and the beginning of the melt plateau with considerable oxide spikes. A summary highlighting the apparent solidification temperature, T_{PL}, is given by Table 4.1. Solidification temperature was determined by taking the average of a representatively large portion of the melt plateau. Special consideration was taken when sampling the melt plateau to avoid oxide spikes. As such, there is no characteristic time or time frame in which these samples were taken.

Table 4.1 : Cycle number, associated HCV value, and observed liquidus temperature.

Cycle	T_{PL} **(K)**	**HCV**
31	1293.8 ± 0.2638	0.3
32	1293.9 ± 0.2121	0.3
33	1293.8 ± 0.1724	0.3
34	1293.9 ± 0.1535	0.3
36	1293.8 ± 0.2195	0.5
38	1294.0 ± 0.2497	0.6
39	1293.9 ± 0.2596	0.8
40	1294.3 ± 0.1988	1.0

4.2 Frequency Analysis

Uncorrected surface tension results show an increased dependence on temperature as HCV increases. Shown in Figure 4.2 is all frequency data for the trials run at an HCV of 0.3 volts. Frequency values were taken from the nonlinear regression and applied directly to the uncorrected Rayleigh equation. For plots of all heater control voltages, see Appendix D.

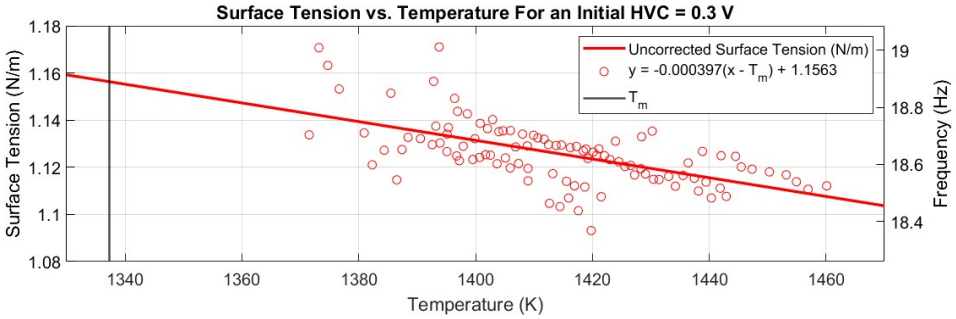

Figure 4.2 : Surface Tension (N/m, Left Axis) and Frequency (Hz, Right Axis) vs. Temperature Profile for all $U^H_{\text{ctr}} = 0.3$ Runs

Linear fits were applied to the uncorrected surface tension results, with uncertainty in fitted parameters calculated through the standard processes outlined by the Guide to the Expression of Uncertainty in Measurement (GUM) [45, 46]. Further details on the calculation of linear fit uncertainties can be found in Chapter 6.6 *Uncertainty in Linear Regression.* Results of the fit can be found in Table 4.2.

Table 4.2 : Results of Linear Fit of Uncorrected Surface Tension Data $y = m(T - T_m) + b$

$U^H_{\mathbf{ctr}}$	**m (N/mK)**	**b (N/m)**
0.3	-0.000350 ± 0.000040	1.151931 ± 0.002958
0.5	-0.000330 ± 0.000132	1.140640 ± 0.007317
0.6	-0.000697 ± 0.000076	1.167946 ± 0.004781
0.8	-0.000776 ± 0.000092	1.185598 ± 0.007364
1.0	-0.000945 ± 0.000043	1.207573 ± 0.003986

The following tables include all data analyzed in this work. The values for frequency reported are without deformation correction. The values for temperature are corrected for emissivity shift.

Table 4.3 : Frequency and Deformation Data — 0.3 V

Cycle	View	Corrected Temp (K)	Frequency (Hz)	Deformation
31	Top	1460.0980	18.529038	0.048276
31	Top	1456.9232	18.516935	0.045049
31	Top	1454.9270	18.543518	0.042733
31	Top	1453.1762	18.567913	0.039632
31	Top	1450.3038	18.578096	0.037609
31	Top	1447.3327	18.587800	0.035660
31	Top	1445.4856	18.595584	0.033766
31	Top	1444.5066	18.632950	0.030911
31	Top	1442.0228	18.635211	0.027955
31	Top	1438.8533	18.650328	0.025606
31	Top	1430.2388	18.721362	0.017283
31	Top	1428.4185	18.701777	0.015112
31	Top	1426.5564	18.820587	0.012737
31	Top	1423.9566	18.686250	0.011436
31	Top	1421.1075	18.659235	0.010086
31	Top	1418.9059	18.658575	0.009532
32	Top	1441.8760	18.520741	0.055848
32	Top	1439.4509	18.542260	0.053575
32	Top	1437.4490	18.555735	0.051566
32	Top	1435.5178	18.565543	0.048265
32	Top	1433.0567	18.562227	0.044706
32	Top	1430.4680	18.552194	0.041118
32	Top	1428.3227	18.589324	0.038179
32	Top	1426.5672	18.600652	0.035861
32	Top	1424.5181	18.613831	0.034152
32	Top	1422.0709	18.635411	0.032948
32	Top	1420.1374	18.648162	0.031830
32	Top	1418.4342	18.652221	0.030770
32	Top	1416.2068	18.663694	0.029751
32	Top	1413.7973	18.671304	0.029039
32	Top	1411.7496	18.693120	0.028394

Table 4.3 – continued from previous page

Cycle	View	Corrected Temp (K)	Frequency (Hz)	Deformation
32	Top	1409.9285	18.707135	0.027534
32	Top	1408.0364	18.711017	0.025940
32	Top	1405.9506	18.723287	0.025084
32	Top	1403.9750	18.719502	0.023070
32	Top	1402.0513	18.730189	0.020737
32	Top	1399.8870	18.694884	0.018119
32	Top	1397.8954	18.668532	0.015040
32	Top	1396.7631	18.634440	0.012336
32	Top	1395.3457	18.733578	0.010077
32	Top	1392.5869	18.674041	0.008963
32	Side	1442.9158	18.491598	0.059073
32	Side	1440.3598	18.486003	0.055751
32	Side	1438.1610	18.510792	0.050360
32	Side	1436.3874	18.609845	0.045881
32	Side	1434.2070	18.527631	0.042056
32	Side	1431.4230	18.551042	0.039370
32	Side	1429.0868	18.571153	0.036571
32	Side	1427.2173	18.567630	0.034178
32	Side	1425.5746	18.597284	0.032150
32	Side	1422.9827	18.621738	0.029793
32	Side	1420.7381	18.636588	0.027748
32	Side	1419.2331	18.625290	0.026742
32	Side	1417.2679	18.667760	0.025826
32	Side	1414.7032	18.672603	0.023863
32	Side	1412.4750	18.674186	0.022479
32	Side	1410.6583	18.697734	0.020673
32	Side	1408.8537	18.669440	0.019194
32	Side	1406.8407	18.665922	0.017116
32	Side	1404.6920	18.722533	0.015278
32	Side	1402.9105	18.761562	0.013272
32	Side	1400.7944	18.748419	0.011956
32	Side	1398.5844	18.781555	0.010216

Table 4.3 – continued from previous page

Cycle	View	Corrected Temp (K)	Frequency (Hz)	Deformation
32	Side	1396.9179	18.790330	0.008301
32	Side	1396.4128	18.835532	0.006549
32	Side	1393.7590	19.013286	0.004749
33	Top	1418.7000	18.525038	0.067929
33	Top	1416.9376	18.529230	0.062832
33	Top	1415.5593	18.544883	0.059427
33	Top	1413.2165	18.571905	0.054415
33	Top	1408.9765	18.590194	0.046311
33	Top	1407.3567	18.607622	0.043145
33	Top	1405.0983	18.627086	0.039456
33	Top	1402.5376	18.637039	0.036781
33	Top	1395.1299	18.711185	0.025610
33	Top	1393.1933	18.738792	0.022985
33	Top	1385.5009	18.853505	0.012714
33	Top	1376.6488	18.868065	0.008142
33	Top	1374.7008	18.949651	0.006364
33	Top	1373.1873	19.010735	0.004994
33	Top	1371.5097	18.708366	0.004052
33	Side	1419.7885	18.370378	0.082246
33	Side	1417.5952	18.441005	0.076257
33	Side	1415.9248	18.485722	0.067637
33	Side	1414.4466	18.455455	0.060661
33	Side	1412.6572	18.467052	0.055043
33	Side	1408.9870	18.546646	0.048326
33	Side	1405.9292	18.592129	0.045425
33	Side	1403.6790	18.606822	0.042432
33	Side	1401.7200	18.638255	0.041183
33	Side	1400.6947	18.629156	0.037927
33	Side	1399.5335	18.622060	0.033277
33	Side	1397.2221	18.617645	0.030657
33	Side	1395.0993	18.649487	0.028157
33	Side	1393.9146	18.679629	0.027121

Table 4.3 – continued from previous page

Cycle	View	Corrected Temp (K)	Frequency (Hz)	Deformation
33	Side	1392.8325	18.894654	0.024644
33	Side	1390.5588	18.695143	0.023282
33	Side	1388.4378	18.699530	0.019011
33	Side	1387.4013	18.656889	0.015678
33	Side	1386.5054	18.550122	0.013514
33	Side	1384.3491	18.654220	0.011029
33	Side	1382.3086	18.603176	0.009257
33	Side	1380.9317	18.715074	0.007051
34	Top	1388.0994	18.626371	0.047200
34	Top	1386.1180	18.615137	0.042697
34	Top	1384.0930	18.631884	0.037609
34	Top	1382.1295	18.671492	0.033500
34	Top	1380.3232	18.698527	0.031186
34	Top	1378.6786	18.730557	0.028786
34	Top	1377.0806	18.757990	0.025400
34	Top	1375.2792	18.788411	0.021265
34	Top	1373.5915	18.846440	0.018016
34	Side	1387.7826	18.611296	0.058875
34	Side	1385.8597	18.614050	0.055693
34	Side	1383.8774	18.630943	0.052031
34	Side	1381.8846	18.659077	0.049830
34	Side	1380.0665	18.669241	0.047314
34	Side	1378.4921	18.674591	0.044301
34	Side	1375.0322	18.717568	0.036480
34	Side	1373.3701	18.744298	0.034103
34	Side	1371.8152	18.751684	0.030804
34	Side	1370.1593	18.764798	0.027753
34	Side	1368.6416	18.779542	0.024642
34	Side	1366.7604	18.787977	0.021304
34	Side	1364.9538	18.811807	0.018346
34	Side	1363.6126	18.848343	0.015648

Table 4.4 : Frequency and Deformation Data — 0.5 V

Cycle	View	Corrected Temp (K)	Frequency (Hz)	Deformation
36	Top	1403.5575	18.570419	0.058993
36	Top	1401.7505	18.596238	0.053515
36	Top	1398.6358	18.605337	0.042595
36	Top	1396.3842	18.614791	0.036872
36	Top	1392.8355	18.639453	0.028092
36	Top	1391.2701	18.652965	0.025191
36	Top	1389.2754	18.630138	0.021875
36	Top	1387.3566	18.645792	0.018057
36	Top	1385.7255	18.624442	0.014015
36	Top	1384.2297	18.637097	0.010800
36	Top	1382.5549	18.561271	0.008629
36	Top	1380.7141	18.672564	0.007415

Table 4.5 : Frequency and Deformation Data — 0.6 V

Cycle	View	Corrected Temp (K)	Frequency (Hz)	Deformation
38	Top	1416.7600	18.451272	0.073657
38	Top	1415.1857	18.556040	0.026589
38	Top	1413.5519	18.473242	0.058510
38	Top	1411.6463	18.503981	0.053161
38	Top	1409.8112	18.543426	0.050168
38	Top	1408.4819	18.561370	0.048149
38	Top	1406.9530	18.584112	0.046822
38	Top	1404.8041	18.615142	0.044785
38	Top	1402.6995	18.651401	0.017007
38	Top	1401.2074	18.636061	0.040568
38	Top	1400.1141	18.625032	0.036345
38	Top	1398.3778	18.638640	0.032721
38	Top	1396.1607	18.649901	0.029539
38	Top	1394.5070	18.658002	0.027779
38	Top	1393.3736	18.681991	0.026980
38	Top	1391.6956	18.697361	0.024999

Table 4.5 – continued from previous page

Cycle	View	Corrected Temp (K)	Frequency (Hz)	Deformation
38	Top	1389.4983	18.685907	0.022327
38	Top	1387.9196	18.649842	0.017767
38	Top	1386.9533	18.627375	0.015461
38	Top	1385.4272	18.633905	0.012564
38	Top	1383.3289	18.655396	0.011184
38	Top	1381.6202	18.638124	0.008658
38	Top	1380.5988	18.608168	0.007100
38	Side	1418.7089	18.505306	0.060050
38	Side	1416.7799	18.532624	0.056691
38	Side	1415.2014	18.560105	0.055086
38	Side	1413.5667	18.567951	0.052077
38	Side	1411.6687	18.586313	0.048117
38	Side	1409.8334	18.599387	0.046002
38	Side	1408.4909	18.613646	0.044055
38	Side	1406.9664	18.625343	0.042722
38	Side	1404.8317	18.640187	0.041407
38	Side	1402.7226	18.660705	0.040701
38	Side	1401.2176	18.667123	0.040204
38	Side	1400.1255	18.676186	0.039223
38	Side	1398.4015	18.693100	0.037822
38	Side	1396.1808	18.704423	0.036551
38	Side	1394.5181	18.702118	0.034574
38	Side	1393.3892	18.711692	0.032063
38	Side	1391.7204	18.717851	0.029290
38	Side	1389.5172	18.716342	0.025964
38	Side	1387.9284	18.731621	0.022394
38	Side	1386.9671	18.777388	0.019305
38	Side	1385.4476	18.794144	0.016029
38	Side	1383.3445	18.736228	0.013236
38	Side	1381.6310	18.727428	0.010128
38	Side	1380.6119	18.775436	0.007312

Table 4.6 : Frequency and Deformation Data — 0.8 V

Cycle	View	Corrected Temp (K)	Frequency (Hz)	Deformation
39	Top	1433.8561	18.602731	0.058565
39	Top	1431.8657	18.591936	0.056581
39	Top	1429.9923	18.556356	0.051149
39	Top	1428.7455	18.575451	0.047616
39	Top	1427.5084	18.616019	0.042028
39	Top	1425.4768	18.428209	0.011856
39	Top	1423.4872	18.599713	0.037432
39	Top	1422.1716	18.612549	0.035858
39	Top	1420.9647	18.633114	0.034145
39	Top	1419.1043	18.814813	0.013791
39	Top	1417.1284	18.670449	0.031640
39	Top	1415.7918	18.668316	0.030691
39	Top	1414.6615	18.698546	0.029676
39	Top	1412.9042	18.688389	0.028680
39	Top	1411.0040	18.700062	0.026845
39	Top	1409.6082	18.704110	0.024785
39	Top	1408.4484	18.698153	0.022133
39	Top	1406.9146	18.649465	0.019565
39	Top	1405.1007	18.661610	0.017619
39	Top	1403.6421	18.662568	0.015503
39	Top	1402.4863	18.696273	0.013671
39	Top	1401.0113	18.691553	0.012684
39	Top	1399.3385	18.740324	0.012464
39	Side	1432.4792	18.448129	0.067363
39	Side	1430.4710	18.482378	0.065529
39	Side	1429.0677	18.501231	0.064204
39	Side	1427.9644	18.548676	0.062985
39	Side	1426.1036	18.568430	0.059480
39	Side	1423.9940	18.549609	0.053995
39	Side	1422.5220	18.529020	0.050958
39	Side	1421.3795	18.571238	0.048400

Table 4.6 – continued from previous page

Cycle	View	Corrected Temp (K)	Frequency (Hz)	Deformation
39	Side	1419.6877	18.608744	0.044971
39	Side	1417.6600	18.610802	0.042452
39	Side	1416.1375	18.626504	0.040809
39	Side	1415.0275	18.645588	0.038752
39	Side	1413.4643	18.655396	0.037076
39	Side	1411.5344	18.660786	0.035891
39	Side	1409.9808	18.686826	0.034073
39	Side	1408.8028	18.672586	0.032901
39	Side	1407.4063	18.673830	0.031459
39	Side	1405.6305	18.700820	0.029392
39	Side	1404.0137	18.706824	0.027002
39	Side	1402.8401	18.720829	0.024821
39	Side	1401.4842	18.720048	0.021436
39	Side	1399.8175	18.705974	0.018444

Table 4.7 : Frequency and Deformation Data — 1.0 V

Cycle	View	Corrected Temp (K)	Frequency (Hz)	Deformation
40	Top	1449.2951	18.412114	0.088257
40	Top	1447.3542	18.423368	0.084273
40	Top	1445.7421	18.440103	0.079413
40	Top	1444.6604	18.458226	0.077024
40	Top	1443.3018	18.485887	0.075111
40	Top	1441.4429	18.520718	0.072636
40	Top	1439.8450	18.545569	0.070472
40	Top	1438.8111	18.553247	0.068261
40	Top	1437.5547	18.559285	0.065845
40	Top	1435.7619	18.574737	0.062711
40	Top	1434.1762	18.599798	0.059670
40	Top	1433.0640	18.602924	0.056492
40	Top	1431.8375	18.605048	0.053163
40	Top	1430.1944	18.610956	0.050305

Table 4.7 – continued from previous page

Cycle	View	Corrected Temp (K)	Frequency (Hz)	Deformation
40	Top	1428.6525	18.618737	0.047459
40	Top	1427.5295	18.623704	0.043677
40	Top	1426.3585	18.630438	0.041115
40	Top	1424.8290	18.684071	0.038429
40	Top	1423.3477	18.667702	0.036813
40	Top	1422.2156	18.668799	0.034659
40	Top	1421.0415	18.679534	0.033512
40	Top	1419.5693	18.703250	0.032428
40	Top	1418.1703	18.705015	0.031001
40	Top	1417.0485	18.694190	0.029384
40	Top	1415.8805	18.684821	0.027407
40	Top	1414.5096	18.702513	0.025894
40	Top	1413.1641	18.710488	0.024066
40	Top	1412.0010	18.715638	0.023176
40	Side	1448.6381	18.383543	0.073605
40	Side	1444.2683	18.462032	0.070300
40	Side	1442.6989	18.464076	0.067463
40	Side	1439.4362	18.512905	0.058386
40	Side	1438.4553	18.531185	0.054947
40	Side	1437.0006	18.537456	0.053804
40	Side	1435.1437	18.555324	0.053123
40	Side	1433.7304	18.584693	0.052295
40	Side	1432.7104	18.608690	0.050879
40	Side	1429.5945	18.634057	0.047911
40	Side	1428.2216	18.622791	0.043801
40	Side	1424.2684	18.613101	0.031622
40	Side	1422.9209	18.641509	0.030679
40	Side	1420.5626	18.689805	0.029704
40	Side	1419.0440	18.712592	0.029463
40	Side	1417.7542	18.720094	0.028686
40	Side	1415.4347	18.715712	0.025062
40	Side	1414.0287	18.682361	0.023759

Table 4.7 – continued from previous page

Cycle	View	Corrected Temp (K)	Frequency (Hz)	Deformation
40	Side	1412.7578	18.676213	0.021096
40	Side	1410.3648	18.692998	0.019220
40	Side	1409.0935	18.684803	0.019050

Chapter 5

Discussion

5.1 Validation of Excitation Parameters

Separate runs were conducted to validate the Faraday excitation parameters, independent of the primary experimental runs. Three types of validation runs were performed: an *a-sweep*, in which the Faraday forcing amplitude is varied over a range of values; a *t-sweep*, in which the forcing duration is varied; and an *f-sweep*, in which the forcing frequency is varied. Table 5.1 summarizes these experimental runs.

Table 5.1 : Experimental Test Matrix

Test Type	**Number of Runs**	**Run Number(s)**
a-sweep	1	51
t-sweep	1	53
f-sweep	4	56, 57, 60, 61

5.1.1 Validation of Faraday Amplitude

In the a-sweep, the Faraday excitation frequency was held at 18.5 Hz for 2.0 seconds. The positioner voltage was fixed at 5 V and the heater control voltage at a median value of 1.6 V. To isolate the effect of amplitude from temperature, the apparent temperature was held constant at 1100°C.

Oscillation performance is evaluated using the deformation of the droplet as

observed from the side view.

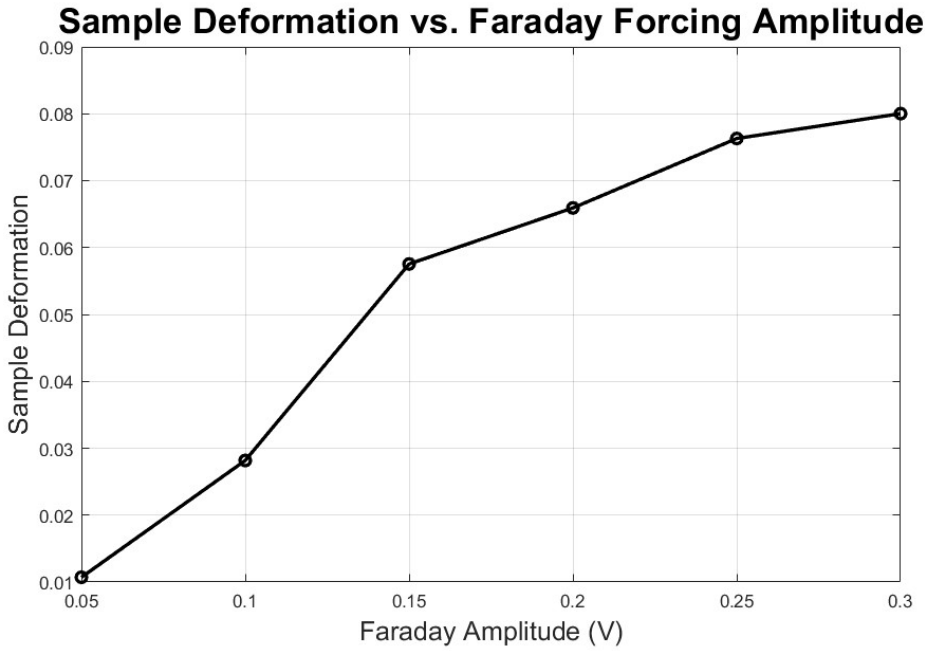

Figure 5.1 : Droplet oscillation amplitude (pixels^2) vs. Faraday forcing amplitude (V).

As shown in Figure 5.1, the relationship between oscillation amplitude and forcing amplitude becomes nonlinear beyond 0.15 V. This indicates that energy intended to excite the $\ell = 2$ mode is also driving off-axis oscillations with nonzero m. Tests, however, were run at an amplitude of 0.2 V. This feeds minimally to off-mode oscillations and was instilled to receive more dramatic deformations to better define deformation correction analysis.

5.1.2 Validation of Stimulation Time

The t-sweep varied the Faraday excitation duration from one to five seconds in one-second increments. To isolate the effect of excitation time, all other parameters were held constant: excitation frequency at 18.5 Hz, heater control voltage at 1.6 ± 0.2 V, positioner voltage at 5 V, and apparent temperature

at 1100 K. Figure 5.2 shows the full oscillation profile across all tests, and Figure 5.3 shows the maximum amplitude achieved in each.

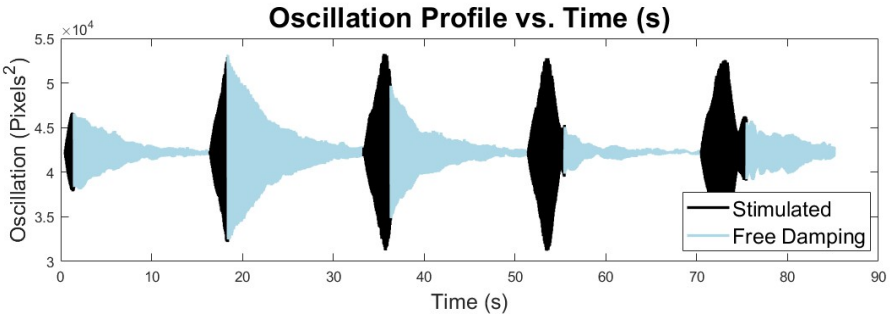

Figure 5.2 : Oscillation profile (pixels^2) vs. time (s), with active Faraday forcing shown in black and free damping in blue.

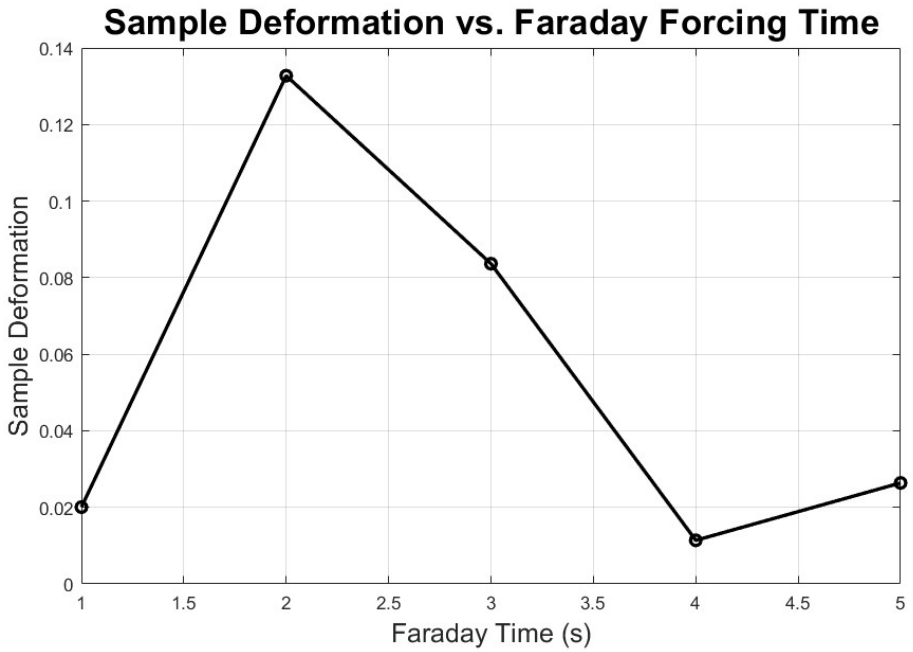

Figure 5.3 : Oblate Eccentricity at the End of Excitation amplitude vs. Faraday Excitation Duration (s).

As seen in Figure 5.2, samples excited for substantially longer than two seconds begin to oscillate with diminished deformation during forcing. This is attributed to the onset of mixed-mode oscillations at longer excitation times.

While the maximum oscillation amplitude is consistent across all tests with a stimulation time greater than one second, the time at which this maximum occurs falls consistently between 2.0 and 2.3 seconds after the start of excitation. Accordingly, an excitation duration of 2.1 seconds was adopted for all subsequent tests.

5.1.3 Validation of Faraday Frequency

The optimal excitation frequency was identified by sweeping over a range of forcing frequencies and measuring the post-stimulation oscillation amplitude. As the forced frequency approaches the natural frequency, the sample resonates more strongly; the natural frequency therefore corresponds to the peak in response amplitude.

Four f-sweeps were conducted, each with slightly different experimental parameters, as summarized in Table 5.2.

Table 5.2 : Experimental input parameters for the four f-sweep runs.

Cycle	Range (Hz)	U^H_{ctr} (V)	U^P_{ctr} (V)	$T_{P,\text{hold}}$ (°C)	Time (s)	$\Delta\nu$ (Hz)
56	18.4–18.8	1.6 ± 0.2	5	1100	2	0.1
57	18.4–18.8	1.7 ± 0.2	5	1140	2	0.1
60	18.4–18.8	2.0 ± 0.2	5	1220	2	0.1
61	18.2–18.6	1.8 ± 0.2	5	1180	2	0.1

Despite small differences in experimental parameters across the four runs, the peak response amplitude falls consistently between 18.4 and 18.6 Hz. Results from Cycle 56, which exhibits a pronounced amplitude peak at 18.6 Hz, were used to validate the excitation frequency. Cycle 56 was conducted at an apparent temperature of 1100 C, for which a large number of data points

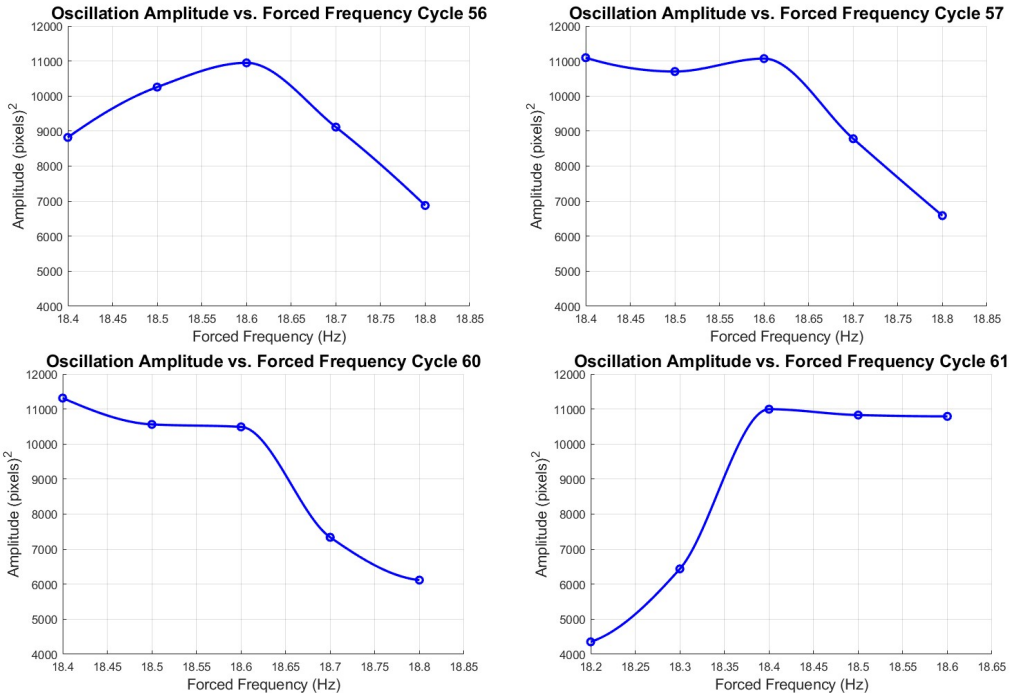

Figure 5.4 : Amplitude (pixels^2) vs. forced frequency (Hz) for Cycles 56, 57, 60, and 61, respectively.

were available. Accordingly, 18.6 Hz was selected as the Faraday excitation frequency for all subsequent tests.

5.2 Effect of Deformation on Surface Tension

Due to the lack of data for $U^H_{\text{ctr}} = 0.5$, it was determined that the data would not be used in subsequent analysis. In particular, a reliable relationship between frequency, temperature, and deformation, as characterized by the corrected frequency formula, could not be determined. This is exhibited in the frequency shift ratio plot in Appendix E and the values of the subsequent relationship between corrected surface tension and temperature, which violates Eötvös's Rule, as seen in Appendix F.

Deformation and heater control voltage are directly related. This is seen vi-

sually in Figure 5.5, in which the maximum eccentricity is related to heater control voltage. For the time segment corresponding to the largest deformation, immediately after excitation, the average of the eccentricity peaks was taken, with error bars corresponding to the standard deviation of the peaks.

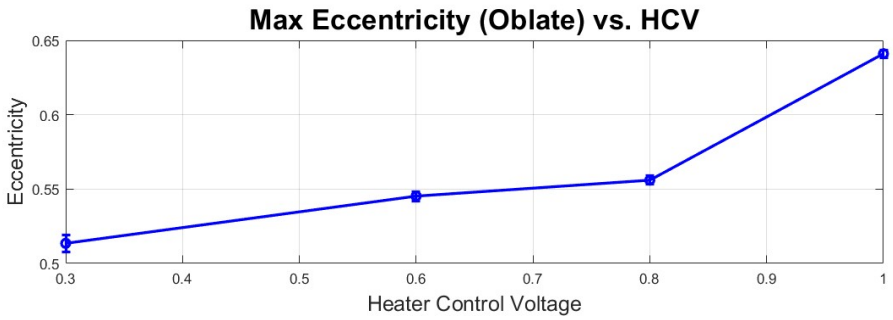

Figure 5.5 : Max Eccentricity vs. Heater Control Voltage

Additionally, a quantification of steady-state deformation was explored, relating to the amount of deformation present as a result of solely the flat heater control voltage without oscillations. The beginning of each experimental run consists of a steady heater control voltage at the median value. Deformation was taken with respect to this portion of the run. It can be seen in Figure 5.6 that an exponential behavior is exhibited between steady-state deformation and heater control voltage. At the lower heater control voltages, particularly the 0.3 V, the signal is predominantly noise, contributing to a high noise-to-signal ratio, as evidenced by the error bars.

5.2.1 Correction Factors

The oscillation frequencies associated with each heater control voltage were fit to the corrected frequency formula to determine the correction coefficients p_1 and p_2. The resulting coefficients, along with other relevant parameters, are

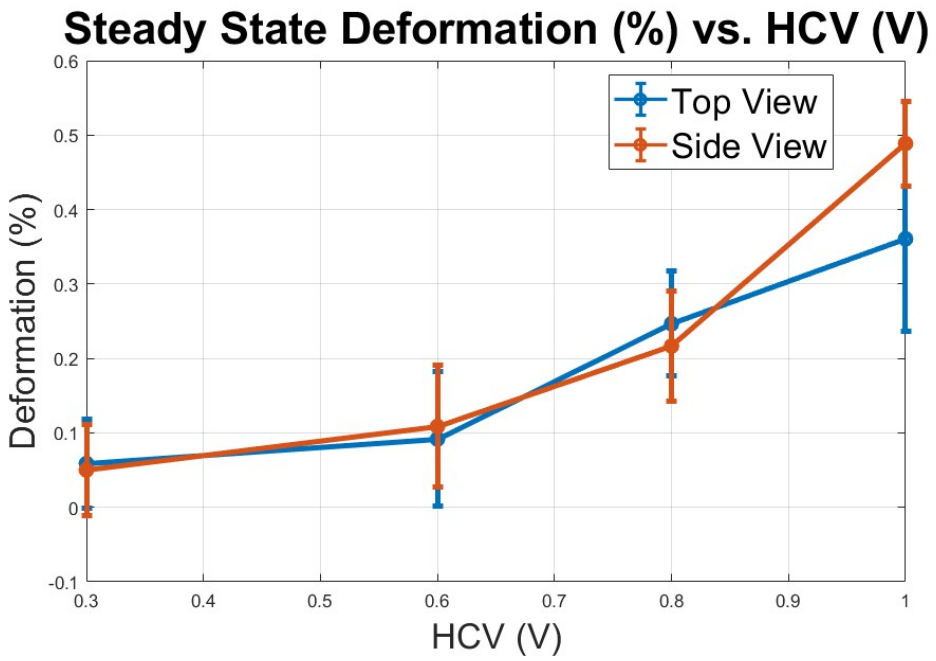

Figure 5.6 : Steady State Deformation (%) vs. Heater Control Voltage for Both Top View (Blue) and Side View (Orange) Runs

presented in Table 5.3. A representative visualization of the curve fit is shown in Figure 5.7; fits for the remaining heater control voltages are provided in Appendix E.

Table 5.3 : Rayleigh equation correction factors for all heater control voltage runs.

U^H_{ctr} (V)	$\nu_{\theta=0}$ (Hz)	p_θ	p_1	p_2	R^2
0.3	18.860	−0.139	−0.000	−2.713	0.695
0.6	18.821	−0.167	−0.000	−1.725	0.731
0.8	18.882	−0.177	−0.000	−1.778	0.845
1.0	18.903	−0.169	−0.000	−1.500	0.841

One immediate result that is seen visually from Figure 5.7 is that excitation frequency does not substantially affect initial frequency measurements. Frequencies associated with high deformation and dimensionless temperature

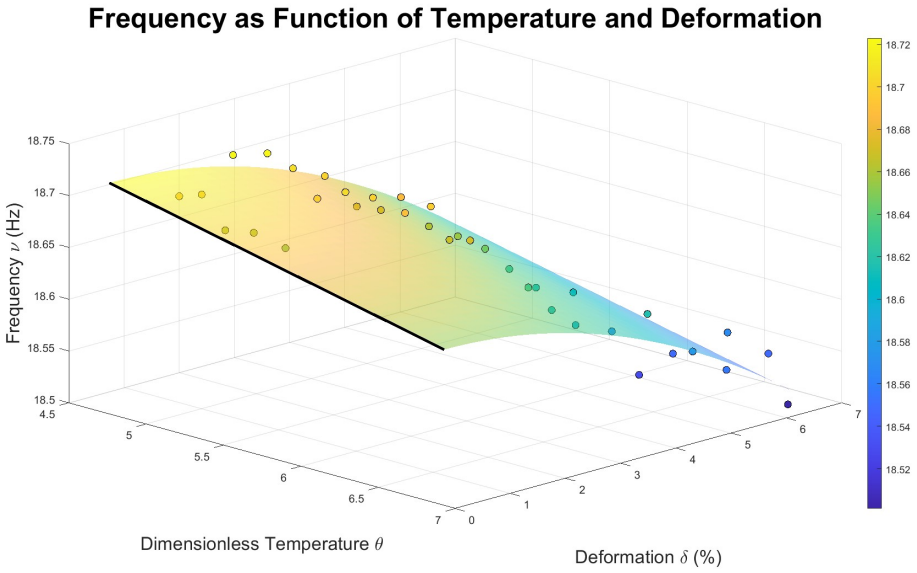

Figure 5.7 : Nonlinear regression of the frequency correction formula $\nu_c = \nu_{\theta=0}(1 + p_\theta\theta)(1 + p_1\delta + p_2\delta^2)$ for $U^H_{\text{ctr}} = 0.8$ V.

correspond to measurements taken immediately after the conclusion of excitation. It can be seen that these measurements are substantially below the excitation frequency of 18.6 Hz. However, the first recorded frequency after excitation nears that of the excitation frequency as heater control voltage increases. Quantification of the results is seen in Table 5.4.

Table 5.4 : Average of First Three Frequencies After Excitation for Each Heater Control Voltage

U^H_{ctr}	Lowest 3 Frequencies (Averaged)
0.3	18.42 Hz
0.6	18.45 Hz
0.8	18.53 Hz
1.0	18.53 Hz

Upper and lower bounds were imposed on the curve-fit parameters to ensure consistency with prior results using the corrected frequency method [34]. Several bounds were motivated directly by physics. The correction factor p_θ was

constrained to be strictly negative, reflecting the well-established inverse relationship between temperature and oscillation frequency, and was bounded within the range reported for gold in prior ground-based studies [6, 4]. The same physical reasoning was applied to the linear deformation correction factor p_1, since large positive values would imply an unphysical direct relationship between surface tension and frequency.

These parameter constraints introduce modest trade-offs, most visibly in the values of p_2. Following Xiao et al. [34], who identified a quadratic relationship between frequency and deformation, this study adopted the same functional form and applied bounds on the quadratic coefficient that reflect their results. For heater control voltage of 1.0 V, the fitted value of p_2 falls directly on the lower bound, suggesting that the fit may be slightly over-constrained in these cases. Relaxing the bounds, however, led to significant overfitting to noise, with negligible improvement in R^2 (0.853 for 1.0 V). The original bounds were therefore retained.

5.2.2 Corrected Surface Tension

While the temperature dependence of oscillation frequency is well characterized in the literature, its dependence on droplet deformation is not. To isolate and visualize the deformation dependence, the temperature correction term p_θ is removed, and the resulting frequency shift ratio is plotted as a function of deformation for several temperature ranges. These results are shown in Figure 5.8.

With p_1 and p_2 determined, corrected surface tension values are obtained by applying the corrected Rayleigh equation to the full dataset. Linear fits are

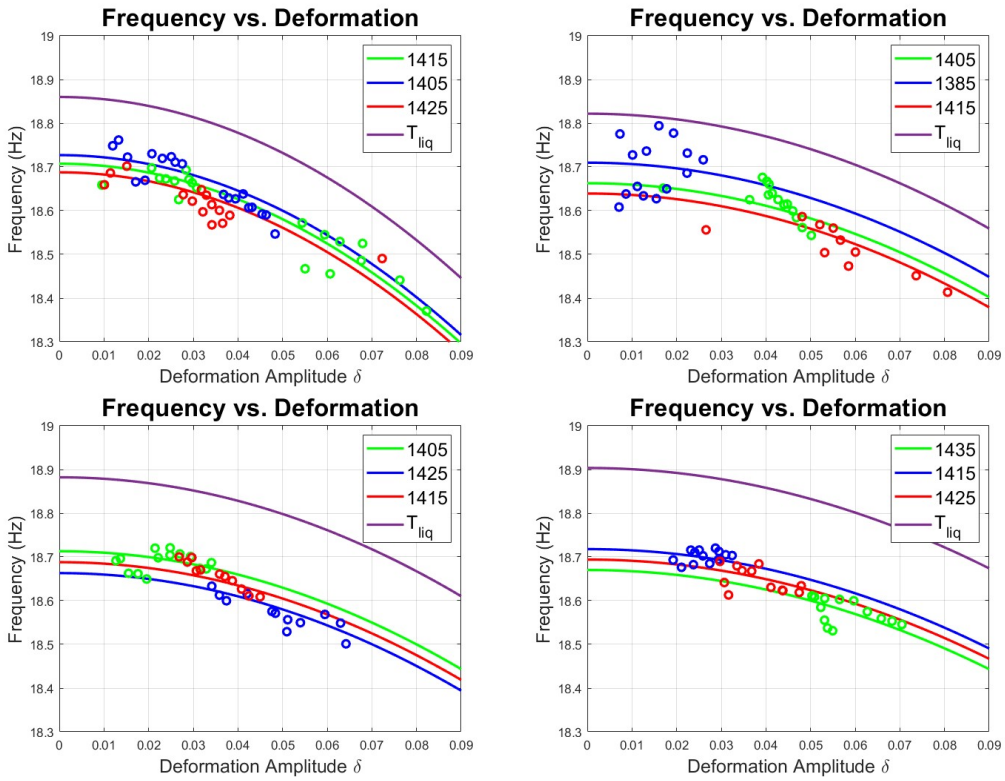

Figure 5.8 : Frequency (Hz) vs. deformation for heater control voltages of 0.3, 0.6, 0.8, and 1.0 V, respectively.

then applied to each corrected dataset; the results are summarized in Table 5.5 and visualized in Figure 5.9. The results show that higher heater control voltages are associated with both a stronger temperature dependence of surface tension and a higher surface tension value at the melting temperature.

Table 5.5 : Results of linear fits to corrected surface tension data, $\sigma = m(T - T_m) + b$.

U^H_{ctr} (V)	m (N/m·K)	b (N/m)
0.3	-0.000239 ± 0.000028	1.152191 ± 0.002084
0.6	-0.000312 ± 0.000068	1.149960 ± 0.004289
0.8	-0.000356 ± 0.000086	1.158783 ± 0.006824
1.0	-0.000371 ± 0.000041	1.163987 ± 0.003758

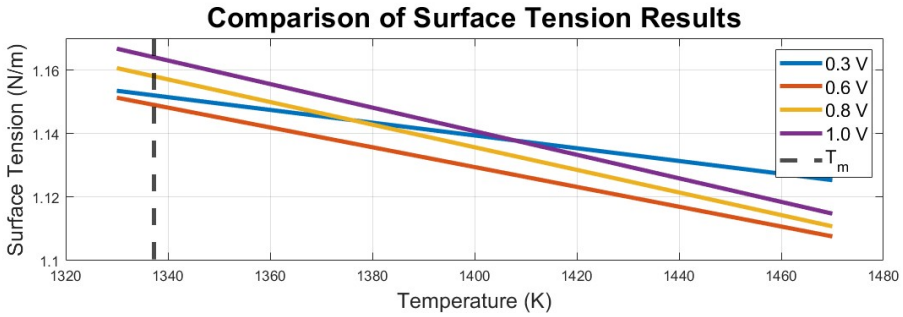

Figure 5.9 : Comparison of corrected surface tension curve fits across all heater control voltage runs.

5.3 Effect of Stirring on Surface Tension

5.3.1 Quantification of Stirring

The computed flow velocities and corresponding Reynolds numbers are presented in Figure 5.10. At heater control voltages of 0.3 and 0.6 V, the flow remains within the laminar regime ($Re < 500$) across all temperatures tested, with the 0.6 V case approaching the transitional boundary. At 0.8 V, the flow sits firmly in the transitional regime throughout the tested temperature range, only reaching the turbulent threshold at approximately 1440 K—a temperature not included in the test matrix for that voltage. At 1.0 V, the flow is fully turbulent across all temperatures tested.

During Faraday excitation, the heater voltage oscillates above and below its mean value, meaning the internal flow regime can fluctuate on short timescales. For a mean heater control voltage of 0.6 V, this can cause the flow to alternate between the transitional and laminar regimes in rapid succession. A secondary analysis was therefore performed to assess the velocity at the end of the excitation period, assuming the fluid velocity responds instantaneously to changes in heater voltage. It should be noted that even at the lowest heater control

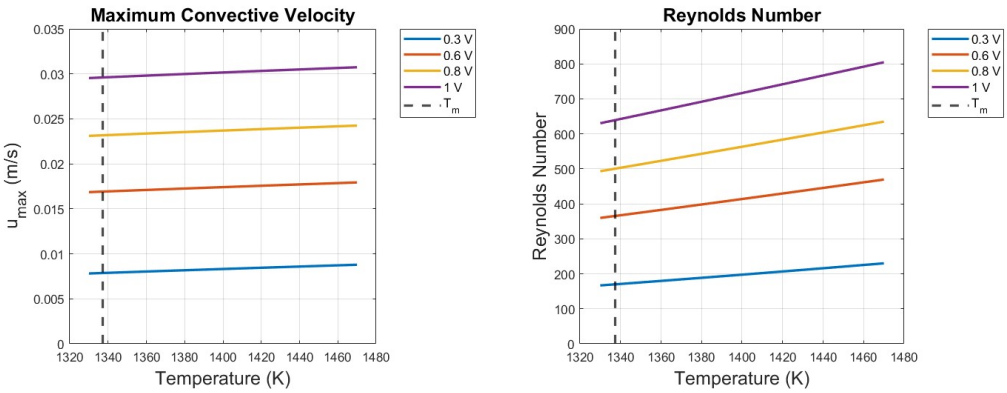

Figure 5.10 : Maximum convective velocity (left) and Reynolds number (right) vs. temperature (K).

voltage used in this study ($U^H_{\text{ctr}} = 0.1$ V), the heater-driven velocity exceeds the positioner contribution, so the net flow direction remains consistent throughout.

A sinusoidal voltage perturbation with amplitude 0.2 V and frequency 18.6 Hz was applied to the median heater control voltage for 2.1 seconds, replicating test conditions. At each time step, the corresponding fluid velocity was computed and combined with the velocity from the previous step using a first-order relaxation model:

$$u_{i+1} = u_i + \frac{\Delta t}{\zeta}\left(u\left(U^H_{\text{ctr}}\right) - u_i\right)$$

where u_i is the current cumulative velocity, $u(U^H_{\text{ctr}})$ is the steady-state velocity at the instantaneous heater voltage, $\Delta t = 0.001$ s is the time step, and ζ is a relaxation parameter controlling the influence of the current heater voltage on the velocity. A small value of $\zeta = 0.005$ was chosen to maximize sensitivity to the sinusoidal excitation, providing a conservative upper bound on the heater-induced velocity fluctuations. As shown in Figure 5.11, the effect of the sinusoidal excitation on the cumulative velocity is negligible. Consequently,

the velocity and Reynolds number throughout each test can be taken as those corresponding to the mean heater control voltage.

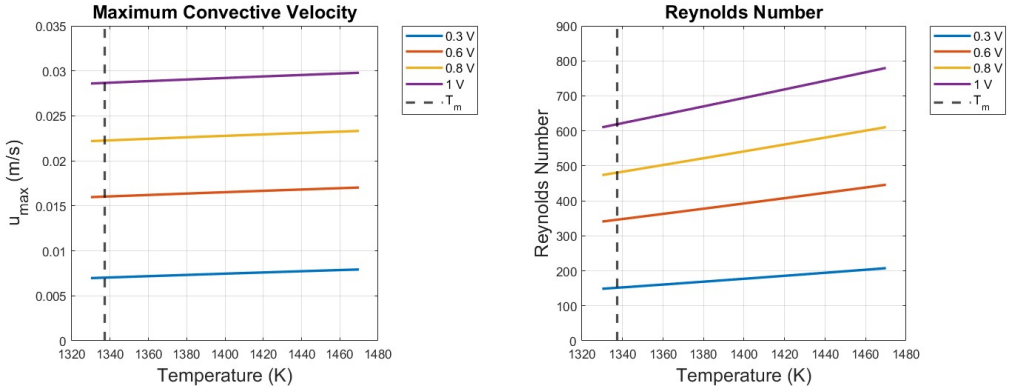

Figure 5.11 : Cumulative convective velocity (left) and Reynolds number (right) vs. time during sinusoidal heater excitation.

5.3.2 Statistical Analysis of Results

Further evidence of fluid velocity's effects is visible in Figure 5.8. Tests conducted in the laminar regime (lower heater control voltages) exhibit a stronger dependence of oscillation frequency on droplet deformation, resulting in a larger correction when the corrected frequency formula is applied. As heater control voltage—and by extension, internal stirring—increases, this deformation dependence diminishes. In the turbulent regime of the 1.0 V test, the deformation dependence is substantially reduced. The two intermediate voltages, 0.6 and 0.8 V, show similar deformation dependence, consistent with both operating near the transitional regime over the tested temperature range.

These trends are reflected in Table 5.5, which shows that surface tension exhibits a stronger temperature dependence at higher heater control voltages, as indicated by the increasing magnitude of the slope m. This dependence is less dramatic than the uncorrected results in Table 4.2. The intercept values,

by contrast, do not show a clear monotonic dependence on stirring level. In the laminar fluid regime, the droplet's oscillation behavior is governed more strictly by the Rayleigh equations, as there are few internal dissipative forces acting within the fluid. Leading to a frequency shift that is more dominated by oscillation behavior and the corrected Rayleigh equation. As the Reynolds number increases, there are more eddies and momentum fluctuations within the fluid that make oscillation behavior stray from that of a quiescent sample. This leads to oscillation behavior that strays slightly from that of deformation-induced frequency shift. This implies that internal stirring causes a significant difference in surface tension derivation that needs to be confirmed with statistical analysis. To assess whether the observed differences in temperature dependence are statistically significant, a chi-squared test was conducted with 3 degrees of freedom and a significance level of $\alpha = 0.05$. Results are reported in Table 5.6.

Table 5.6 : Results of chi-squared test for the effect of stirring on surface tension fit parameters.

Parameter	p-value	Conclusion
Slope	0.0479	Stirring significantly affects temperature dependence
Intercept	0.0411	Stirring significantly affects surface tension at T_m

5.3.3 Extrapolation to Zero Stirring

Having confirmed that internal stirring measurably affects the surface tension results, an extrapolation was performed to estimate the surface tension in the absence of heater-induced convection ($U^H_{\text{ctr}} = 0$). The slope and intercept of each corrected surface tension fit were plotted against heater control voltage, and a linear fit was applied to each set of values. The surface tension param-

eters at zero stirring were then taken as the fitted values at $U_{\text{ctr}}^{H} = 0$. The fits are shown in Figure 5.12 and the extrapolated values are reported in Table 5.7.

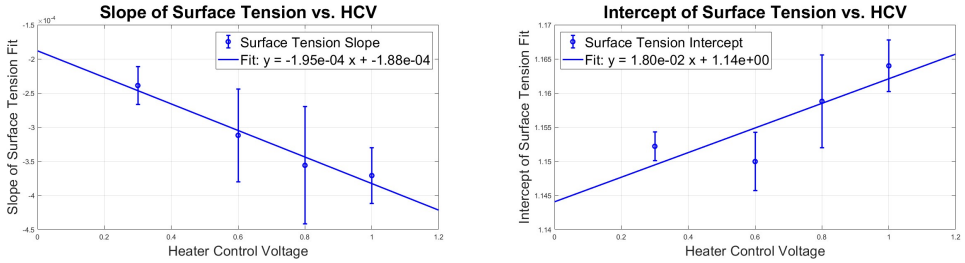

Figure 5.12 : Slope (left) and intercept (right) of the corrected surface tension fit vs. heater control voltage, with linear extrapolation to zero stirring.

Table 5.7 : Extrapolated surface tension parameters at zero stirring.

Parameter	Value
Slope	-0.000188 ± 0.000035 N/m·K
Intercept	1.144 ± 0.0062 N/m

With the surface tension–temperature relationship established at zero stirring, these results can be directly compared to previously reported values in the literature. These results compare well to those presented by Egry and Keene, with Table 5.8 showing the comparison between these results [3, 4].

Table 5.8 : Comparison of Surface Tension Line of Best Fits with Respect to Temperature [3, 4]

Study	Slope (N/mK)	Intercept (N/m)
This Study	-0.000188	1.144
Egry	-0.00014	1.149
Keene	-0.00020	1.145

Additionally, these results can be overlaid with recent EML surface tension results gathered using the pulse excitation method. This is shown below, with the linear fit representing the extrapolated zero-stirring condition.

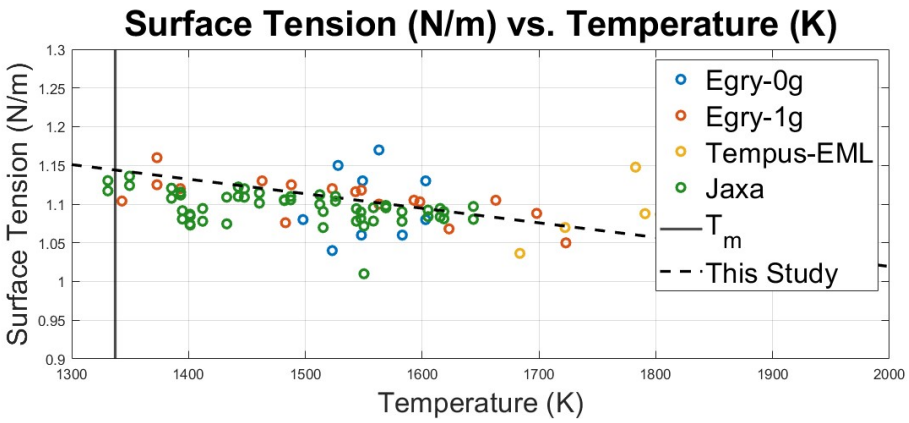

Figure 5.13 : Plot of Previous Surface Tension Results with Extrapolated Zero-Stirring Condition (This Study) Overlaid

A relationship between surface tension and heater control voltage can be constructed for gold using the results from Figure 5.12. Extrapolation to zero heater control voltage results in a lower surface tension at the melting temperature, as indicated by the intercept versus heater control voltage trend, and a reduced temperature dependence of surface tension, as indicated by the slope versus heater control voltage trend.

To extrapolate surface tension measurements to a reference heater control voltage, U^H_{ref}, the voltage dependence of the fitted parameters can be used. An additive correction to the intercept is given by $\Delta\sigma_b = b_{\text{slope}}\left(U^H_{\text{ref}} - U^H_{\text{ctr}}\right)$, where $b_{\text{slope}} = 1.804 \times 10^{-2}\frac{N}{mV}$ is the slope of the intercept versus heater control voltage relationship. Similarly, the correction to the temperature-dependent term is $\Delta\sigma_m = m_{\text{slope}}\left(U^H_{\text{ref}} - U^H_{\text{ctr}}\right)(T - T_m)$, where $m_{\text{slope}} = -1.956 \times 10^{-4}\frac{N}{mKV}$ is the slope of the slope versus heater control voltage relationship.

For extrapolation to zero heater control voltage, $U^H_{\text{ref}} = 0$, these expressions simplify to $\Delta\sigma_b = -b_{\text{slope}}U^H_{\text{ctr}}$ and $\Delta\sigma_m = -m_{\text{slope}}U^H_{\text{ctr}}(T - T_m)$. The corrected

surface tension is therefore

$$\gamma_C = \gamma_{\text{measured}} - m_{\text{slope}} U_{\text{ctr}}^H (T - T_m) - b_{\text{slope}} U_{\text{ctr}}^H.$$

Note that the individual contribution of $\Delta\sigma_b$ decreases surface tension results, while the contribution of $\Delta\sigma_m$ increases surface tension for temperatures above the melting temperature of gold.

This correction can be applied to all surface tension results to give a final dependence of Surface Tension vs. Temperature.

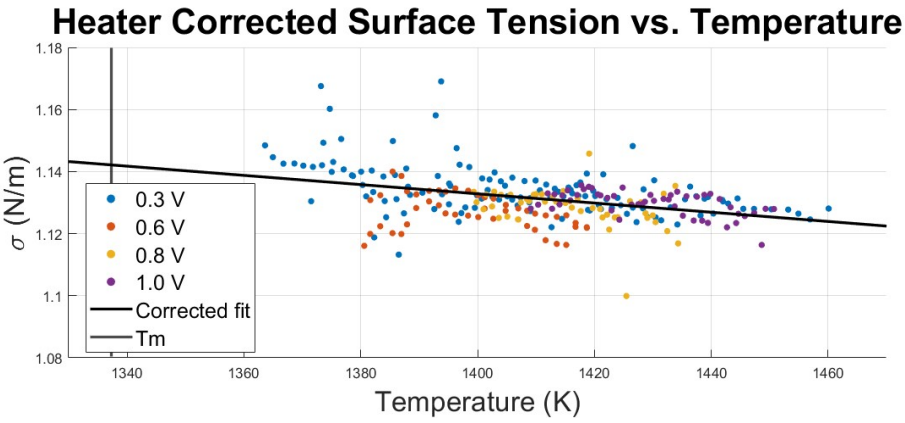

Figure 5.14 : Plot of Surface Tension vs. Temperature with Frequency and Heater Corrections Applied

Table 5.9 : Heater and Frequency Corrected Linear Regression Results

Slope (N/mK)	Intercept (N/m)
$-1.4843 \cdot 10^{-4} \pm 2.09 \cdot 10^{-5}$	$1.1421 \pm 1.61 \cdot 10^{-3}$

5.4 Comparison to Pulse Excitation

A similar analysis was completed by Benjamin Ledru on experimental runs for pulse excitation and is outlined in his thesis, *Surface Tension Measurement of Pure Gold Using Electromagnetic Levitation Pulse Excitation on the International Space Station* [47]. These runs had the same experimental initiative as those run for Faraday forcing: investigate the effect of deformation and stirring.

The results of the pulse excitation tests extrapolated back to zero stirring compare well with the Faraday forcing results and are summarized in Table 5.10. The coefficient of variation, defined as $CV = \frac{u_b}{b}$, is used to quantify the precision of results, with a smaller value relating to greater precision in measurement. Uncertainty in linear fit parameters is calculated through the standard procedure outlined in the GUM [45].

Table 5.10 : Comparison of Zero Stirring Lines of Best Fit Between Pulse Excitation and Faraday Forcing [3, 4]

Study	Slope (N/mK)	Intercept (N/m)	CV (%)
Pulse Excitation	$-0.000149 \pm 1.51 \cdot 10^{-5}$	1.150 ± 0.0022	0.19
Faraday Forcing	$-0.000188 \pm 2.09 \cdot 10^{-5}$	1.142 ± 0.0016	0.14

These results show excellent alignment between the two experimental methods, particularly in the surface tension's temperature dependence. The coefficient of variance shows that Faraday forcing is the more precise method of measuring surface tension and should be used for future testing initiatives. Additionally, the coefficient of variance was calculated for the top and side-view results independently. It was found that the coefficient of variation for the top view is $CV = 0.212\%$ and the side view is $CV = 0.178\%$. This result is consistent with uncertainty analysis, which shows the top view has more uncertainty, as evidenced in Section 6: *Uncertainty Analysis*.

Chapter 6

Uncertainty Analysis

All calculations completed in this section pertain to a datapoint from the top view of cycle 31 with a temperature of 1429.65 K and a frequency of 18.7017 Hz. For side view calculations, representative values were taken from the same cycle.

6.1 Uncertainty in Experimental Methods

Uncertainty is calculated according to the Guide to Uncertainty Measurement for every measured parameter in the surface tension calculation [45]. In surface tension analysis, uncertainty can be attributed to both values derived from physical measurement—mass and temperature—and values derived from curve fitting—ν, δ, p_1, p_2 [46]. For calculations that involve multiple variables with independent uncertainties, the propagation of uncertainty can be calculated using the following formulas, where u is uncertainty and f is the combined equation of parameters x_i through x_N [45].

$$u_{\text{Total}} = \sqrt{\sum_{i=1}^{N} \left(\frac{\partial f}{\partial x_i}\right) u^2(x_i)} \qquad \text{Propagation of Error (General)} \quad (6.1)$$

$$u_{\text{Total}} = \sqrt{\sum_{i=1}^{N} \left(a_i \frac{u(x_i)}{x_i}\right)^2} \qquad \text{Propagation of Error (Multiplication)} \quad (6.2)$$

$$u_{\text{Total}} = \sqrt{\sum_{i=1}^{N} u^2(x_i)} \qquad \text{Propagation of Error (Addition)} \quad (6.3)$$

6.2 Uncertainty in Temperature

Uncertainty in pyrometer-measured temperature values can be defined as the following [46].

$$\frac{u_T}{T} = \sqrt{\left(\frac{1}{T_P}\left(\frac{u(T_P)}{T_P}\right) + \frac{1}{T_{PL}}\left(\frac{u(T_{PL})}{T_{PL}}\right)\right)^2 + \frac{1}{T_L^2}\left(\frac{u(T_L)}{T_L}\right)^2}$$

As a result, finding the associated uncertainties of the apparent pyrometer temperature, the apparent melting temperature, and the true melting temperature is necessary for finding the uncertainty associated with the true temperature. Because both the uncertainties associated with T_P and T_{PL} are associated with the uncertainty of the pyrometry equipment and readings, the terms are coupled [46].

Because gold is a pure element that has been studied extensively for centuries, it is assumed that there is no uncertainty in its true melting temperature. As a result, $u(T_L) = 0$.

A range of temperatures at the melt plateau and a range of temperatures during the cooling profile of Cycle 31 were taken as representative samples of pyrometer recordings. These ranges can be seen in the figure below and were used in determining the uncertainty of the apparent temperature, T_P, and the apparent liquidus temperature, T_{PL}. Uncertainty was calculated by fitting linear lines to both data subsets and calculating the RMS deviation from the fitted line. Both subsets have a sample size of $N = 401$. Fitted lines and uncertainty calculations can be seen below [46].

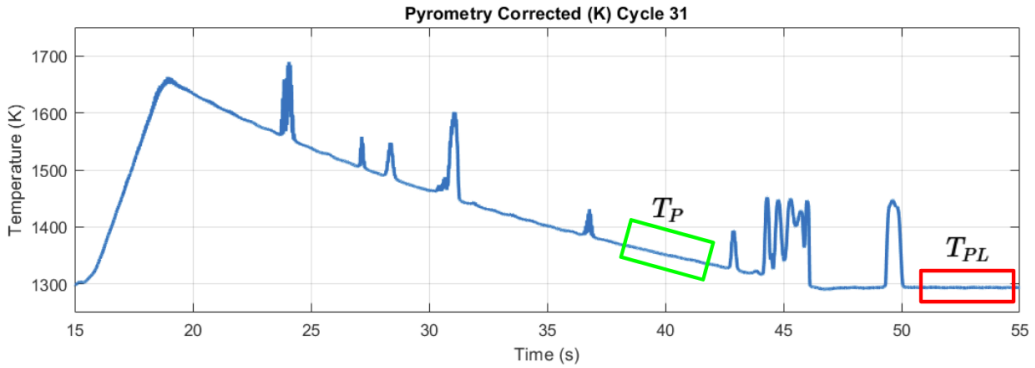

Figure 6.1 : Time-Temperature Profile of Cycle 31 with Boxes Representing Apparent (Green) and Apparent Liquidus (Red) Indices Used for Uncertainty Calculation

$$T_{P,\,\text{Fit}} = 1796.961 - 9.904 \cdot t$$

$$T_{PL,\,\text{Fit}} = 1341.770 - 0.0824 \cdot t$$

$$u(T_P) = \sqrt{\frac{\sum_{i=1}^{N}(T_{P,i} - T_{P,\,\text{Fit},\,i})^2}{N-2}} \qquad = 0.3950\,K$$

$$u(T_{PL}) = \sqrt{\frac{\sum_{i=1}^{N}(T_{PL,i} - T_{PL,\,\text{Fit},\,i})^2}{N-2}} \qquad = 0.2638\,K$$

Given an apparent temperature of $T_P = 1351.3\,K$, which corresponds to the middle value of the T_P subset, and an apparent liquidus temperature of $T_{PL} = 1293.8\,K$, which corresponds to the mean of the T_{PL} subset, uncertainty in terms of percentages can be derived.

$$\frac{u(T_P)}{T_P} = \frac{0.3950}{1351.3} = 0.02923\%$$
$$\frac{u(T_{PL})}{T_{PL}} = \frac{0.2638}{1293.8} = 0.02038\%$$

Using this, we can calculate the uncertainty of the pyrometry data for cycle 31.

$$\frac{u_T}{T} = \sqrt{((0.02923) + (0.02038))^2 + (0)^2}$$

$$\frac{u_T}{T} = 0.05320\%$$

6.3 Uncertainty in Mass

Uncertainty pertaining to the mass of the sample derives from two sources. The first is the scale on which the mass was measured. The sample was weighed on a Mettler Toledo AX105 Delta Range® precision balance with a reported uncertainty of 0.05 mg in its coarse operating range. This gives the first component of mass uncertainty.

$$u_{\text{scale}} = 5 \cdot 10^{-5}\, g$$

Because samples were tested aboard the International Space Station, final massing of the sample has not been completed. To work around this, the ISS-EML has deposition coils that track the total amount of evaporated debris attached to them. Deposition is calculated as a layer thickness onto the closest coil. This coil is located 10.35 mm from the sample center, and thus the total mass evaporated can be estimated as a spherical shell with known thickness at this radius. The following equation calculates evaporated mass, where w is the mass of evaporated debris. Variables are defined in Appendix H.

$$w = S \cdot H \cdot \pi d^2 \cdot A \cdot \frac{e^{-B/T_i}}{\sqrt{T_i}} \cdot \Delta t \cdot 1000$$

By summing the evaporated mass tracked by the deposition coil from cycles 31 to 40, the uncertainty can be determined.

$$u_{\text{evap}} = 3.90 \cdot 10^{-6}\, g$$

Full values of evaporated mass can be found in Appendix H. Because the uncertainty attributed to mass evaporation is so small, formal uncertainty analysis on the equations used to calculate mass evaporation was not evaluated. From these components, a final uncertainty for mass can be obtained.

$$u_m = \sqrt{(u_{\text{scale}})^2 + (u_{\text{evap}})^2} \qquad \text{Uncertainty in Mass} \quad (6.4)$$
$$\frac{u_m}{m} = \sqrt{(5 \cdot 10^{-5})^2 + (3.90 \cdot 10^{-6})^2} = 0.00005\, g$$
$$\frac{u_m}{m} = \frac{0.000050\, g}{2.7496\, g} = 0.0018\%$$

6.4 Uncertainty of Fitted Parameters

Individual uncertainties of fitted parameters come from the covariance matrix, C. In the context of the damped sine curve fit, the covariance matrix is the following [45].

$$\mathbf{C_{DS}} = \begin{bmatrix} \text{Var}(A) & \text{Cov}(A,\tau) & \text{Cov}(A,\nu) & \text{Cov}(A,\phi) & \text{Cov}(A,D) \\ \text{Cov}(\tau,A) & \text{Var}(\tau) & \text{Cov}(\tau,\nu) & \text{Cov}(\tau,\phi) & \text{Cov}(\tau,D) \\ \text{Cov}(\nu,A) & \text{Cov}(\nu,\tau) & \text{Var}(\nu) & \text{Cov}(\nu,\phi) & \text{Cov}(\nu,D) \\ \text{Cov}(\phi,A) & \text{Cov}(\phi,\tau) & \text{Cov}(\phi,\nu) & \text{Var}(\phi) & \text{Cov}(\phi,D) \\ \text{Cov}(D,A) & \text{Cov}(D,\tau) & \text{Cov}(D,\nu) & \text{Cov}(D,\phi) & \text{Var}(D) \end{bmatrix} \quad (6.5)$$

Individual uncertainties for variables can be derived by taking the square roots of the variance terms, $u(x_i) = \sqrt{C_{ii}}$. Additionally, if two terms are related, their covariance term, C_{ij}, must be included in the uncertainty calculation [45].

6.5 Uncertainty in Frequency

Because frequency measurement derives from high-speed camera videos that are thresholded with edge-detection video processing, there exists uncertainty associated with the edge detection and the frame rate of the high-speed camera. With these three factors considered, the final uncertainty in frequency can be defined. In the following equation, u_{fit} represents the uncertainty in the curve fit, u_{fps} represents the uncertainty resulting from the frame rate, and u_r is the error in the radius of the sample [46, 45].

$$\frac{u_\nu}{\nu} = \sqrt{\left(\frac{u_r}{r}\right)^2 + \left(\frac{u_{\text{fit}}}{\text{fit}}\right)^2 + \left(\frac{u_{\text{fps}}}{\text{fps}}\right)^2} \qquad \text{Uncertainty in Frequency} \qquad (6.6)$$

The error in the radius can be defined as the following, where px_{exp} is the spherical radius of the droplet in pixels, px_{cal} is the radius of the calibration sphere in pixels, and r_{cal} is the true radius of the calibration sphere [46].

$$\frac{u_r}{r} = \sqrt{\left(\frac{u_{px,exp}}{px_{exp}} + \frac{u_{px,cal}}{px_{cal}}\right)^2 + \left(\frac{u_{r,cal}}{r_{cal}}\right)^2} \qquad \text{Uncertainty in Radius} \qquad (6.7)$$

The calibration sphere has a diameter of 6.705394 ± 0.000813 mm.

$$\frac{u_{r,cal}}{r_{cal}} = \frac{0.000813}{6.70539} = 0.0124\% \qquad (6.8)$$

Uncertainty pertaining to pixel measurements was taken over a representative number of data points, $N = 300$. The standard deviation of the pixel count

is the uncertainty associated with the measurement, while the mean of the pixel count is treated as the 'true' reading. The same value of uncertainty will be used for the pixel count of the calibration sphere. This is a conservative assumption, as the uncertainty $u_{px,exp}$ is associated with a molten liquid experiencing translation combined with deformation induced by sample spin, while the calibration sphere is shape invariant. This yields relative uncertainties as follows.

$$\frac{u_{px,exp}}{px_{exp}} = \frac{u_{px,cal}}{px_{cal}} = \frac{0.6305}{103.1642} = 0.611\%$$

With this information, we can determine the uncertainty in the radius.

$$\frac{u_r}{r} = \sqrt{(0.00611 + 0.00611)^2 + (0.000124)^2} = 1.22\%$$

The uncertainty associated with the curve fit of the frequency comes from the $C_{3,3}$ term of the damped sine covariance matrix.

$$\frac{u_{\text{fit}}}{\text{fit}} = \frac{0.0049}{18.7017} = 0.0262\%$$

Finally, the error associated with the frame rate is at most

$$u_{\text{fps}} = \left(\frac{1}{2}\right)\left(\frac{\nu}{\text{Sampling Rate}}\right) = \left(\frac{1}{2}\right)\left(\frac{18.7071}{\text{Sampling Rate}}\right)$$

Because videos are recorded at both 150 Hz for the axial view and 400 Hz for the radial view, this frequency uncertainty changes accordingly.

$$\frac{u_{\text{fps}}}{\text{fps}} = \left(\frac{1}{2}\right)\left(\frac{18.701}{150}\right) = 6.23\% \qquad \text{Uncertainty in Axial View}$$

$$\frac{u_{\text{fps}}}{\text{fps}} = \left(\frac{1}{2}\right)\left(\frac{18.701}{400}\right) = 2.33\% \qquad \text{Uncertainty in Radial View}$$

With these factors included, the uncertainty of the frequency can be determined.

$$\frac{u_\nu}{\nu} = \sqrt{\left(\frac{u_r}{r}\right)^2 + \left(\frac{u_{\text{fit}}}{\text{fit}}\right)^2 + \left(\frac{u_{\text{fps}}}{\text{fps}}\right)^2} = \sqrt{(0.0122)^2 + (0.000262)^2 + (0.0623)^2}$$

$$\frac{u_\nu}{\nu} = 6.34\% \qquad \text{Top View}$$

$$\frac{u_\nu}{\nu} = \sqrt{\left(\frac{u_r}{r}\right)^2 + \left(\frac{u_{\text{fit}}}{\text{fit}}\right)^2 + \left(\frac{u_{\text{fps}}}{\text{fps}}\right)^2} = \sqrt{(0.0122)^2 + (0.000262)^2 + (0.0233)^2}$$

$$\frac{u_\nu}{\nu} = 2.63\% \qquad \text{Side View}$$

6.6 Uncertainty in Linear Regression

Uncertainty in both the slope and intercept of linear equations are of particular importance in the chi-squared statistical test performed to determine statistical independence. For linear fits, the uncertainty is defined as follows for inputs x_i, outputs y_i, and a number of datapoints N.

$$u_m = \frac{s_{yx}}{\sqrt{\sum (x_i - \bar{x})^2}} \qquad \text{Slope Uncertainty} \qquad (6.9)$$

$$u_b = s_{yx}\sqrt{\frac{1}{N} + \frac{\bar{x}^2}{\sum (x_i - \bar{x})^2}} \qquad \text{Intercept Uncertainty} \qquad (6.10)$$

$$s_{yx} = \sqrt{\frac{\sum y_i^2 - b\sum y_i - m\sum x_i y_i}{N-2}} \qquad \text{Standard Error} \qquad (6.11)$$

6.7 Uncertainty in Surface Tension

Uncertainty in uncorrected surface tension is a function of both mass and frequency, with a quadratic dependence on frequency.

$$\frac{u_\gamma}{\gamma} = \sqrt{\left(\frac{u_m}{m}\right)^2 + \left(2\frac{u_\nu}{\nu}\right)^2} \qquad \text{Uncertainty in Surface Tension} \qquad (6.12)$$

With both the mass and frequency uncertainty determined, the uncorrected surface tension uncertainty for the given datapoint from a top view video can be determined.

$$\frac{u_\gamma}{\gamma} = \sqrt{(0.0018)^2 + (2(6.34))^2} = 12.68\%$$

The same process can be applied for a datapoint from the side view with its own associated uncertainty in frequency.

$$\frac{u_\gamma}{\gamma} = \sqrt{(0.0018)^2 + (2(2.63))^2} = 5.26\%$$

Given that the datapoint has an associated surface tension, the absolute uncertainty in surface tension can be defined.

$$\gamma = \frac{3}{8}\pi m\nu^2 = \frac{3}{8}\pi(0.002749\,\mathrm{kg})(18.7017\,\mathrm{Hz})^2 = 1.133\,\mathrm{N}\cdot\mathrm{m}^{-1}$$

$$u_\gamma = 1.133(0.1286) = 0.14\,\mathrm{N}\cdot\mathrm{m}^{-1}$$

6.8 Uncertainty in Deformation

6.8.1 Top View

Top view deformation has two parameters, A and D.

$$\delta = \sqrt{\frac{|A| + D}{D}} - 1 \tag{6.13}$$

Using the general form of uncertainty propagation, the uncertainty for the top view can be defined as the following.

$$\frac{u_\delta}{\delta} = \sqrt{\left(\frac{\partial \delta}{\partial A}\right)^2 \left(\frac{u_A}{A}\right)^2 + \left(\frac{\partial \delta}{\partial D}\right)^2 \left(\frac{u_D}{D}\right)^2 + 2\frac{\partial \delta}{\partial A}\frac{\partial \delta}{\partial D} C_{A,D}} \tag{6.14}$$

$$\frac{\partial \delta}{\partial A} = \frac{A}{2D|A|\sqrt{\frac{|A|+D}{D}}} \qquad \frac{\partial \delta}{\partial D} = -\frac{|A|}{2D^2\sqrt{\frac{|A|+D}{D}}}$$

Uncertainties for the values of A and D come from the damped sine covariance matrix, $C_{1,1}$ and $C_{5,5}$. Note that A and D are from the same video that produced the uncertainty in radius, u_r. Because A and D are derived from the same video data, and u_r is included in the propagation of uncertainty for u_ν, including u_r here would double-count its contribution to uncertainty when propagated to the uncertainty in corrected surface tension. Additionally, the oscillation signal comes from variations in A and D, not explicitly from a radius measurement. Hence, it is omitted from the deformation uncertainty calculation. Because A and D come from the same curve fit, they are correlated parameters. This warrants the inclusion of their covariance term $C_{1,5}$.

If $\frac{u_A}{A} = \frac{0.4626}{1489.5} = 0.0310\%$ and $\frac{u_D}{D} = \frac{53.822}{42396} = 0.127\%$ from the datapoint being analyzed, the uncertainty in top view deformation can be determined. The negative sign for $\partial\delta/\partial D$ is removed for convenience, as uncertainties should

always be positive.

$$\frac{\partial\delta}{\partial A} = \frac{A}{2D|A|\sqrt{\frac{|A|+D}{D}}} = 1.16 \cdot 10^{-5} \qquad \frac{\partial\delta}{\partial D} = \frac{|A|}{2D^2\sqrt{\frac{|A|+D}{D}}} = 4.073 \cdot 10^{-7}$$

Taking the covariance term to be $C_{1,5} = 7.199$,

$$\frac{u_\delta}{\delta} = \sqrt{\left(\frac{\partial\delta}{\partial A}\right)^2\left(\frac{u_A}{A}\right)^2 + \left(\frac{\partial\delta}{\partial D}\right)^2\left(\frac{u_D}{D}\right)^2 + 2\frac{\partial\delta}{\partial A}\frac{\partial\delta}{\partial D}C_{A,D}} = 0.000133\%$$

6.8.2 Side View

Side view deformation is dependent on A, which represents the difference between the equatorial and polar radii in the side view, and R_0, the spherical radius of the droplet.

$$\delta = \frac{1 - \sqrt{1 - 4(\frac{A}{3R_0})}}{2}$$

Using the general form of uncertainty propagation, the uncertainty in the side view deformation can be expressed as the following.

$$\frac{u_\delta}{\delta} = \sqrt{\left(\frac{\partial\delta}{\partial A}\right)^2\left(\frac{u_A}{A}\right)^2 + \left(\frac{\partial\delta}{\partial R_0}\right)^2\left(\frac{u_{R_0}}{R_0}\right)^2} \quad \text{Uncertainty in Side Deformation} \tag{6.15}$$

$$\frac{\partial\delta}{\partial A} = \frac{1}{3R_0\sqrt{1 - \frac{4A}{3R_0}}} \qquad \frac{\partial\delta}{\partial R_0} = -\frac{A}{3R_0^2\sqrt{1 - \frac{4A}{3R_0}}}$$

Similar to top-view deformation, the uncertainty in A comes from the damped sine covariance matrix, $C_{1,1}$. R_0, however, comes directly from the video measurement and is thus equivalent to u_r. Because the side view deformation depends on a separate measurement of R_0, rather than on the variation of two cross-correlated parameters as in the top view, the uncertainty in radius must be included.

Taking $A = 9.6190$ px, $R_0 = 206.337$ px, $\frac{u_A}{A} = \frac{0.123}{9.6190} = 1.27\%$, and $\frac{u_{R_0}}{R_0} = \frac{u_r}{r} = 1.22\%$, the uncertainty for side view deformation can be determined.

$$\frac{\partial \delta}{\partial A} = \frac{1}{3R_0\sqrt{1-\frac{4A}{3R_0}}} = 0.00169 \qquad \frac{\partial \delta}{\partial R_0} = -\frac{A}{3R_0^2\sqrt{1-\frac{4A}{3R_0}}} = 0.0000777$$

$$\frac{u_\delta}{\delta} = \sqrt{\left(\frac{\partial \delta}{\partial A}\right)^2\left(\frac{u_A}{A}\right)^2 + \left(\frac{\partial \delta}{\partial R_0}\right)^2\left(\frac{u_{R_0}}{R_0}\right)^2} = 0.0533\%$$

It must also be noted that there is an associated error in the side view deformation calculation due to the truncation of the Taylor polynomial. For a side view deformation of 0.0096, the associated truncation error is

$$\text{error} = \frac{1}{\delta}\left(\frac{1}{(1+\delta)^2} - (1 - 2\delta + 3\delta^2)\right)$$
$$\text{error} = \frac{1}{0.0096}\left(\frac{1}{(1+0.0158)^2} - (1 - 2(0.0096) + 3(0.0096)^2)\right)$$
$$\text{error} = -0.0364\%$$

Taking the sum of the absolute values of both the uncertainty and the error gives the final uncertainty of side view deformation.

$$\frac{u_\delta}{\delta} = 0.0533\% + 0.0364\% = 0.0897\%$$

It can be seen that there is more associated uncertainty in side view deformation than in top view deformation.

6.9 Uncertainty in Corrected Surface Tension

The input parameters to the corrected Rayleigh equation are ν, m, δ, p_1, and p_2. Uncertainty in deformation correction factors p_1 and p_2 is excluded

from this analysis. The associated uncertainty of these parameters is high due to the limited number of data points for each heater control run. Additionally, the focus of this uncertainty analysis is on the experimental methods employed. Including the large uncertainties associated with these correction factors would cause them to dominate over the uncertainties of the experimental methods. With this in mind, the uncertainty in corrected surface tension can be calculated using the following equation.

$$\frac{u_{\gamma,c}}{\gamma_c} = \sqrt{\left(\frac{u_m}{m}\right)^2 + \left(2\frac{u_\nu}{\nu}\right)^2 + \left(\frac{1}{\gamma_c}\frac{\partial \gamma_c}{\partial \delta}\right)^2 \left(\frac{u_\delta}{\delta}\right)^2} \tag{6.16}$$

$$\frac{1}{\gamma_c}\frac{\partial \gamma_c}{\partial \delta} = \frac{p_1 + p_2\delta}{1 + p_1\delta + p_2\delta^2}$$

Cycle 31 was run with a heater control voltage of 0.3 V, and thus $p_1 = 0$ and $p_2 = -2.713$ with associated deformation $\delta = 0.0096$. Using this in addition to the derived uncertainties from earlier yields a final uncertainty for the top view video of

$$\frac{u_{\gamma,c}}{\gamma_c} = \sqrt{\left(\frac{u_m}{m}\right)^2 + \left(2\frac{u_\nu}{\nu}\right)^2 + \left(\frac{1}{\gamma_c}\frac{\partial \gamma_c}{\partial \delta}\right)^2 \left(\frac{u_\delta}{\delta}\right)^2} = 12.68\%$$

If viewing from the side, the uncertainty changes. Note that the same deformation $\delta = 0.0096$ was used for demonstrative purposes; in practice, the deformation values would not be equivalent.

$$\frac{u_{\gamma,c}}{\gamma_c} = \sqrt{\left(\frac{u_m}{m}\right)^2 + \left(2\frac{u_\nu}{\nu}\right)^2 + \left(\frac{1}{\gamma_c}\frac{\partial \gamma_c}{\partial \delta}\right)^2 \left(\frac{u_\delta}{\delta}\right)^2} = 5.26\%$$

It can be seen that uncertainty in frequency heavily dominates the uncertainty analysis, and there is less associated uncertainty in side view videos as a result of the increased sampling rate.

6.10 Tabular Summary of Results

Table 6.1 : Summary of Relative Uncertainty Results

Variable	Relative Uncertainty (%)
$\frac{u_T}{T}$	0.0532
$\frac{u_m}{m}$	0.0018
$\frac{u_{\text{fps}}}{\text{fps}}$ (Top)	6.23
$\frac{u_{\text{fps}}}{\text{fps}}$ (Side)	2.33
$\frac{u_\nu}{\nu}$ (Top)	6.34
$\frac{u_\nu}{\nu}$ (Side)	2.63
$\frac{u_\gamma}{\gamma}$ (Top)	12.68
$\frac{u_\gamma}{\gamma}$ (Side)	5.26
$\frac{u_\delta}{\delta}$ (Top)	0.000133
$\frac{u_\delta}{\delta}$ (Side)	0.0897
$\frac{u_{\gamma,c}}{\gamma_c}$ (Top)	12.68
$\frac{u_{\gamma,c}}{\gamma_c}$ (Side)	5.26

Chapter 7

Conclusion

This thesis serves as an experimental study of the derivation of gold's thermophysical properties dependence on both droplet deformation and induced stirring within the ISS-EML. To study the effect of deformation, we applied Faraday excitation, typical of ESL testing, on gold droplets and mapped the frequency of oscillation to both the Rayleigh equation and the corrected Rayleigh equation. To study the effect of stirring, tests were run at five separate heater control voltages, which all induce different velocities within the droplet. Quantification of the velocities was provided through the use of a surrogate model [13].

In this regard, it was found that deformation produces a marked decrease in oscillating frequency for gold, a result consistent with that found by Xiao et al. on a LEK-94 alloy [34]. This is evidenced by the reduction of both surface tension intercept at the melting point, b, and surface tension's temperature dependence between the preliminary results expressed in Table 4.2 and the post-correction results expressed in Table 5.5. Frequency was shown to map quadratically to deformation across all heater control voltages studied, as evidenced in Figure 5.8, which is, again, consistent with the results shown by Xiao et al. [34]. After correction, the surface tension results were only a function of temperature and heater control voltage, not deformation. Statistical analysis of the deformation-corrected results showed that there is a statistical dependence between surface tension results and heater control voltage. With

statistical dependence confirmed, a relationship between heater control voltage and linear fit parameters m and b could be produced. The results of which were used to create a surface tension correction formula dependent on both temperature and heater control voltage.

$$\sigma_C = \sigma_{\text{measured}} - m_{\text{slope}} U^H_{\text{ctr}} (T - T_m) - b_{\text{slope}} U^H_{\text{ctr}}$$

This additive correction formula allows for the use of Faraday forcing as a primary technique in future ISS-EML studies of pure gold, as it facilitates surface tension correction for stirring without sweeping through a range of heater control values, like was done in this work. Validation of this work's results against prior surface tension results, Egry aboard the Columbia space shuttle and Keene from ground-based experiments, shows validity in the methodology used and provides merit for these methods to be used on other materials. Notably, pulse-excitation faces noticeable stirring in the first tenth of a second of testing. Because the relationship between surface tension and heater control voltage is generalizable, this equation can be used to correct surface tension values across testing methods.

Another primary objective of this work is the determination of Faraday forcing as an experimental technique in EML environments. With forcing conducted at a single frequency for a prolonged time, excitation frequency can influence the frequency measurements of free damping. It was found that the free damping frequencies recorded immediately after the end of excitation were consistently lower than that of the excitation frequencies, showing independence. As the temperature decreased during cooling, frequencies characteristically increased and surpassed that of the excitation frequency. The results

from Faraday forcing EML results align well with previous measurements of gold's surface tension, both measured in microgravity and terrestrially. Finally, comparison with pulse excitation results tested with the same gold sample and levitator shows good alignment between stirring corrected results of the two experimental methods. Additionally, Faraday forcing shows a decreased coefficient of variation at the melting point [47]. This proves the validity of Faraday forcing as an experimental method for EMLs with appropriate stirring correction.

The successful implementation of Faraday forcing as a testing method in EML environments represents a meaningful advancement in microgravity research. This is especially important for the determination of viscosity in EML experiments. Typical EML procedures, when pulse excitation is used, results in a fast decrease in internal stirring. Over the course of a single pulse, samples transition from higher to lower Reynolds numbers, which can represent different flow regimes, complicating analysis. Because Faraday forcing can focus on a single Reynolds number, higher fidelity can be achieved in these measurements. This not only represents a positive step in microgravity research but also in the fidelity of predictive models as well, as having a validated, correctable excitation method available in microgravity directly improves the quality and reliability of the property databases these models depend on.

Chapter 8

Future Work

While the primary objectives of this thesis were met, directions for further experimentation were left unexplored. This contains the following aspects:

- **Different Models of Deformation** — Fahimi *et al.* discuss different methods of defining deformation in an oscillating droplet. Namely, they mention a 'volume moved' metric that is defined as the amount of volume displaced in oscillation from a perfect sphere. Comparison of deformation correction introduced by Xiao *et al.* and Fahimi *et al.* is unexplored and can lead to model improvements [34, 48].

- **Improving Heater Correction** — This study defines a correction of surface tension results based on a given heater control voltage. The correction formula was based on a linear relationship between both the intercept and slope of surface tension curves with heater control voltage. This judgment is based off of four data points, which may not be enough to fully determine the behavior. Future studies should increase the range of heater control voltage studied, especially above 1.0 V, to fully determine whether a linear relationship is appropriate.

- **Improving Surrogate Model Parameters** — The relationship between viscosity and temperature was not defined for the gold sample used in the experiment. Instead, literature values were used. By determining the viscosity of the sample, model fidelity can be improved and extrapolated to more testing scenarios.

- **Isothermal Comparison** — Typically, Faraday forcing is used in isothermal tests, where the temperature remains constant throughout the experiment. This allows for a multitude of reliable data points at each temperature. Alternatively, this study focuses on an active cooling approach. Cross comparison between the two methods has not been studied for EML environments. Future work can focus on determining whether the two methods yield similar results.

- **Quantification of Heater Field** — When the heater voltage is set to 0 V, residual magnetic fields associated with the heater are created through operation of the ISS-EML. While the field is small, it warrants the re-evaluation of this work with respect to experienced heater field, not heater control voltage.

This research serves as the first effort of implementing Faraday excitation in an EML environment. With results validating the use of the techniques with the use of a stirring correction factor, extensions of the application of Faraday Excitation should be investigated.

- **Viscosity with Faraday Excitation** — Viscosity has a well-defined and stronger relationship with stirring than surface tension. Because Faraday excitation induces more prolonged but consistent stirring with samples, it can be used to define the viscosity of metals at precise flow conditions.

Bibliography

[1] A. Seidel, W. Soellner, and C. Stenzel, "Uncertainty analysis and performance evaluation of thermophysical property measurement of liquid au in microgravity," *Journal of Physics: Conference Series*, vol. 327, 2011.

[2] M. Mohlenkamp, "A user's guide to spherical harmonics," 2016.

[3] I. Egry, E. Schwartz, J. Szekely, G. Jacobs, G. Lohoefer, and P. Neuhaus, "Surface tension measurements on liquid metals in microgravity," *Metallurgical and Materials Transactions B*, vol. 29, 1998.

[4] B. Keene, "Review of data for the surface tension of pure metals," *International Materials Review*, vol. 38, 1993.

[5] N. Brosius, Z. K. J. Livesay, R. Singiser, M. SanSoucie, B. Phillips, and R. Narayanan, "Characterization of oscillation modes in levitated droplets using image and non-image based technique," *Microgravity*, vol. 9, no. 3, 2023.

[6] I. Egry, G. Lohoefer, and G. Jacobs, "Surface tension of liquid metals: Results from measurements on ground and in space," *Physical Review Letters*, vol. 75, 1995.

[7] P. Gradl, "Metal additive manufacturing for rocket propulsion applications," 2022.

[8] D. Adak, P. Sreeramagiri, S. Roy, and G. Balasubramanian, "Advances

and challenges in predictive modeling for additive manufacturing of dissimilar metals and complex alloys," 2023.

[9] J. Nawer, T. Ishikawa, H. Oda, H. Saruwatari, C. Koyama, X. Xiao, S. Schneider, M. Kolbe, and D. Matson, "Uncertainty analysis and performance evaluation of thermophysical property measurement of liquid au in microgravity," vol. 9, 2023.

[10] J. Nawer, T. Ishikawa, H. Oda, C. Koyama, and D. Matson, "Uncertainty quantification of thermophysical property measurement in space and on earth: A study of liquid platinum using electrostatic levitation," *Journal of Astronomy and Space Sciences*, vol. 40, 2023.

[11] I. Egry, G. Jacobs, E. Schwartz, and J. Szekely, "Surface tension measurements of metallic melts under microgravity," *International Journal of Thermophysics*, vol. 17, 1996.

[12] E. Baker, J. Nawer, X. Xiao, and D. Matson, "Mhd surrogate model for convection in electromagnetically levitated molten metal droplets processed using the iss-eml facility," *npj Microgravity*, vol. 6, no. 9, 2020.

[13] X. Xiao, R. Hyers, and D. Matson, "Surrogate model for convective flow inside electromagnetically levitated molten droplet using magnetohydrodynamic simulation and feature analysis," *International Journal of Heat and Mass Transfer*, vol. 136, pp. 531–542, 2019.

[14] A. Diefenbach and S. S. andT. Volkmann, *Experiment Preparation and Performance for the Electromagnetic Levitator (EML) Onboard the International Space Station.* IntechOpen, 2020.

[15] D. M. Matson, L. Battezzati, P. K. Galenko, C.-A. Gandin, A. K. G. amd H. Henein, K. F. Kelton, M. Kolbe, J. Valloton, S. C. Vogel, and T. Volk-

mann, "Electromagnetic levitation containerless processing of metallic materials in microgravity: rapid solidification," *NPJ Microgravity*, 2023.

[16] J. Witteveen, M. Vrielink, R. van Gastel, A. van Houselt, and H. Zandvliet, "Containerless metal single-crystal growth via electromagnetic levitation," *Rev. Sci. Instrum*, vol. 92, 2021.

[17] J. Rogers and M. SanSoucie, "Containerless processing studies in the msfc electrostatic levitator," *American Institute of Aeronautics and Astronautics*, 2012.

[18] M. SanSoucie, "Levitation capabilities on ground and in space," 2021.

[19] Z. Xi, X. Shuo, and L. Jing, "Surface tension of liquid metal: role, mechanism and application," *Frontiers in Energy*, vol. 228, 2023.

[20] J. Douillard and F. Salles, "Phenomenology of water adsorption at clay surfaces," *Interface Science and Technology*, vol. 1, 2004.

[21] P. Systeme, "Surface tension by the ring method (du nuoy method)," tech. rep., PHYWE Series of Publications, 2005.

[22] S. Blairs and M. Abbas, "Correlation between surface tension and critical temperatures of liquid metals," *Journal of Colloid and Interface Science*, vol. 304, 2006.

[23] F. Aqra and A. Ayyad, "Theoretical temperature-dependence surface tension of pure liquid gold," *Materials Letters*, vol. 65, 2011.

[24] L. Rayleigh, *On the Capillary Phenomena of Jets.* Royal Society Publishing, 1879.

[25] H. Kitahara, R. Tanaka, Y. Koyano, S. Matsumoto, K. Nishinari, T. Watanabe, K. Hasegawa, T. Kanagawa, A. Kaneko, and Y. Abe,

"Oscillation of a rotating levitated droplet: Analysis with a mechanical model," *Physical Review E*, vol. 92, 2015.

[26] E. Yakhshi-Tafti, R. Kumar, and H. Cho, "Measurement of surface interfacial tension as a function of temperature using pendant drop images," *International Journal of Optomechatronics*, vol. 5, 2011.

[27] R. Delahaije, L. Sagis, and J. Yang, "Impact of particle sedimentation in pendant drop tensiometry," *Langmuir*, vol. 33, 2022.

[28] K. Lewis and T. Matsuura, "Calculation of the meniscus shape formed under gravitational force by solving the young–laplace differential equation using the bézier curve method," *ACS Omega*, vol. 7, 2022.

[29] M. Neeson, D. Chan, and R. Tabor, "Compound pendant drop tensiometry for interfacial tension measurement at zero bond number," *Langmuir*, vol. 30, 2014.

[30] J. Berry, M. Neeson, R. Dagastine, D. Chan, and R. Tabor, "Measurement of surface and interfacial tension using pendant drop tensiometry," *Journal of Colloid and Interface Science*, vol. 454, pp. 226–237, 2015. Includes detailed comparisons of force-based vs. optical methods.

[31] E. de Farias, R. Fermam, and A. de Mendonça, "Comparison between the wilhelmy surface tension measurement method and the pendant drop shape analysis method," *Acta Polytechnica*, 2025.

[32] S. Ebnesajjad, *Surface Treatment of Materials for Adhesive Bonding*. William Andrew, 2014.

[33] D. Matson, X. Xiao, J. Rodriguez, and R. Wunderlich, "Preliminary experiments using electromagnetic levitation on the international space

station," *International Journal of Microgravity Science and Application*, vol. 33, 2016.

[34] X. Xiao, R. Hyers, R. Wunderlich, H. Fecht, and D. Matson, "Deformation induced frequency shifts of oscillating droplets during molten metal surface tension measurement," *Applied Physics Letters*, vol. 113, 2018.

[35] P. Coates and D. Lowe, *The Fundamentals of Radiation Thermometers*. CRC Group, 2017.

[36] C. Jing, Z. XueCong, L. Dan, L. HaiJing, and Z. Yang, "Standard photoelectric pyrometer," *Measurement: Sensors*, vol. 38, 2025.

[37] R. Linton, "The optical properties of platinum and gold in the vacuum ultraviolet," tech. rep., NASA Marshall Space Flight Center, 1972.

[38] A. Tiwari, R. Samanta, and H. Chattopadhyay, "Droplet solidification: Physics and modelling," *Applied Thermal Engineering*, vol. 228, 2023.

[39] J. Lee, X. Xiao, D. Matson, and R. Hyers, "Numerical prediction of the accessible convection range for an electromagnetically levitated fe50co50 droplet in space," *Metallurgical and Materials Transactions*, 2015.

[40] X. Xiao, J. Lee, R. Hyers, and D. Matson, "Numerical representations for flow velocity and shear rate inside electromagnetically levitated droplets in microgravity," *npj Microgravity*, vol. 5, no. 7, 2019.

[41] T. Iida, R. Guthrie, M. Isac, and N. Tripathi, "Accurate predictions for the viscosities of several liquid transition metals, plus barium and strontium," *Metallurgical and Materials Transactions B*, vol. 37B, 2006.

[42] D. M. Matson, "Sample preparation procedure for gold (au) for iss-eml batch 4 flight sample 122."

[43] X. Xiao, J. Brillo, J. Lee, R. W. Hyers, and D. M. Matson, "Impact of convection on the damping of an oscillating droplet during viscosity measurement using the iss-eml facility," *Microgravity*, 2021.

[44] R. W. Hyers, G. Trapaga, and B. Abedian, "Laminar-turbulent transition in an electromagnetically levitated droplet," *Metallurgical and Materials Transactions B*, vol. 34, 2003.

[45] JCGM, "Evaluation of measurement data – Guide to the expression of uncertainty in measurement," Tech. Rep. JCGM 100:2008, Joint Committee for Guides in Metrology, Sèvres, France, 2008.

[46] D. Matson, J. Nawer, K. Bergeron, and B. Phillips, "Expressing uncertainty using regression and gum for derived property measurements based on uncertainty in input quantities." In Print for High Temperatures-High Pressures.

[47] B. Ledru, "Surface tension measurement of pure gold using electromagnetic levitation pulse excitation on the international space station," Master's thesis, Tufts University, 2026.

[48] K. Fahimi, L. Madler, and N. Ellendt, "Exploring droplet oscillation dynamics in surface tension measurements," *Experiments in Fluids*, vol. 65, no. 12, 2024.

Sample Historical Data Sheet

1. Historical Record Sheets (CER-08)

	Historical Record Sheet
EML GSP4, Batch 4	Science team ELFSTONE - Matson Sample composition **Au** Sample ID: **#FS 122-1** Priority: 1 Mass [g] 2.7496 Minimal diameter [mm] 6.45 Average diameter [mm] 6.510 ± 0.042 Maximal diameter [mm] 6.57
Requirements for storage	The samples were desiccated in ethanol and placed in the plastic bottles labelled with sample ID in air before integration into the Sample transfer container which contains a 1 atm Argon shield
Requirements for handling before and during integration	Default procedure using plastic tweezers and nitrile gloves to limit potential for scratching

Date	Activity, Procedure	Remarks	performed by
07.08.2023	Cut from gold wire at Tufts University	Raw stock same as GB test	Matson
21.08.2023	Induction-melted at Binnion, lathe machined to shape	Surface roughness retained	Binnion
28.08.2023	Shipped to Tufts in air	Gold is inert, no gas shield.	Binnion
28.08.2023	Runners removed for chemical analysis, stored in glass bottles	Gold is inert, no gas shield	Matson
07.09.2023	Integrated into EXI-STC 12 position 1		Matson

Sample Calculation

All calculations will be completed on Cycle 31 Top View Data.

B.1 Surface Tension Calculation

After completing edge detection on the high-speed video and curve fitting the signal data, values for the observed frequency of the oscillation can be obtained.

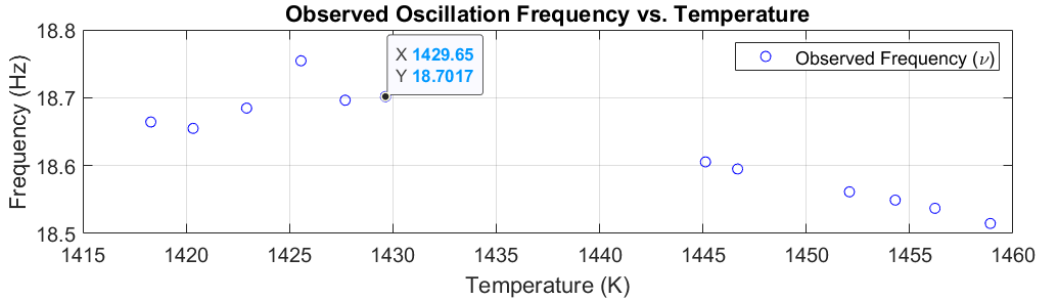

Figure B.1 : Observed Frequency (Hz) vs. Temperature (K) for Cycle 31 Top View

Consider point (1429.65, 18.7017). Curve fitting additionally reveals that for this segment, $A = 1489.5\,\text{pixels}^2$ and $D = 42396.0\,\text{pixels}^2$. These values can be used to determine deformation.

$$\delta = \sqrt{\frac{|A| + D}{D}} - 1 \qquad \text{Top View Deformation}$$

$$\delta = \sqrt{\frac{1489.5 + 42396.0}{42396.0}} - 1 \qquad \text{Substitution}$$

$$\delta = 0.01741$$

This process can be completed for every segment in the cycle. The frequencies, their associated deformations, and temperatures must be stored. Once sufficient data are recorded, they can be fit against the corrected frequency formula to yield the following fit.

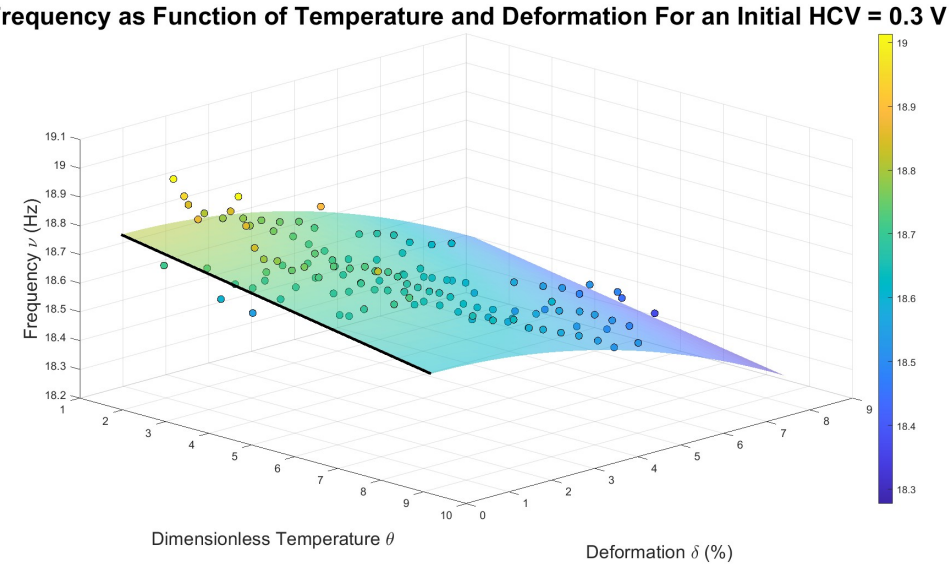

Figure B.2 : Corrected Frequency Formula Applied to 0.3 HCV Dataset with $\nu_{\theta=0} = 18.91$, $p_1 = -0$, $p_2 = -2.713$, $p_\theta = -0.139$, and $R^2 = 0.695$

These correction factors can be applied to the corrected Rayleigh equation to find the corrected surface tension of the material.

$$\sigma = \frac{3}{8}\pi m\nu^2(1 + p_1\delta + p_2\delta^2)$$
$$\sigma = \frac{3}{8}\pi \left(\frac{2.7496}{1000}\ \text{kg}\right)(18.7017\ \text{Hz})^2\left(1 - 0 \cdot 0.01741 - 2.713 \cdot 0.01741^2\right)$$
$$\sigma = 1.1320\,\frac{\text{N}}{\text{m}}$$

B.2 Pyrometry Correction

For a specific temperature reading given by the pyrometer, T_P, the true value of the temperature can be derived using the liquidus temperature of the ma-

terial, T_L, and the pyrometer reading of the liquidus temperature, T_{PL}. The liquidus reading can be determined from the temperature recorded after recalescence from undercooling, as seen below.

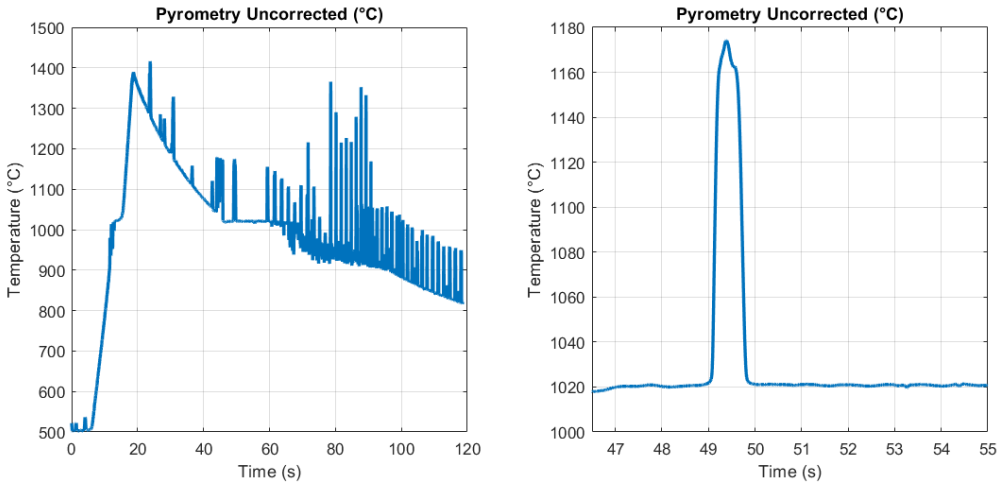

Figure B.3 : Full Temperature Profile (Left) and Subsection of Melt Plateau (Right) for Cycle 31

There is no significant undercooling in this temperature profile. The temperature recorded after recalescence is $T_{PL} = 1020.4\,^{\circ}\mathrm{C} = 1293.4\,\mathrm{K}$. Given that the true liquidus temperature for gold is $T_L = 1338\,\mathrm{K}$, the true temperature of a pyrometry reading at $T_P = 1204.15\,\mathrm{K}$ can be calculated.

$$\left(\frac{1}{T} - \frac{1}{T_L}\right) = \left(\frac{1}{T_P} - \frac{1}{T_{PL}}\right) \qquad \text{Correction Equation}$$

$$\left(\frac{1}{T} - \frac{1}{1338\,\mathrm{K}}\right) = \left(\frac{1}{1204.1\,\mathrm{K}} - \frac{1}{1293.4\,\mathrm{K}}\right) \qquad \text{Substitution}$$

$$T = \left(\frac{1}{1204.1\,\mathrm{K}} - \frac{1}{1293.4\,\mathrm{K}} + \frac{1}{1338\,\mathrm{K}}\right)^{-1} \qquad \text{Solve for } T$$

$$T = 1242.66\,\mathrm{K}$$

B.3 Velocity Calculation

The maximum velocity of fluid flow in the droplet is calculated using the following equation:

$$u_{\max}, \dot{\gamma}_{\max} = \sum_{i,j,k,s} q_{\text{ijks}} \cdot \left(U_{\text{ctr}}^{H}\right)^{i} \cdot \left(\rho^{j}\right) \cdot (\ln \mu)^{k} \cdot (\ln \sigma_{\text{el}})^{s} - \sum_{i,j,k,s} p_{\text{ijks}} \cdot \left(U_{\text{ctr}}^{P}\right)^{i} \cdot \left(\frac{1}{\sqrt{\sigma_{\text{el}}}}\right)^{j} \cdot \left(\rho^{k}\right) \cdot \left(\frac{1}{\ln(\mu)}\right)^{s}$$

When expanded, the equation takes the following form.

$$\begin{aligned}
u_{\max},\ \dot{\gamma}_{\max} = {} & q_{0000} + q_{0001}(\ln \sigma_{\text{el}}) + q_{0010}(\ln \mu) + q_{0011}(\ln \mu)(\ln \sigma_{\text{el}}) + q_{0012}(\ln \mu)(\ln \sigma_{\text{el}})^2 \\
& + q_{0021}(\ln \mu)^2(\ln \sigma_{\text{el}}) \\
& + q_{1000}(U_{\text{ctr}}^{H}) + q_{1001}(U_{\text{ctr}}^{H})(\ln \sigma_{\text{el}}) + q_{1002}(U_{\text{ctr}}^{H})(\ln \sigma_{\text{el}})^2 \\
& + q_{1010}(U_{\text{ctr}}^{H})(\ln \mu) + q_{1011}(U_{\text{ctr}}^{H})(\ln \mu)(\ln \sigma_{\text{el}}) + q_{1020}(U_{\text{ctr}}^{H})(\ln \mu)^2 \\
& + q_{1100}(U_{\text{ctr}}^{H})(\rho) + q_{1101}(U_{\text{ctr}}^{H})(\rho)(\ln \sigma_{\text{el}}) + q_{1110}(U_{\text{ctr}}^{H})(\rho)(\ln \mu) + q_{1200}(U_{\text{ctr}}^{H})(\rho)^2 \\
& + q_{2000}(U_{\text{ctr}}^{H})^2 + q_{2001}(U_{\text{ctr}}^{H})^2(\ln \sigma_{\text{el}}) + q_{2010}(U_{\text{ctr}}^{H})^2(\ln \mu) + q_{2100}(U_{\text{ctr}}^{H})^2(\rho) \\
& + q_{3000}(U_{\text{ctr}}^{H})^3 \\
& - (p_{0000} + p_{0001}(\tfrac{1}{\sqrt{\sigma_{\text{el}}}}) + p_{0002}(\tfrac{1}{\sqrt{\sigma_{\text{el}}}})^2 + p_{0003}(\tfrac{1}{\sqrt{\sigma_{\text{el}}}})^3 \\
& + p_{0010}(\rho) + p_{0011}(\rho)(\tfrac{1}{\sqrt{\sigma_{\text{el}}}}) + p_{0012}(\rho)(\tfrac{1}{\sqrt{\sigma_{\text{el}}}})^2 \\
& + p_{0100}(\tfrac{1}{\ln \mu}) + p_{0101}(\tfrac{1}{\ln \mu})(\tfrac{1}{\sqrt{\sigma_{\text{el}}}}) \\
& + p_{0200}(\tfrac{1}{\ln \mu})^2 + p_{0201}(\tfrac{1}{\ln \mu})^2(\tfrac{1}{\sqrt{\sigma_{\text{el}}}}) + p_{0300}(\tfrac{1}{\ln \mu})^3 \\
& + p_{1000}\,(U_{\text{ctr}}^{P}) + p_{1001}\,(U_{\text{ctr}}^{P})(\tfrac{1}{\sqrt{\sigma_{\text{el}}}}) \\
& + p_{1100}\,(U_{\text{ctr}}^{P})(\tfrac{1}{\ln \mu}) + p_{1101}\,(U_{\text{ctr}}^{P})(\tfrac{1}{\ln \mu})(\tfrac{1}{\sqrt{\sigma_{\text{el}}}}) + p_{1200}\,(U_{\text{ctr}}^{P})(\tfrac{1}{\ln \mu})^2)
\end{aligned}$$

Using the tabulated coefficients provided in Baker et. al and the material properties found in Table 2.4, the maximum velocity can be calculated for a

single temperature [12]. Assuming a temperature of 1400 K, a heater control voltage of 0.3 V, and a positioner voltage of 4.0 V, the maximum velocity within the sample can be defined.

$$\rho = 17233 - 1.168(1400 - 1337.33) = 17131.5 \text{ kg} \cdot \text{m}^{-3}$$
$$\mu = 5.7976 \cdot 10^{-4} \exp\left(\frac{2.65(1337.33)^{1.27}}{(8.13)(1400)}\right) = 0.00486 \text{ Pa} \cdot \text{s}$$
$$\sigma_{\text{el}} = \left(2.500 \cdot 10^{-7} + 4.937 \cdot 10^{-11}(1400 - 1337.33)\right)^{-1} = 3.951 \cdot 10^{6} \text{ S} \cdot \text{m}^{-1}$$
$$u_{\max} = 0.0083 \text{ m} \cdot \text{s}^{-1}$$

To calculate the Reynolds number, the spherical diameter of the droplet must be calculated.

$$V = \frac{m}{\rho} = \frac{2.7496 \text{ g}}{0.0171315 \text{ g} \cdot \text{mm}^{-3}} = 160.49 \text{ mm}^3$$
$$D = \sqrt[3]{\frac{6V}{\pi}} = \sqrt[3]{\frac{6(160.49 \text{ mm}^3)}{\pi}} = 6.742 \text{ mm}$$
$$Re = \frac{\rho u_{\max} D}{\mu} = \frac{(17131.5 \text{ kg} \cdot \text{m}^{-3})(0.0083 \text{ m} \cdot \text{s}^{-1})(0.006742 \text{ m})}{0.00486 \text{ Pa} \cdot \text{s}} = 197.2$$

This corresponds to laminar flow within the metallic droplet.

Pyrometer Corrected Time-Temperature Profiles

Cycle 31, HCV: 0.3 V

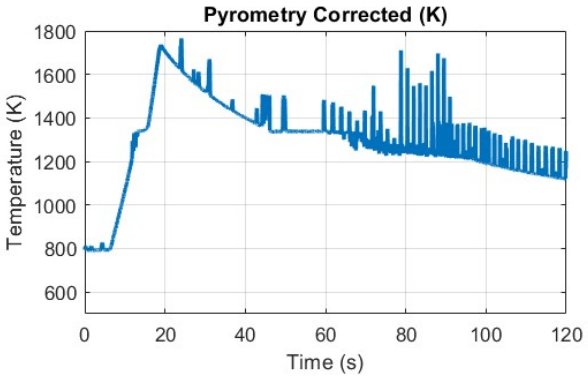

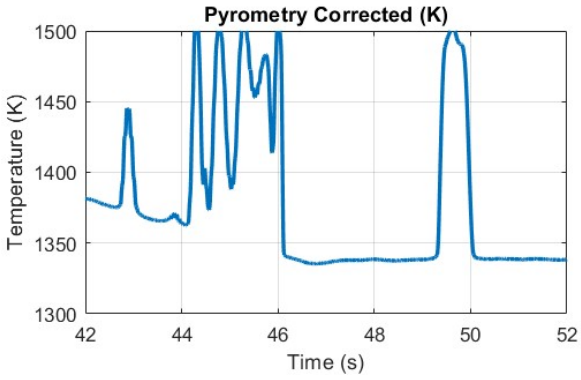

Cycle 32, HCV: 0.3 V

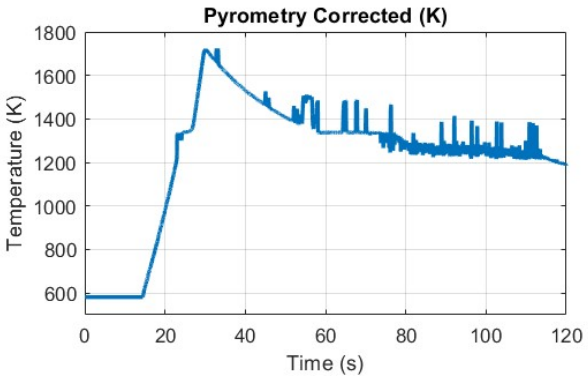

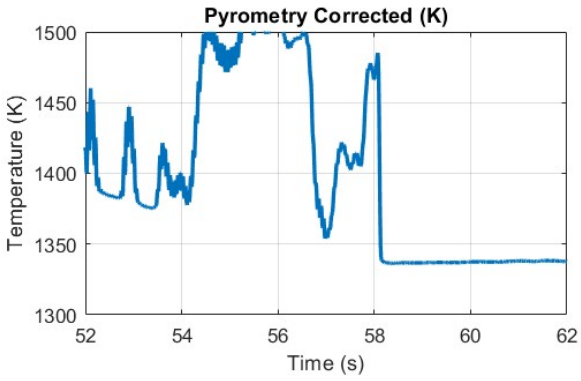

Cycle 33, HCV: 0.3 V

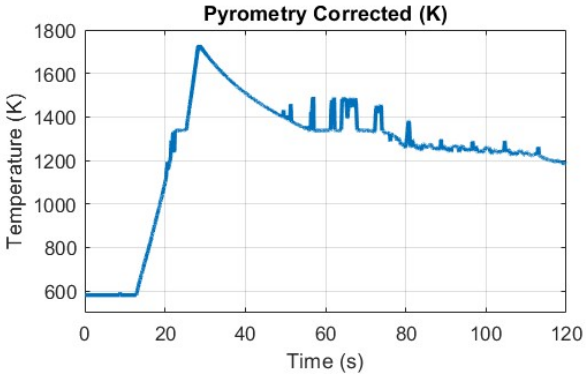

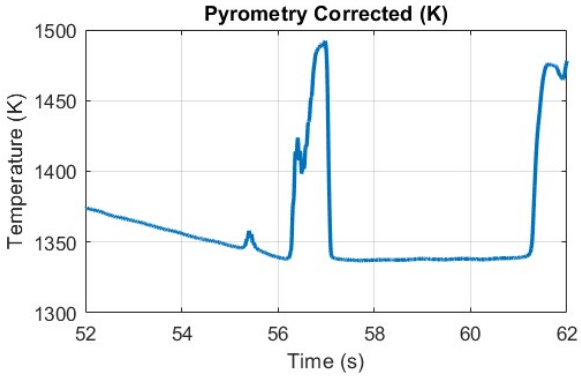

Cycle 34, HCV: 0.3 V

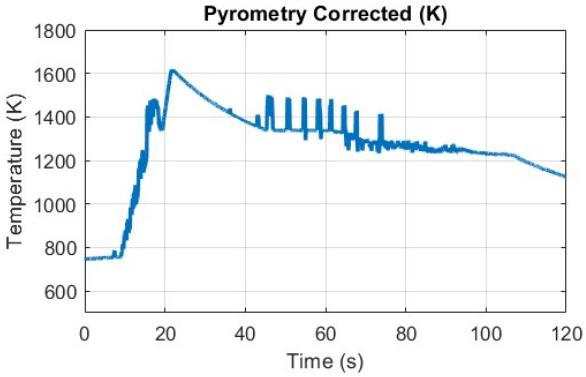

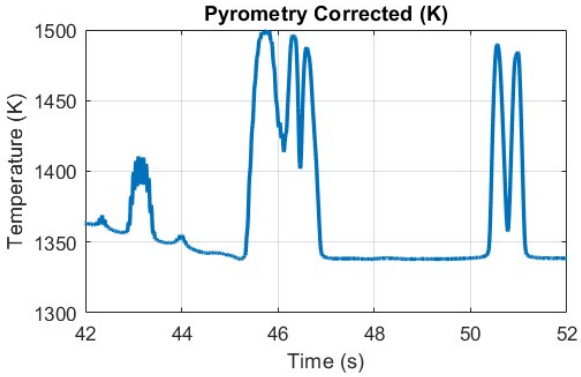

Cycle 36, HCV: 0.5 V

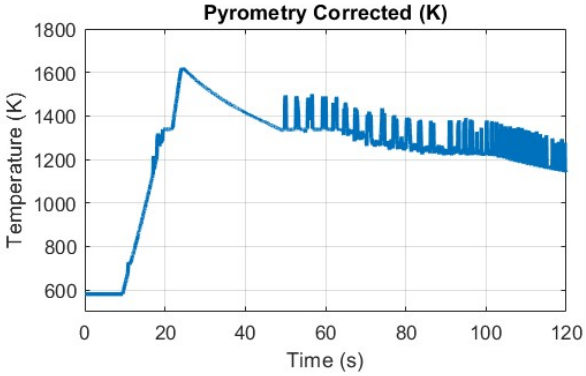

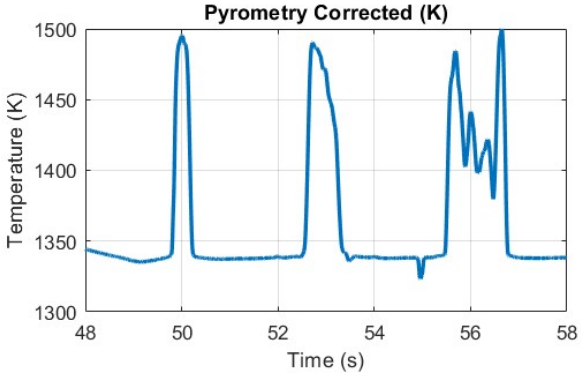

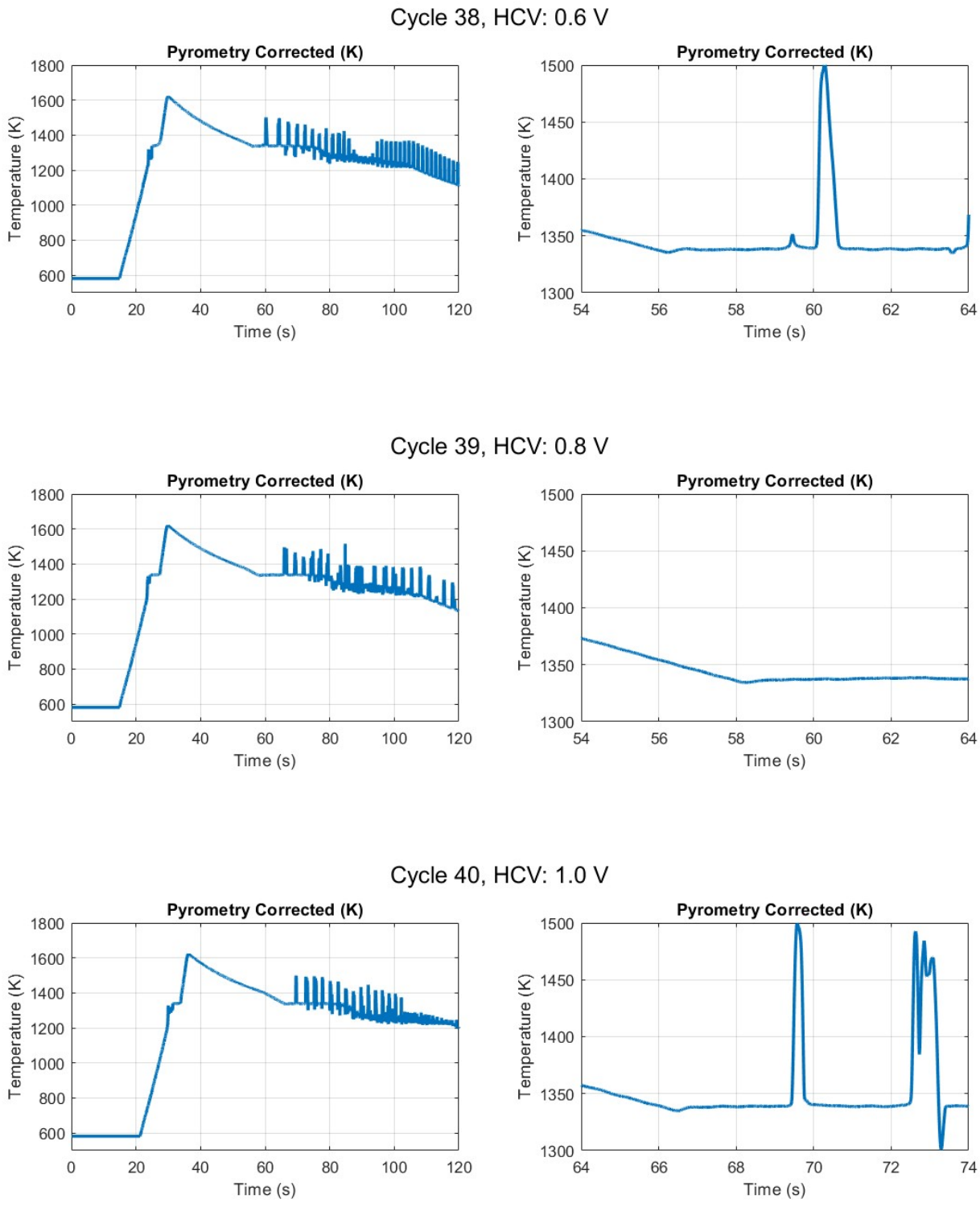

Figure C.1 : Corrected Pyrometry Time (s) Temperature (K) Profiles for All Cycles

Uncorrected Surface Tension Profiles

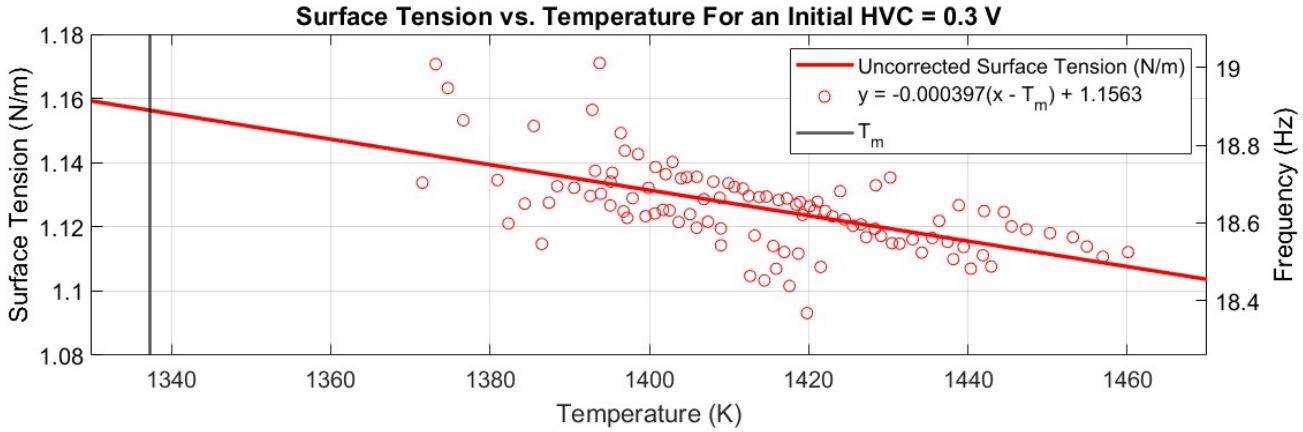

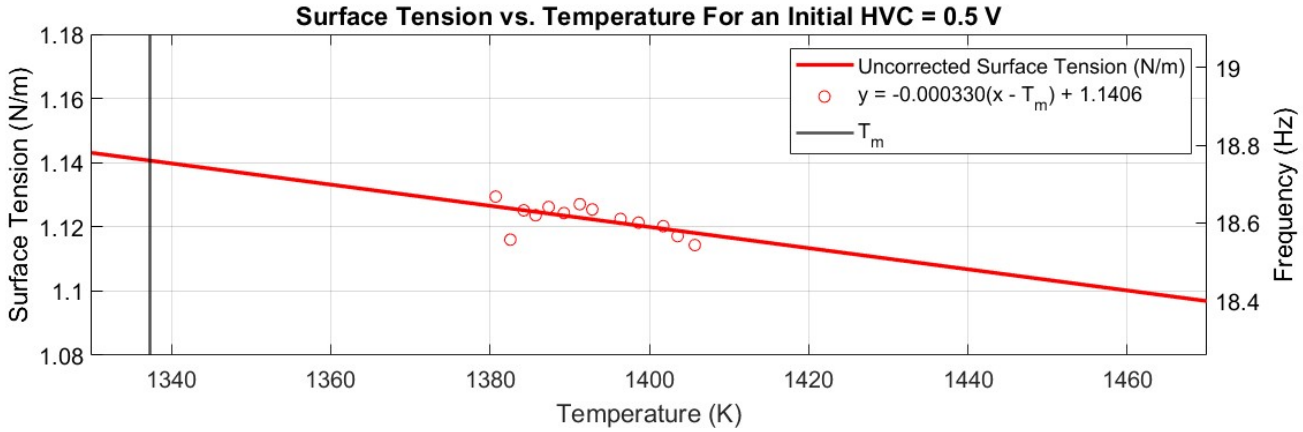

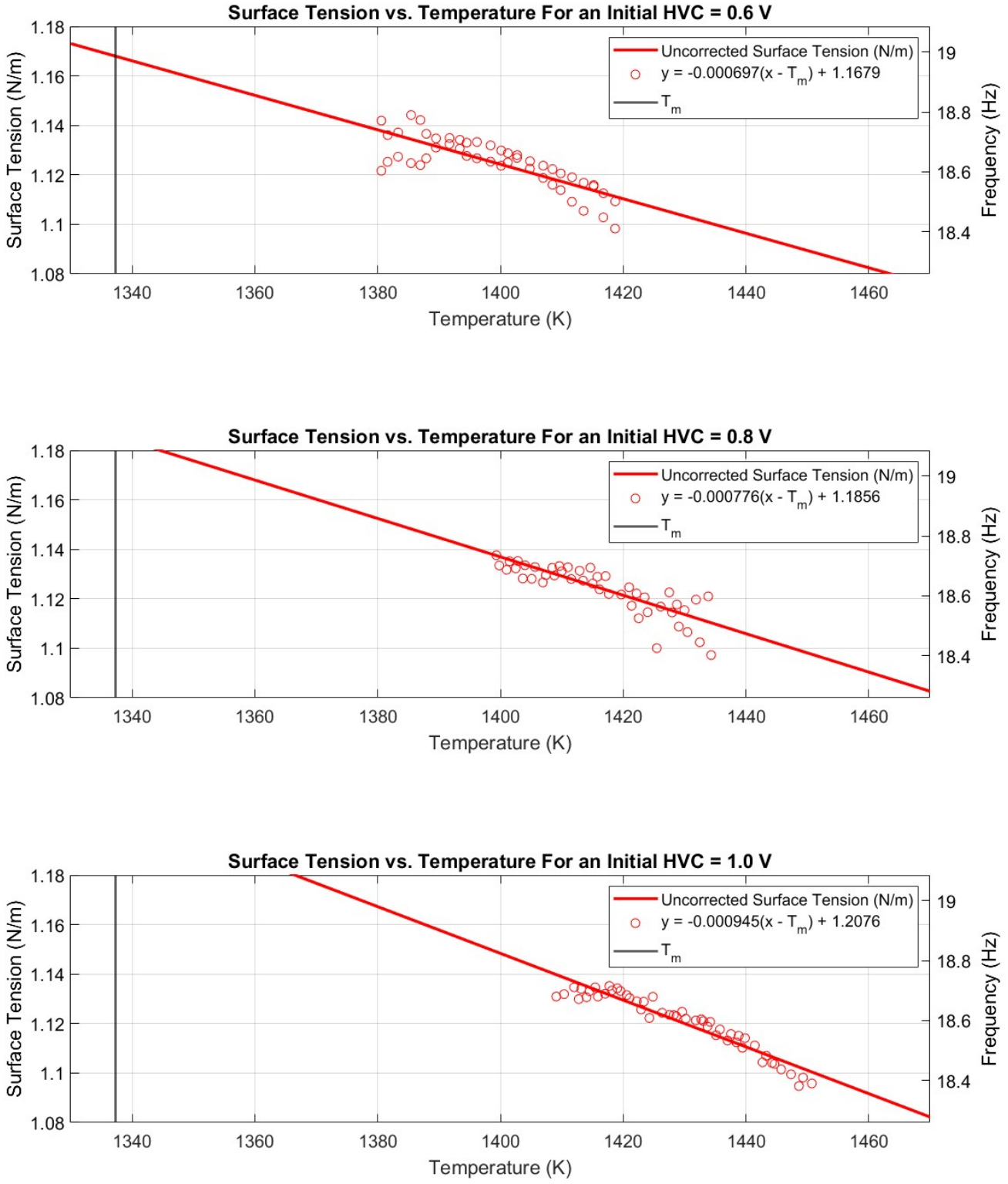

Figure D.1 : Individual Uncorrected Surface Tension vs. Temperature Profiles for HCV Values of 0.3, 0.5, 0.6, 0.8 and 1.0 V Respectively

Corrected Rayleigh Equation Curve Fits

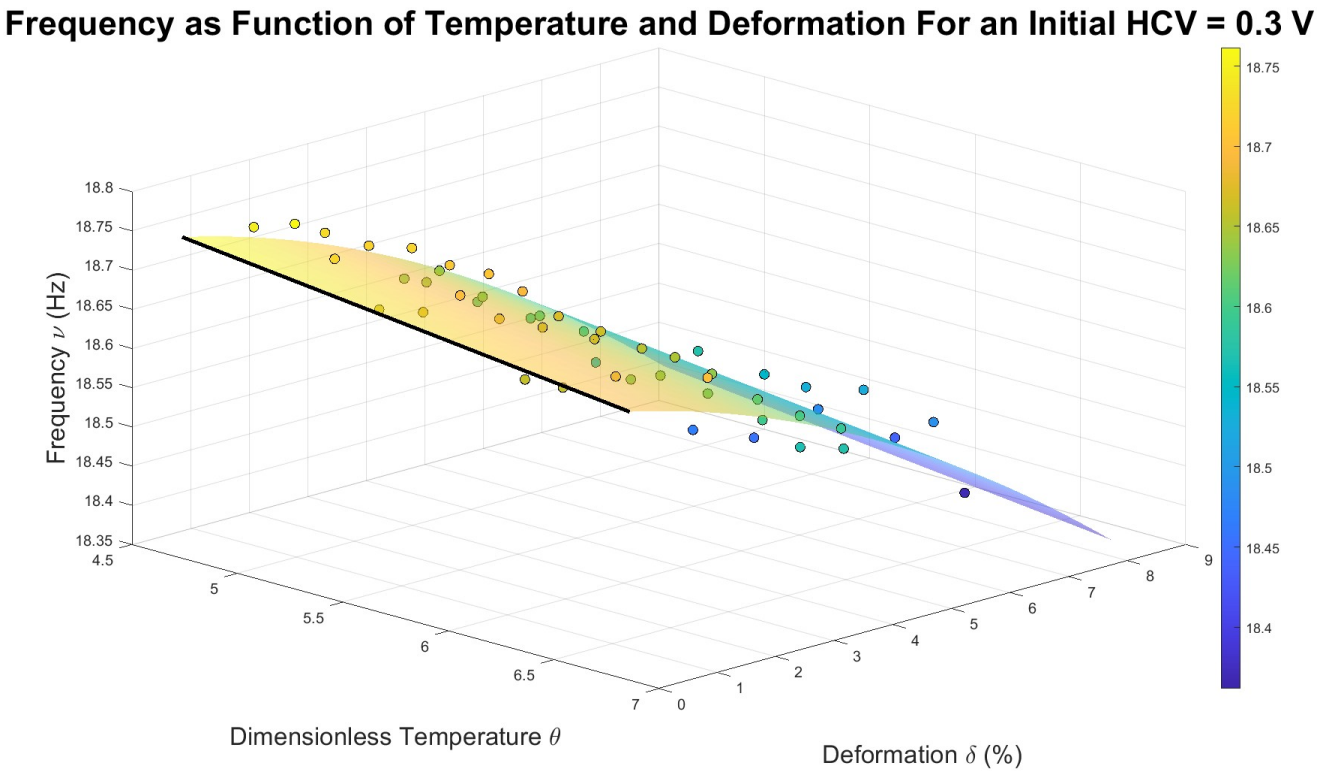

Frequency as Function of Temperature and Deformation For an Initial HCV = 0.5 V

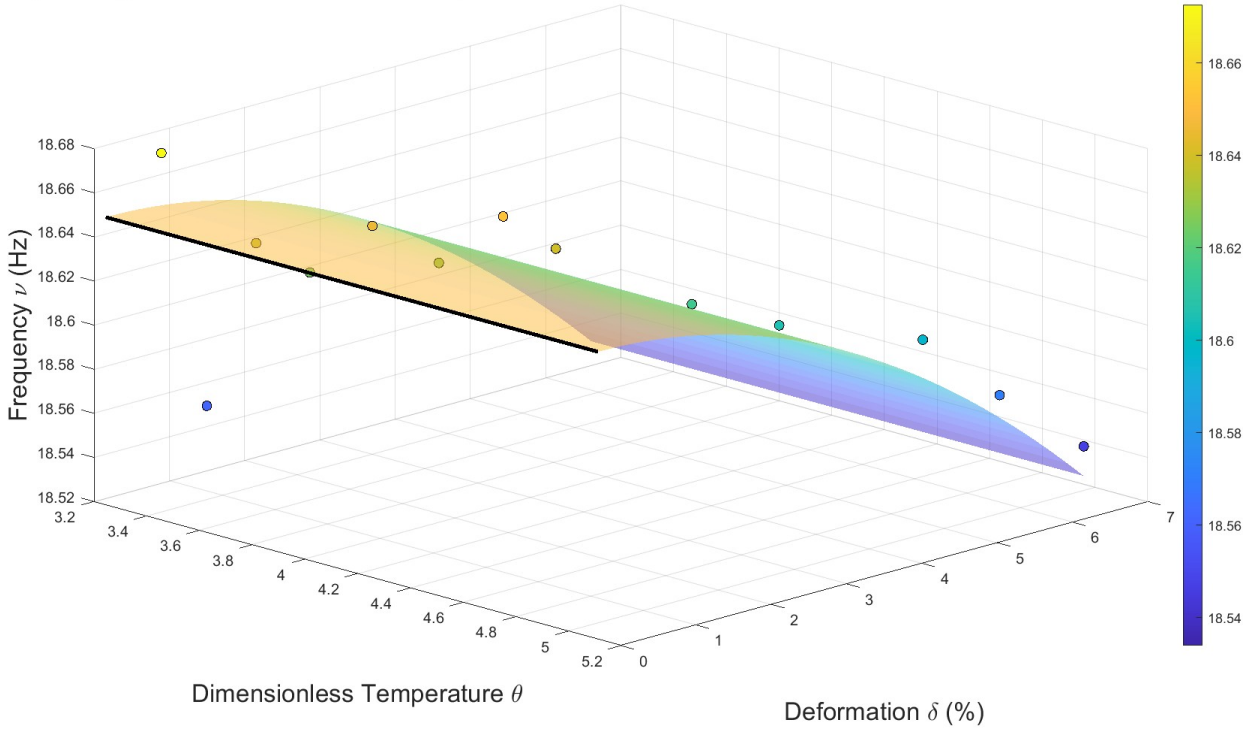

Frequency as Function of Temperature and Deformation For an Initial HCV = 0.6 V

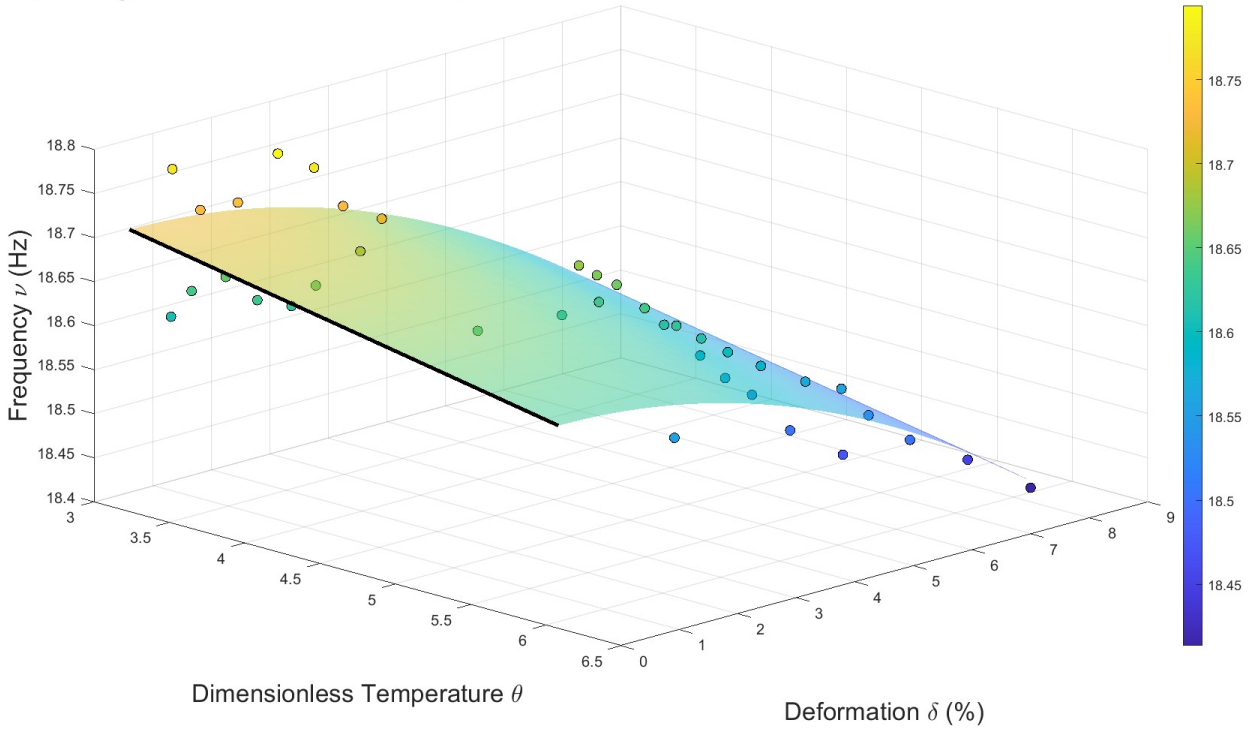

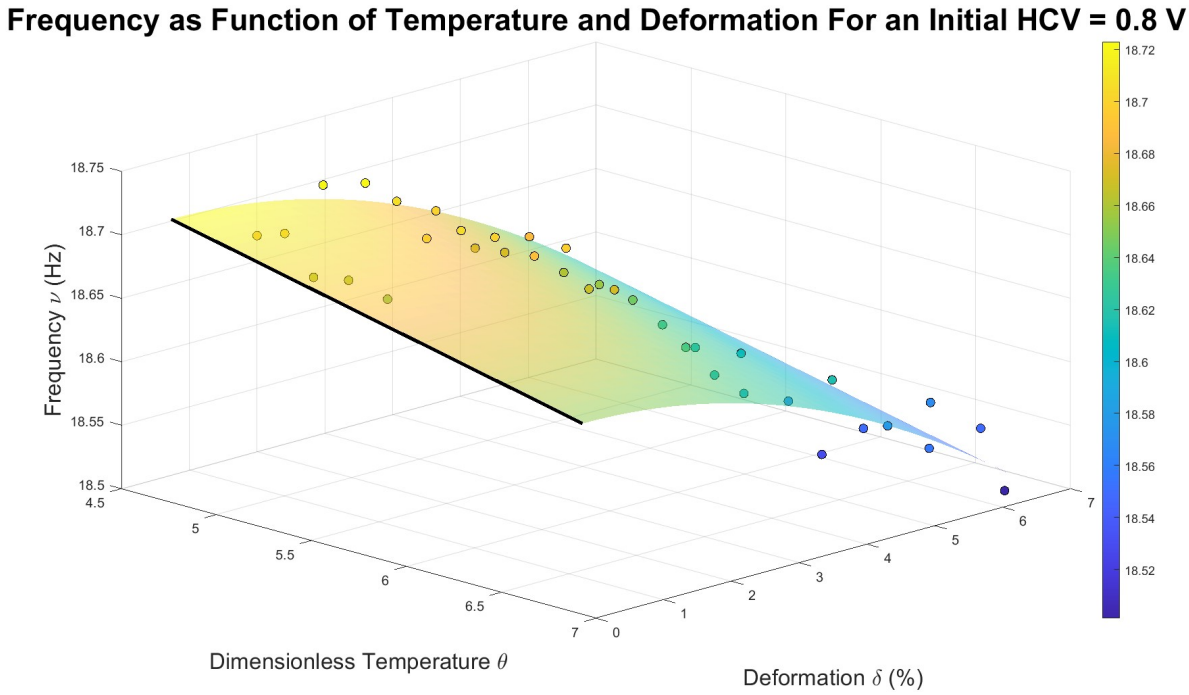

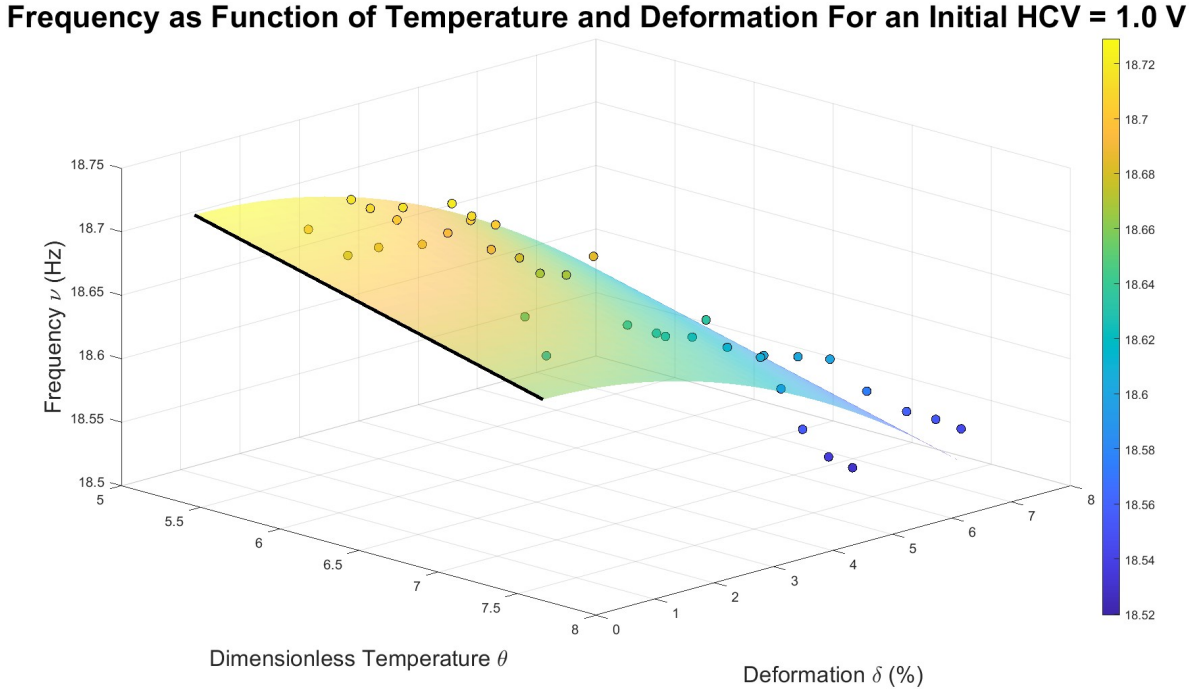

Figure E.1 : Plots of Corrected Frequency Formula ($\nu_c = \nu_{\theta=0}(1 + p_\theta\theta)(1 + p_1\delta + p_2\delta^2)$) for HCV Values of 0.3, 0.5, 0.6, 0.8 and 1.0 V Respectively

Corrected Surface Tension Profiles

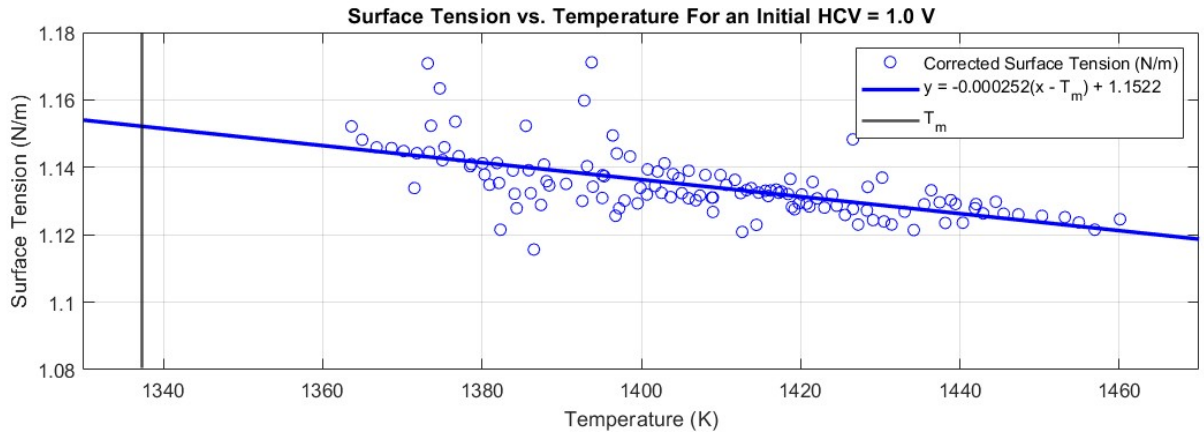

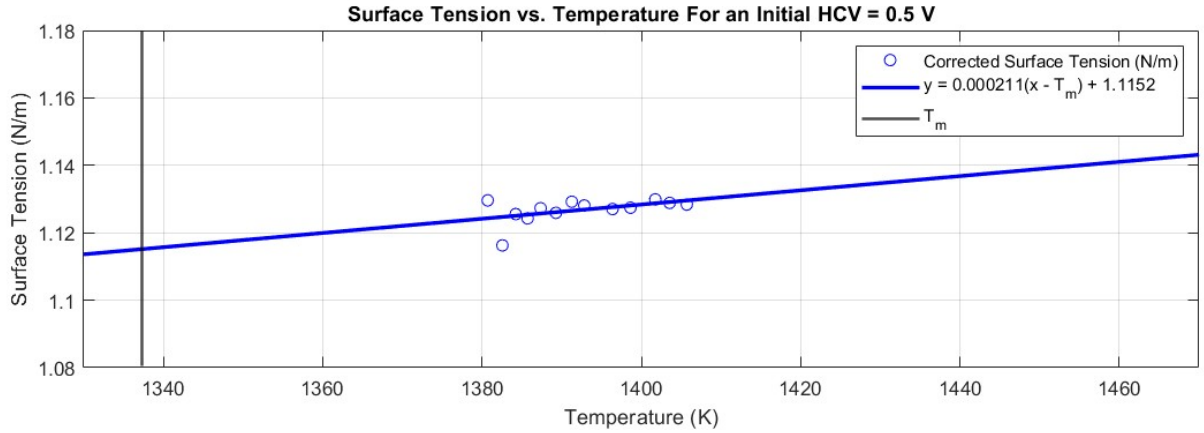

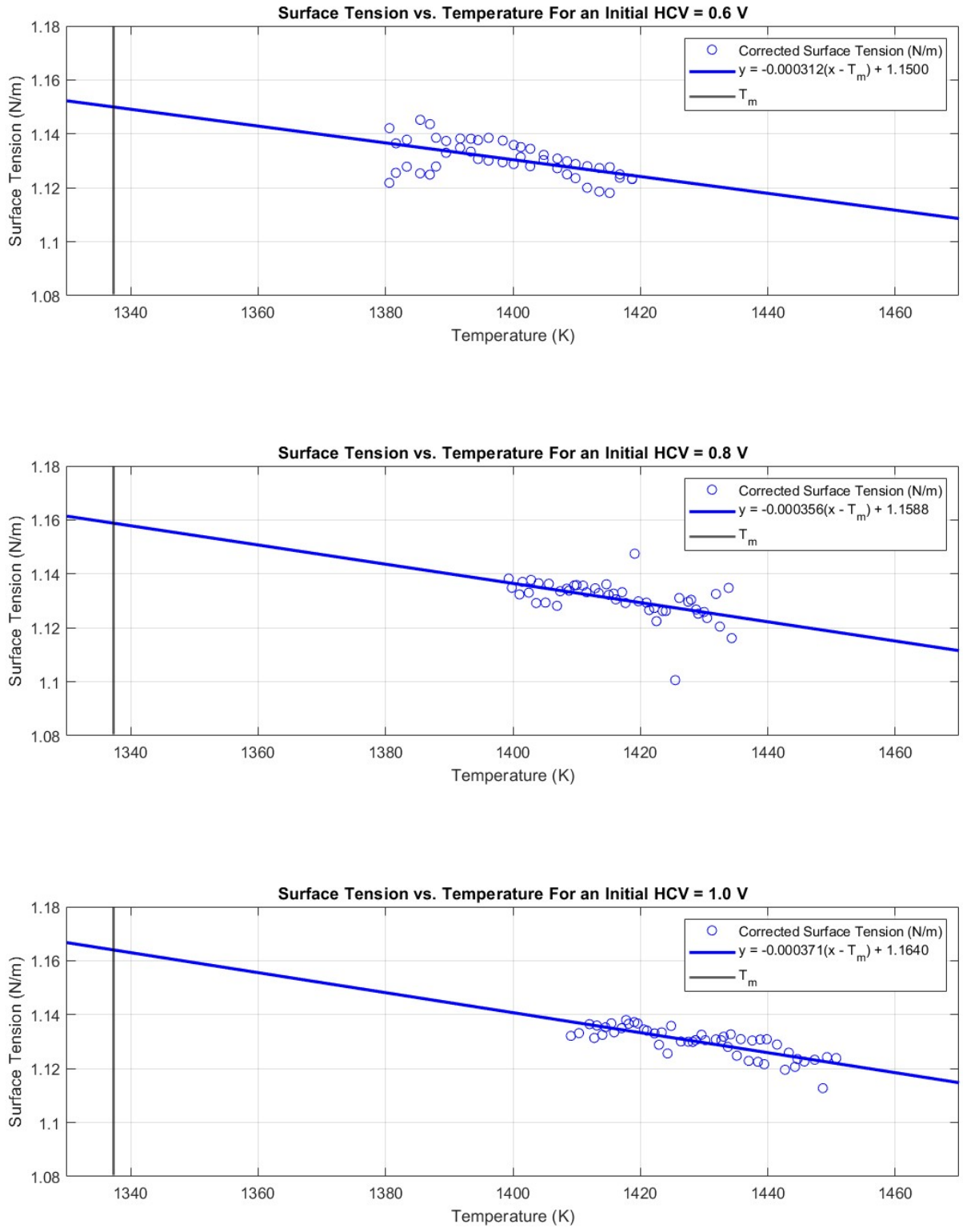

Figure F.1 : Individual Corrected Surface Tension vs. Temperature Profiles for HCV Values of 0.3, 0.5, 0.6, 0.8 and 1.0 V Respectively

Derivation of Gold and Electrical Conductivity

The electrical conductivity and density of the gold were measured using Science Coupling Electronics (SCE), a specific experimental module designed and implemented for measuring electrical conductivity [1]. Cycles 78 to 87 were specifically reserved for SCE testing. The following is a statement by Dr. Peace Muusha on the process of determining properties from SCE data:

The SCE system provides three key measured outputs: the voltage amplitude U_0, the current-to-voltage ratio $Y_0 = I_0/U_0$, and the phase shift between current and voltage. These are used to construct the complex total admittance of the heating circuit.

Using calibrated circuit parameters (capacitance, inductance, and resistance), the total admittance is then separated into real and imaginary components. From this, the sample contribution is isolated, giving the complex sample impedance Z_s, which depends on resistivity and sample radius.

Next, the real and imaginary parts of Z_s are used to solve for the electromagnetic parameter q, which relates the sample radius to the skin depth. Once q is known, resistivity is determined directly.

The sample radius is then obtained from the same impedance relationship, using the coil constant and frequency. Finally, density is calculated from the radius and the known sample mass using the spherical volume relation.

So in short, the chain is:

SCE signals $\rightarrow$ admittance $\rightarrow$ sample impedance $\rightarrow q \rightarrow$ resistivity and radius $\rightarrow$ density

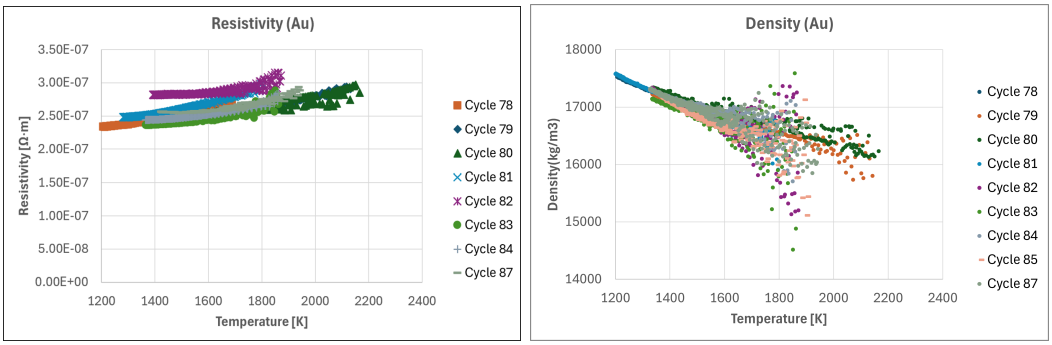

Figure G.1 : Raw Results of SCE Resistivity and Density

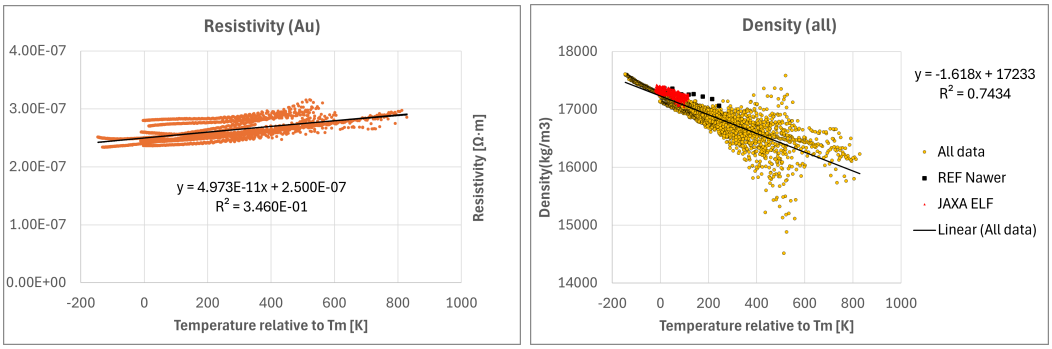

Figure G.2 : Raw Results of SCE Resistivity and Density with Linear Fit

Deposition Coil Mass Loss Table

Sample	Experiment	Cycle Number	Gas Type	Evaporated Mass / mg	Coating Layer Thickness / nm	Start	End
B4 Sample #11 Au ID122	Batch 4.1 Exp. 01	89	Argon	000.000E+00	000.000E+00	2025-09-02 00:07:06	2025-09-02 00:22:06
B4 Sample #11 Au ID122	Batch 4.1 Exp. 01	78	Argon	003.043E-03	407.222E-03	2025-09-02 00:30:00	2025-09-02 00:34:18
B4 Sample #11 Au ID122	Batch 4.1 Exp. 01	79	Argon	047.918E-03	006.411E+00	2025-09-02 00:45:02	2025-09-02 00:50:02
B4 Sample #11 Au ID122	Batch 4.1 Exp. 01	80	Argon	158.925E-03	021.264E+00	2025-09-02 00:54:54	2025-09-02 00:58:54
B4 Sample #11 Au ID122	Batch 4.1 Exp. 01	81	Argon	209.236E-03	027.995E+00	2025-09-02 01:05:10	2025-09-02 01:09:10
B4 Sample #11 Au ID122	Batch 4.1 Exp. 01	1	Argon	019.364E-03	002.590E+00	2025-09-02 22:05:00	2025-09-02 22:29:00
B4 Sample #11 Au ID122	Batch 4.1 Exp. 01	2	Argon	006.302E-03	843.267E-03	2025-09-02 22:36:00	2025-09-02 22:45:00
B4 Sample #11 Au ID122	Batch 4.1 Exp. 01	3	Argon	003.063E-03	409.923E-03	2025-09-02 23:15:00	2025-09-02 23:21:00
B4 Sample #11 Au ID122	Batch 4.1 Exp. 01	4	Argon	003.085E-03	412.812E-03	2025-09-02 23:31:00	2025-09-02 23:37:00
B4 Sample #11 Au ID122	Batch 4.1 Exp. 01	5	Argon	018.247E-03	002.441E+00	2025-09-02 23:50:00	2025-09-02 23:56:00
B4 Sample #11 Au ID122	Batch 4.1 Exp. 01	6	Argon	003.031E-03	405.545E-03	2025-09-03 00:04:00	2025-09-03 00:09:00
B4 Sample #11 Au ID122	Batch 4.1 Exp. 01	7	Argon	002.856E-03	382.145E-03	2025-09-03 00:16:00	2025-09-03 00:20:00
B4 Sample #11 Au ID122	Batch 4.1 Exp. 01	8	Argon	002.528E-03	338.250E-03	2025-09-03 01:05:00	2025-09-03 01:11:00
B4 Sample #11 Au ID122	Batch 4.1 Exp. 01	9	Argon	002.414E-03	323.038E-03	2025-09-03 01:33:00	2025-09-03 01:37:00
B4 Sample #11 Au ID122	Batch 4.1 Exp. 01	10	Argon	002.743E-03	367.079E-03	2025-09-03 01:43:00	2025-09-03 01:50:00
B4 Sample #11 Au ID122	Batch 4.1 Exp. 01	11	Argon	002.160E-03	289.008E-03	2025-09-03 02:21:00	2025-09-03 02:25:00
B4 Sample #11 Au ID122	Batch 4.1 Exp. 01	12	Argon	005.459E-03	730.506E-03	2025-09-03 02:34:00	2025-09-03 02:40:00
B4 Sample #11 Au ID122	Batch 4.1 Exp. 01	13	Argon	002.028E-03	271.385E-03	2025-09-03 03:10:00	2025-09-03 03:13:00
B4 Sample #11 Au ID122	Batch 4.1 Exp. 01	14	Argon	002.074E-03	277.563E-03	2025-09-03 03:26:00	2025-09-03 03:32:00
B4 Sample #11 Au ID122	Batch 4.1 Exp. 01	15	Argon	002.358E-03	315.599E-03	2025-09-03 04:18:00	2025-09-03 04:22:00
B4 Sample #11 Au ID122	Batch 4.1 Exp. 01	16	Argon	002.554E-03	341.798E-03	2025-09-03 04:30:00	2025-09-03 04:36:00
B4 Sample #11 Au ID122	Batch 4.1 Exp. 01	17	Argon	002.690E-03	359.951E-03	2025-09-04 02:25:00	2025-09-04 02:31:00
B4 Sample #11 Au ID122	Batch 4.1 Exp. 01	18	Argon	002.173E-03	290.879E-03	2025-09-04 02:42:00	2025-09-04 02:48:00
B4 Sample #11 Au ID122	Batch 4.1 Exp. 01	82	Argon	006.597E-03	882.741E-03	2025-09-04 03:25:00	2025-09-04 03:31:00
B4 Sample #11 Au ID122	Batch 4.1 Exp. 02	5	Argon	033.549E-03	004.488E+00	2025-09-04 04:08:00	2025-09-04 04:15:00

EML Toxicity Report: Analysis "All Cycles With One Sample": B4 Sample #11 Au ID122

Analysis "All Cycles With One Sample": B4 Sample #11 Au ID122

Used Formulas:

Formula Identifier	Formula
TEMPERATURE_RECALIBRATION	$T_i^{recalibrated} = L\left(L^{-1}(T_i) * \frac{\epsilon_{used}}{\epsilon_{true}}\right)$
HOLDER_ABSORPTION	H
EVAPORATIONS_PER_ELEMENT	$w_{Element} = distributionPercentage * w$
EPSILON_TRUE	$\epsilon_{true} = \epsilon_{used} * \frac{L^{-1}(ObserverdLiqTemp)}{L^{-1}(LiteratureLiqTemp)}$
COATING_LAYER_THICKNESS	$L_{Surface} = holderBlocking * \frac{m_{evap}}{Density} * \frac{1}{4\pi d_x^2} * 10^4$
GAS_SHIELDING	$S = \begin{cases} 1/(1+1.2*Pressure) & GasType = Argon \\ 1/((1+1.2*Pressure)*2.2) & GasType = Helium \\ 1 & otherwise \end{cases}$
EVAPORATIONS	$w = \sigma * S * H * \pi d^2 * A * \frac{e^{-B/T_i}}{\sqrt{T_i}} * \Delta t * 1000 \quad with \quad \sigma = \begin{cases} 0: & T_i \leq T_{Threshold} \\ 1: & otherwise \end{cases}$

Cycles included:

Deposition is calculated for a layer thickness onto the closest coil. This coil is located 10.35 mm from the sample center and thus total mass evaporated can be estimated as a spherical shell with known thickness at this radius.

Created at: 2026-03-26 15:10:14 by: Administrator

EML Toxicity Report: Analysis "All Cycles With One Sample": B4 Sample #11 Au ID122

Sample	Experiment	Cycle Number	Gas Type	Evaporated Mass / mg	Coating Layer Thickness / nm	Start	End
B4 Sample #11 Au ID122	Batch 4.1 Exp. 01	37	Argon	182.413E-06	024.406E-03	2025-09-23 22:40:00	2025-09-23 22:42:47
B4 Sample #11 Au ID122	Batch 4.1 Exp. 01	38	Argon	173.490E-06	023.212E-03	2025-09-23 22:53:00	2025-09-23 22:55:02
B4 Sample #11 Au ID122	Batch 4.1 Exp. 01	39	Argon	221.453E-06	029.630E-03	2025-09-23 23:05:00	2025-09-23 23:08:00
B4 Sample #11 Au ID122	Batch 4.1 Exp. 01	40	Argon	238.679E-06	031.935E-03	2025-09-23 23:25:00	2025-09-23 23:27:13
B4 Sample #11 Au ID122	Batch 4.1 Exp. 01	41	Argon	359.294E-06	048.073E-03	2025-09-23 23:39:00	2025-09-23 23:42:20
B4 Sample #11 Au ID122	Batch 4.1 Exp. 01	42	Argon	374.203E-06	050.068E-03	2025-09-24 00:11:00	2025-09-24 00:13:50
B4 Sample #11 Au ID122	Batch 4.1 Exp. 01	43	Argon	739.017E-06	098.879E-03	2025-09-24 00:24:00	2025-09-24 00:26:11
B4 Sample #11 Au ID122	Batch 4.1 Exp. 01	44	Argon	270.198E-06	036.152E-03	2025-09-24 00:38:00	2025-09-24 00:40:23
B4 Sample #11 Au ID122	Batch 4.1 Exp. 01	45	Argon	206.677E-06	027.653E-03	2025-09-24 00:57:00	2025-09-24 00:59:19
B4 Sample #11 Au ID122	Batch 4.1 Exp. 01	46	Argon	182.467E-06	024.413E-03	2025-09-24 01:14:00	2025-09-24 01:15:50
B4 Sample #11 Au ID122	Batch 4.1 Exp. 01	47	Argon	193.450E-06	025.883E-03	2025-09-24 01:25:44	2025-09-24 01:29:44
B4 Sample #11 Au ID122	Batch 4.1 Exp. 01	48	Argon	200.502E-06	026.827E-03	2025-09-24 01:48:00	2025-09-24 01:50:45
B4 Sample #11 Au ID122	Batch 4.1 Exp. 01	49	Argon	161.704E-06	021.635E-03	2025-09-24 02:03:00	2025-09-24 02:05:00
B4 Sample #11 Au ID122	Batch 4.1 Exp. 01	50	Argon	539.864E-06	072.233E-03	2025-09-24 02:23:00	2025-09-24 02:25:28
B4 Sample #11 Au ID122	Batch 4.1 Exp. 01	83	Argon	006.269E-03	838.865E-03	2025-09-24 03:01:00	2025-09-24 03:12:13
B4 Sample #11 Au ID122	Batch 4.1 Exp. 01	84	Argon	005.787E-03	774.377E-03	2025-09-24 03:18:00	2025-09-24 03:24:53
B4 Sample #11 Au ID122	Batch 4.1 Exp. 02	7	Argon	002.791E-03	373.466E-03	2025-09-24 04:12:00	2025-09-24 04:22:00
B4 Sample #11 Au ID122	Batch 4.1 Exp. 02	8	Argon	003.502E-03	468.634E-03	2025-09-24 22:31:00	2025-09-24 22:42:00
B4 Sample #11 Au ID122	Batch 4.1 Exp. 02	1	Argon	004.440E-03	594.184E-03	2025-09-24 23:29:04	2025-09-24 23:39:00
B4 Sample #11 Au ID122	Batch 4.1 Exp. 02	2	Argon	006.867E-03	918.898E-03	2025-09-25 00:02:00	2025-09-25 00:13:00
B4 Sample #11 Au ID122	Batch 4.1 Exp. 02	9	Argon	004.959E-06	663.519E-06	2025-09-25 00:44:00	2025-09-25 00:53:00
B4 Sample #11 Au ID122	Batch 4.1 Exp. 02	10	Argon	002.920E-06	390.821E-06	2025-09-25 03:23:00	2025-09-25 03:37:00
B4 Sample #11 Au ID122	Batch 4.1 Exp. 01	56	Argon	615.351E-06	082.333E-03	2025-09-25 04:05:00	2025-09-25 04:09:00
B4 Sample #11 Au ID122	Batch 4.1 Exp. 01	57	Argon	575.085E-06	076.945E-03	2025-09-25 04:23:00	2025-09-25 04:27:00
B4 Sample #11 Au ID122	Batch 4.1 Exp. 01	60	Argon	001.319E-03	176.484E-03	2025-09-25 21:46:00	2025-09-25 21:50:00

Created at: 2026-03-26 15:10:14 by: Administrator

EML Toxicity Report: Analysis "All Cycles With One Sample": B4 Sample #11 Au ID122

Sample	Experiment	Cycle Number	Gas Type	Evaporated Mass / mg	Coating Layer Thickness / nm	Start	End
B4 Sample #11 Au ID122	Batch 4.1 Exp. 02	11	Argon	003.263E-03	436.634E-03	2025-09-04 21:52:32	2025-09-04 22:08:32
B4 Sample #11 Au ID122	Batch 4.1 Exp. 01	58	Argon	926.308E-06	123.939E-03	2025-09-04 22:37:05	2025-09-04 22:42:05
B4 Sample #11 Au ID122	Batch 4.1 Exp. 01	19	Argon	002.399E-03	321.114E-03	2025-09-04 23:11:23	2025-09-04 23:15:23
B4 Sample #11 Au ID122	Batch 4.1 Exp. 02	6	Argon	006.081E-03	813.716E-03	2025-09-05 00:15:56	2025-09-05 00:27:56
B4 Sample #11 Au ID122	Batch 4.1 Exp. 02	12	Argon	023.193E-06	003.103E-03	2025-09-05 00:37:53	2025-09-05 00:55:53
B4 Sample #11 Au ID122	Batch 4.1 Exp. 01	59	Argon	801.975E-06	107.304E-03	2025-09-05 01:43:00	2025-09-05 01:47:00
B4 Sample #11 Au ID122	Batch 4.1 Exp. 01	54	Argon	930.607E-06	124.514E-03	2025-09-05 02:12:58	2025-09-05 02:16:58
B4 Sample #11 Au ID122	Batch 4.1 Exp. 01	55	Argon	740.444E-06	099.070E-03	2025-09-05 02:45:18	2025-09-05 02:49:18
B4 Sample #11 Au ID122	Batch 4.1 Exp. 01	20	Argon	002.506E-03	335.417E-03	2025-09-05 03:25:00	2025-09-05 03:28:20
B4 Sample #11 Au ID122	Batch 4.1 Exp. 01	21	Argon	002.530E-03	338.521E-03	2025-09-05 03:50:56	2025-09-05 03:53:56
B4 Sample #11 Au ID122	Batch 4.1 Exp. 01	22	Argon	002.378E-03	318.285E-03	2025-09-05 04:04:51	2025-09-05 04:08:51
B4 Sample #11 Au ID122	Batch 4.1 Exp. 01	23	Argon	002.542E-03	340.120E-03	2025-09-05 04:23:00	2025-09-05 04:25:23
B4 Sample #11 Au ID122	Batch 4.1 Exp. 01	24	Argon	002.591E-03	346.794E-03	2025-09-22 22:01:00	2025-09-22 22:04:00
B4 Sample #11 Au ID122	Batch 4.1 Exp. 01	25	Argon	002.649E-03	354.459E-03	2025-09-22 22:40:00	2025-09-22 22:42:00
B4 Sample #11 Au ID122	Batch 4.1 Exp. 01	26	Argon	003.870E-06	517.856E-06	2025-09-22 23:33:00	2025-09-22 23:35:00
B4 Sample #11 Au ID122	Batch 4.1 Exp. 01	27	Argon	002.495E-03	333.868E-03	2025-09-22 23:52:00	2025-09-22 23:55:00
B4 Sample #11 Au ID122	Batch 4.1 Exp. 01	28	Argon	003.029E-03	405.355E-03	2025-09-23 00:58:00	2025-09-23 01:00:00
B4 Sample #11 Au ID122	Batch 4.1 Exp. 01	29	Argon	002.659E-03	355.880E-03	2025-09-23 01:14:00	2025-09-23 01:17:00
B4 Sample #11 Au ID122	Batch 4.1 Exp. 01	30	Argon	005.174E-03	692.403E-03	2025-09-23 01:29:00	2025-09-23 01:33:00
B4 Sample #11 Au ID122	Batch 4.1 Exp. 01	31	Argon	897.165E-06	120.040E-03	2025-09-23 02:10:00	2025-09-23 02:13:00
B4 Sample #11 Au ID122	Batch 4.1 Exp. 01	32	Argon	835.387E-06	111.774E-03	2025-09-23 02:42:00	2025-09-23 02:44:00
B4 Sample #11 Au ID122	Batch 4.1 Exp. 01	33	Argon	884.550E-06	118.352E-03	2025-09-23 03:35:00	2025-09-23 03:38:10
B4 Sample #11 Au ID122	Batch 4.1 Exp. 01	34	Argon	180.770E-06	024.186E-03	2025-09-23 03:50:00	2025-09-23 03:51:57
B4 Sample #11 Au ID122	Batch 4.1 Exp. 01	35	Argon	082.336E-06	011.016E-03	2025-09-23 04:18:00	2025-09-23 04:21:00
B4 Sample #11 Au ID122	Batch 4.1 Exp. 01	36	Argon	207.425E-06	027.753E-03	2025-09-23 21:50:00	2025-09-23 21:53:14

Created at: 2026-03-26 15:10:14 by: Administrator

Evaporated Mass Chart:

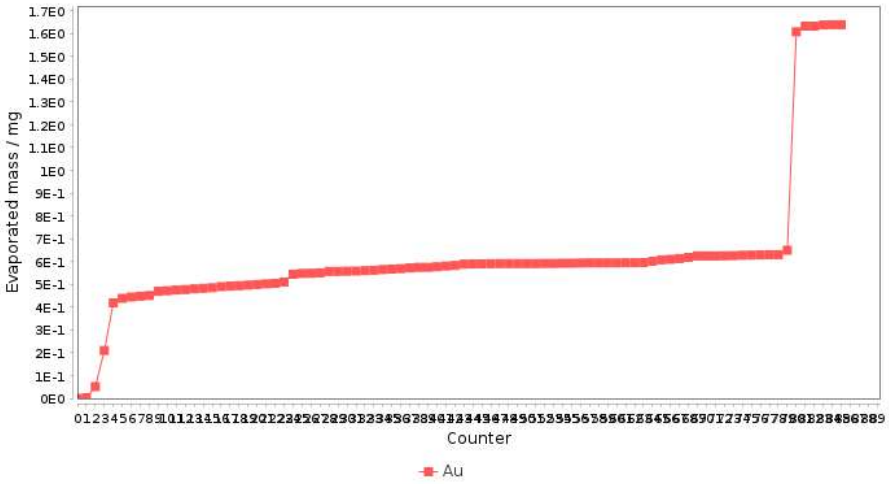

Coating Layer Thickness Chart:

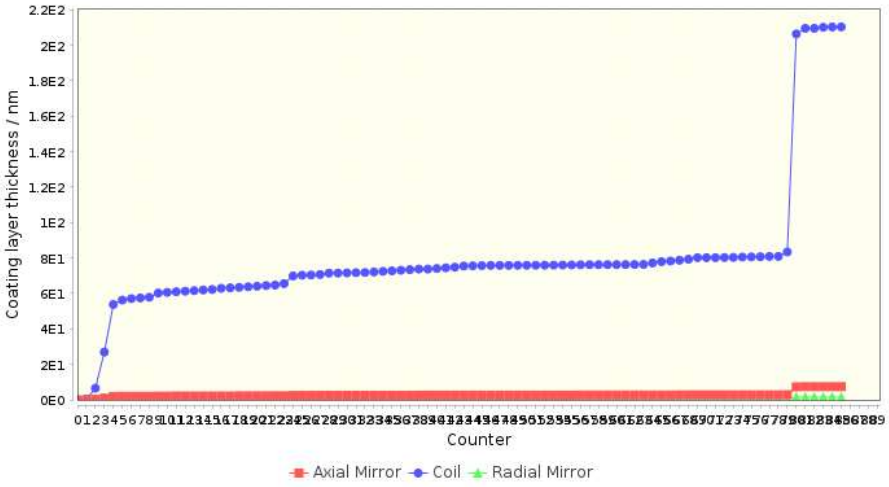

EML Toxicity Report: Analysis "All Cycles With One Sample": B4 Sample #11 Au ID122

Sample	Experiment	Cycle Number	Gas Type	Evaporated Mass / mg	Coating Layer Thickness / nm	Start	End
B4 Sample #11 Au ID122	Batch 4.1 Exp. 01	61	Argon	752.002E-06	100.617E-03	2025-09-25 22:01:00	2025-09-25 22:05:22
B4 Sample #11 Au ID122	Batch 4.1 Exp. 01	51	Argon	663.653E-06	088.796E-03	2025-09-25 22:41:00	2025-09-25 22:45:00
B4 Sample #11 Au ID122	Batch 4.1 Exp. 01	52	Argon	001.443E-03	193.102E-03	2025-09-25 22:58:00	2025-09-25 23:03:00
B4 Sample #11 Au ID122	Batch 4.1 Exp. 01	53	Argon	126.035E-06	016.863E-03	2025-09-25 23:28:00	2025-09-25 23:31:56
B4 Sample #11 Au ID122	Batch 4.1 Exp. 01	85	Argon	019.409E-03	002.596E+00	2025-09-26 00:45:00	2025-09-26 00:50:00
B4 Sample #11 Au ID122	Batch 4.1 Exp. 01	86	Argon	958.253E-03	128.213E+00	2025-09-26 01:34:00	2025-09-26 01:39:00
B4 Sample #11 Au ID122	Batch 4.1 Exp. 01	87	Argon	024.566E-03	003.287E+00	2025-09-26 02:07:00	2025-09-26 02:18:00
B4 Sample #11 Au ID122	Batch 4.1 Exp. 01	62	Argon	183.556E-06	024.559E-03	2025-09-26 02:39:00	2025-09-26 02:43:00
B4 Sample #11 Au ID122	Batch 4.1 Exp. 01	67	Argon	004.747E-03	635.168E-03	2025-09-26 03:03:00	2025-09-26 03:05:00
B4 Sample #11 Au ID122	Batch 4.1 Exp. 01	65	Argon	001.281E-03	171.486E-03	2025-09-26 03:51:00	2025-09-26 03:55:00
B4 Sample #11 Au ID122	Batch 4.1 Exp. 01	63	Argon	236.082E-06	031.587E-03	2025-09-26 04:16:00	2025-09-26 04:20:00

Evaporated Mass in Chamber Atmosphere:

Element	Evaporated Mass / mg	Sample tox limit / mg	Status
Au	001.639E+00	960.000E+00	✓
Sum	001.639E+00		Σ

Coating Layer Thickness:

Surface	Coating Layer Thickness / nm	Sample coating layer limit / nm	Status
Axial Mirror	007.447E+00	201.000E+03	✓
Coil	210.299E+00	201.000E+03	✓
Radial Mirror	001.564E+00	201.000E+03	✓

Created at: 2026-03-26 15:10:14 by: Administrator

Code

Below are pseduocode representations of the code written for this thesis. Full scripts can be found in the following GitHub repository: https://github.com/wcusato/Thesis.git

I.1 Sectioned Analysis

Algorithm 1 Oscillation Extraction and Temperature-Resolved Fitting

Input: Deformation data, temperature data, sampling frequency F_s
Select time window $[n_1, n_2]$ and construct time vector t
Align and interpolate temperature onto t
Select deformation metric (area, radius, etc.)
Global Fit:
Fit $Ae^{-t/\tau}\cos(2\pi\nu t + \phi) + D$
Extract parameters (A, τ, ν, ϕ, D) and covariance
Sliding-Window Analysis:
for each time segment **do**
    Extract $(t_{\text{seg}}, \text{area}_{\text{seg}}, T_{\text{seg}})$
    Fit damped oscillation model
    if fit converged **and** R^2 high **and** no temperature spike **then**
        Compute parameter uncertainties
        Compute deformation δ
        Propagate error from covariance
        Store (T, ν, τ, δ) and uncertainties
    end if
end for
Bin results by temperature and remove duplicates
Output: $\nu(T)$, $\tau(T)$, $\delta(T)$

I.2 Surface Tension Correction

Algorithm 2 Frequency Modeling and Surface Tension Extraction

Input: Temperature-binned dataset (δ, ν, T) and mass m
Select most populated temperature bins
Combine into unified dataset
Compute reduced temperature:

$$h = \frac{T - T_{\text{liq}}}{T_{\text{liq}}}$$

Model:

$$\nu(h, \delta) = f_0(1 + p_h h)(1 + p_1\delta + p_2\delta^2)$$

Fit model using nonlinear least squares
Extract parameters and covariance
Compute goodness-of-fit (R^2)
Surface Tension:

$$\gamma = \frac{3\pi}{8}\, m\, \nu^2$$

$$\gamma_c = \frac{3\pi}{8}\, m\, \nu^2 \left(1 + p_1\delta + p_2\delta^2\right)^{-2}$$

Fit linear models of γ and γ_c vs. T
Error Propagation:
Compute partial derivatives of γ_c with respect to ν, δ, p_1, and p_2
Include parameter covariance terms
Compute uncertainty in γ_c
Output: Surface tension vs. temperature and fitted model

I.3 Velocity and Reynolds Number

Algorithm 3 Convective Velocity and Reynolds Number Prediction

Input: Temperature T, heater voltages U_H, positioner voltages U_P, mass m
Constants: Gas constant R, melting temperature T_m
for each temperature T **do**
    for each heater setting (U_H, U_P) **do**
        Compute material properties:
        $\rho \leftarrow \rho(T)$
        $\mu \leftarrow \mu(T)$
        $\gamma \leftarrow \gamma(T)$
        Compute transformed variables:
        $\ln \gamma$, $\ln \mu$, $\gamma^{-1/2}$, $(\ln \mu)^{-1}$
        Evaluate velocity model:
        $u_{\max} \leftarrow$ polynomial in $(\ln \gamma, \ln \mu, \rho, U_H)$
                    $-$ exponential correction term in (γ, μ, ρ, U_P)
        Compute droplet size:
        $V \leftarrow m/\rho$
        $d \leftarrow (6V/\pi)^{1/3}$
        Compute Reynolds number:

$$\mathrm{Re} = \frac{\rho \, u_{\max} \, d}{\mu}$$

        Store $u_{\max}$ and Re
    end for
end for
Output:
Velocity $u_{\max}(T, U_H)$
Reynolds number $\mathrm{Re}(T, U_H)$
Plot results vs. temperature for each heater setting